Carnegie Mellon University

CARNEGIE INSTITUTE OF TECHNOLOGY

THESIS

SUBMITTED IN PARTIAL FULFILLMENT OF THE REQUIREMENTS

FOR THE DEGREE OF Doctor of Philosophy

TITLE Ultrasonic Signal Processing for Structural Damage Detection and Quantification

PRESENTED BY Peng Gong

ACCEPTED BY THE DEPARTMENTS OF

Civil and Environmental Engineering

Irving J. Oppenheim — ADVISOR, MAJOR PROFESSOR — December 28, 2015 — DATE

David A. Dzombak — DEPARTMENT HEAD — December 28, 2015 — DATE

APPROVED BY THE COLLEGE COUNCIL

Vijayakumar Bhagavatula — DEAN — January 4, 2016 — DATE

Ultrasonic Signal Processing for Structural Damage Detection and Quantification

Submitted in partial fulfillment of the requirements for

the degree of

Doctor of Philosophy

in

Civil and Environmental Engineering

Peng Gong

B.S., Civil and Environmental Engineering, Dalian University of Technology
M.S., Civil and Environmental Engineering, Dalian University of Technology

Carnegie Mellon University
Pittsburgh, PA

December, 2015

Copyright Notice

To my parents
and to my wife Yang and my daughter Grace
for their love, support, encouragement, and inspiration

Acknowledgements

I would never have been able to finish my dissertation, reach the heights or explore the breadths of knowledge without the guidance of my committee members, the discussions with my collaborators and colleagues, the support from my family and my wife, and the help from many other people.

I would like to thank each member of my committee, Dr. Irving Oppenheim, David Greve, Warren Junker, Mario Berges, and Joel Harley, for their guidance. I would like to express my deepest gratitude to my advisor Dr. Oppenheim. Thank you for your excellent guidance, encouragement, patience, and providing me with an excellent atmosphere for doing research. Thank you for teaching me how to write an academic paper, how to present my research work, and how to be excellent on many other things. I would like to thank Dr. Greve who has been providing me the greatest insights into my research questions and giving me direct advice on software and hardware issues related to ultrasonic devices. I would like to thank Dr. Junker for guiding me through many difficult problems in my research work using his expertise in the field of ultrasound and his rich working experience in the field of ultrasonic nondestructive evaluation. I would like to thank Dr. Berges and Dr. Harley for providing me great research ideas, teaching me signal processing and machine learning, and giving me advice on many other problems.

I would like to thank Dr. James Garrett for giving me career guidance, thank Dr. Craig Maloney for guiding me through ultrasound, thank Dr. Hae Young Noh for teaching me structural health monitoring and machine learning, and thank Dr. Lawrence Cartwright for the help on my experimental work. I would also like to thank our CEE staff members, Ron Ripper, Maxine Leffard, Julian Krishnamurti, Mireille Mobley, Cornelia Moore and many others for the great support and numerous help in the past years.

I would like to thank Dr. Mark Patton at MEP Ltd who had directed me through the experimental work on concrete. His strong expertise on concrete problems had helped me a lot. I would like to thank ç and my collaborators there including Jack Lareau, Mike Burke, and Tom Nenno for their testing devices, advice, and practical knowledge. I would like to thank Dr. Thomas Hay at TechKnowServ Corp for providing me with the frac iron specimens and his great insights and help on my research work. I would also like to thank Dr. Christoph Hurley at NobelClad for his great insights on my research studies on clad steel although this topic is outside the scope of this dissertation.

I would also like to thank my fellow graduate student collaborators, Chang Liu, Matineh Eybpoosh, Erin Dauson, Jingkun Gao, and George Lederman. It has been an honor for me to work with such smart and motivated graduate students. I would also like to thank my officemates and colleagues, Hui Wang, Xiaohan Zhang, Seung Kun Park, Mostafa Mirshekari, Irem Velibeyoglu, Susu Xu, Chiqun Zhang, Yiming Gu, Hanqi Cheng, Pengyun Wang, Fiona Zhang, Lauren Cook, Suman Giri and many others. It has been a pleasure for me to work together with them and learn from each other for the past few years.

The research work in this dissertation was supported by Westinghouse Electric Company, the Pennsylvania Infrastructure Technology Alliance (PITA), and the National Energy Technology Laboratory.

Abstract

The operation of our society depends heavily on infrastructure systems. To prevent failures and to reduce costs of maintenance, structural health monitoring (SHM) systems have been implemented on an increasing number of infrastructure systems. SHM systems have the potential to give reliable prediction of structural deterioration with less human safety risk and labor costs, and without interruption of normal operations.

In the field of SHM, many techniques have been proposed in recent decades. Among these techniques, ultrasonic testing has been widely used for damage characterization in structures and materials. However, there remain many challenges in real-world SHM applications. For example, temperature variations can cause a significant decrease in performance of ultrasonic testing. Although there exist some temperature compensation techniques to improve the performance of ultrasonic testing under temperature variations, these techniques have their own limitations.

This dissertation will focus on novel ultrasonic signal processing techniques for damage detection, quantification and temperature compensation. In Chapter 2, I will propose a modified optimal signal stretching (OSS) method and an singular value decomposition (SVD) method to solve the temperature compensation problem, where the OSS method (in its original form) failed to perform well for damage detection. In Chapter 3, I will study the statistical orthogonal relationship between temperature-induced and damage-induced ultrasonic change signals. The orthogonal relationship can be used to explain why SVD performs well under varying temperature conditions and why it also has the potential (under some conditions) to be directly used for damage detection and quantification. In Chapter 4, I

will study the ultrasonic time-of-flight diffraction technique, which is used to quantify wall thickness loss of thick-walled aluminum tubes, because the conventional pulse-echo method did not perform well in my target application. In Chapter 5, I will propose a novel ultrasonic passband technique to quantify the alkali-silica reaction (ASR) caused cracking damage in concrete structures. This technique is based on the ultrasonic wave filtering effects of cracks in concrete. With the progress of ASR caused cracking damage in concrete, more high frequency components of ultrasonic waves are filtered out than low frequency components.

The research work in this dissertation has the potential to help advance ultrasonic SHM techniques, to improve the real-world performance of ultrasonic SHM, to prevent failures of infrastructure systems, and to reduce the costs of maintenance if the proposed ultrasonic techniques can be implemented in real infrastructure systems in the future. However, some future work still needs to be done in order to implement the techniques studied in this dissertation in real-world applications.

Contents

List of Tables

List of Figures

Chapter 1 Introduction

1.1 Motivation

Our society depends heavily on civil infrastructure systems including, for example, oil and gas pipelines, water pipelines, roads, railways, bridges, dams, buildings, etc. Failures of infrastructure systems can cause fatalities, injuries, economic loss, and environmental disasters. For example, the Pipeline and Hazardous Materials Safety Administration (PHMSA), an agency within the United States Department of Transportation (DOT), lists the oil and gas pipeline incidents occurred in the United States between 1995 and 2014 as shown in Table 1-1 (PHMSA 2015). In those twenty years, the total number of oil and gas pipeline incidents is 10,848. These incidents caused 371 fatalities, 1,398 injuries and $6.3 billion economic loss. Here a pipeline incident is reported if any of the following occur: (1) explosion or fire not intentionally set by the operator; (2) release of five gallons or more of a hazardous liquid (any petroleum or petroleum product) or carbon dioxide; (3) fatality; (4) personal injury necessitating hospitalization; and (5) property damage, including cleanup costs, and the value of lost product, and the damage to the property of the operator or others, or both, estimated to exceed $50,000 (PHMSA 2011).

Table 1-1 The pipeline incidents listed by PHMSA (1995-2014)

Calendar Year	Number	Fatalities	Injuries	Property Damage As Reported
1995	349	21	64	$53,427,112
1996	381	53	127	$114,467,631
1997	346	10	77	$79,757,922
1998	389	21	81	$126,851,351
1999	339	22	108	$130,110,339
2000	380	38	81	$191,822,840
2001	341	7	61	$63,092,462
2002	642	12	49	$102,167,588
2003	672	12	71	$139,057,814
2004	672	23	60	$271,836,502
2005	720	17	48	$1,245,463,189
2006	639	21	36	$151,855,467
2007	615	16	49	$154,937,018
2008	660	8	57	$565,819,340
2009	628	13	64	$179,070,183
2010	588	22	109	$1,504,215,990
2011	595	14	56	$404,516,407
2012	570	12	57	$228,107,540
2013	618	10	46	$336,332,898
2014	704	19	97	$302,334,081
Grand Total	**10,848**	**371**	**1,398**	**$6,345,243,674**

Regular inspection and maintenance is important for keeping infrastructure systems functioning properly and avoiding failures. More than $200 billion is spent on the maintenance of plant, equipment, and facilities each year in the United States (Giurgiutiu 2007). These huge costs have become an increasing concern in structure inspection and maintenance.

To prevent failures of infrastructure systems and to reduce the costs of maintenance, structural health monitoring (SHM) systems have been implemented on an increasing number of infrastructure systems. SHM systems are slowly growing to be standard requirements for modern high-cost infrastructure systems (Kołakowski 2007). In SHM systems, sensors are used to record signals, damage-sensitive features are extracted from the recorded signals, and a specific criterion from statistical analysis is then used to determine the current state of system (Farrar and Worden 2007). SHM systems have the potential to give reliable prediction of structural deterioration with less human safety risk and lower labor costs, and without interruption of normal operation.

1.2 Introduction to Ultrasonic Structural Health Monitoring

In the field of SHM, many techniques have been proposed in recent decades for damage characterization in a variety of engineering structures and materials. According to the types of models used, SHM methods can be classified into two categories: model-based methods and data-driven methods.

For model-based methods, physical models must be selected to model the structure, and the structural geometry and material properties must be known before the use of this method (Laory et al. 2011). In the calibration stage, model parameters are calculated using the data recorded before the structure is damaged. In the monitoring stage, new model parameters are recalculated using the new-coming data and then compared with those before damage to see if the new model parameters pass the predefined threshold or not. These methods are straightforward and easy to interpret, but sometimes it is expensive and difficult to build such physical models.

For data-driven methods, statistical models are used to process the data collected from the structure so that the structural geometry and material properties are usually unimportant for these methods (Laory et al. 2011). Generally speaking, data-driven methods are not structure-selective and therefore a method can be used on different types of structures. However, it is sometimes difficult to interpret the results from data-driven methods, especially for damage quantification. Because of the absence of physical models, calibration is necessary to interpret the output from data-driven methods.

In this dissertation, I will investigate both model-based methods, such as the ultrasonic time-of-flight diffraction method and the ultrasonic passband method, and data-driven methods, such as the modified optimal signal stretching (OSS) method and the singular value decomposition (SVD) method.

According to (Kołakowski 2007), ultrasonic testing is defined as *"the interrogation of materials using stress waves of the frequency higher than 20 kHz. "* In ultrasonic testing, piezoelectric transducers are the most widely used transducers although other types of transducers are also available such as electromagnetic acoustic transducers (EMAT). Piezoelectric transducers are popular in SHM because they have good electromechanical properties, relatively low price, both actuating and sensing capabilities, wide measuring range, wide operating temperature, and so on (Kołakowski 2007). Details of piezoelectric materials and their actuating and sensing capabilities can be found in (Gautschi 2002).

In ultrasonic SHM, the operating frequencies depend on the types of defects. Theoretically, the smallest defect size detectable is on the order of the wavelength. The high-frequency ultrasonic waves are more sensitive to defects. However, the low-frequency ultrasonic waves can propagate deeper into the structure. Therefore, a compromise between sensitivity and monitoring range always exists in practice (Kołakowski 2007) and the operating frequency range should be selected based on specific applications.

Ultrasonic waves include ultrasonic bulk waves and ultrasonic guided waves. Bulk waves propagate in the bulk of the testing material away from the boundaries, although some boundary interactions such as reflection, refraction, and diffraction, might be involved. On the other hand, guided waves propagate in the testing material while guided by its boundaries. Bulk waves in isotropic materials are the longitudinal mode and the shear mode (the shear mode can be polarized horizontally or vertically). However, there are generally an infinite number of modes for guided waves due to the introduction of boundary conditions (Rose 2004). Some guided wave problems are already solved such as Rayleigh, Lamb and Stonely waves (Rose 2004). The many guided wave modes typically cause complexity and limit the use of such waves for SHM. However, the diversity of ultrasonic wave types and modes also provides options for SHM because different types and modes of ultrasonic waves can have different sensitivities and other properties in different applications.

Ultrasonic testing can be operated in three major scanning techniques – pulse echo technique, pitch-catch technique, and phased array technique. The pulse-echo technique utilizes the ultrasonic wave reflection phenomenon at the boundary of two different materials. At the boundary, only a portion of ultrasonic waves will be transmitted (refracted) into the other material, and the other portion of ultrasonic waves will be reflected back. The proportion of refraction and reflection depends on the acoustic impedance of the two materials and the angle of incidence (Kołakowski 2007). The pulse-echo technique receives the echoes reflected from material boundaries and determines the current structural state based on the time of arrival, amplitude, and shape of echoes. The pulse-echo technique requires only one transducer and requires access only to one surface of the testing structure. The pitch-catch technique utilizes one transducer as an emitter and another transducer as a receiver. The pitch-catch technique is very flexible because the emitter and receiver can be placed anywhere on the same surface or on different surfaces, provided that the ultrasonic waves can be transmitted to the receiver from the emitter. The pitch-catch technique is especially useful for high-damping materials or materials with strong scattering effects, such as concrete, because echoes from an opposite surface may not always be obtainable. The pitch-catch technique is also widely used when a large monitoring area is required; an example would be damage detection on a pipe structure when the damage location is not known before the monitoring plan is implemented. The phased array technique is an advanced technique of ultrasonic testing that has wide applications. The phased array is an array of transducers placed at locations with certain patterns, and the capability of closely controlling the relative phases of the transducers. The controllable relative phases can produce a steerable, tightly focused, high-resolution ultrasonic beam. The phased array technique has advantages over conventional ultrasonic techniques including high inspection speed, flexible data processing capability, improved resolution, and electronic steering, but it has very demanding requirements regarding the electronic devices when compared with conventional ultrasonic techniques (Giurgiutiu 2007).

Overall, ultrasonic testing has good sensitivity to a variety of defect types because of its wide operating frequency range, different types and modes, and can have large monitoring range due to the long propagating distance of ultrasonic waves. Other advantages of ultrasonic testing include safe operation conditions for the staff, relatively low cost of testing, and so forth (Kołakowski 2007). These advantages of ultrasonic testing make it attractive for SHM applications.

1.3 Challenges

1.3.1 Environmental and Operational Conditions

In current SHM techniques, most methods are sensitive to environmental and operational conditions (EOCs) such as temperature, pressure, and environmental noises. Sometimes, changes caused by temperature can be significantly larger than those caused by structural damage. For example, Koo et al. (Koo et al. 2013) studied the monitoring data over a period of three years from the Tamar suspension bridge and they concluded that the bridge global deformation was mainly caused by the thermal expansion of the deck, main cables and additional stays, but not by the vehicle loading or wind. Catbas et al. (Catbas et al. 2008) studied the longest cantilever truss bridge in the United States. They found the temperature could change between 15 F and 90 F during a one-year monitoring duration, and that this temperature variation caused a peak-peak strain differential that was ten times larger than that induced by the vehicle loading. The temperature has so significant an influence on structures that monitoring data collected with temperature variations must be processed carefully in order to have reliable monitoring results.

For ultrasonic SHM, it is also well known that EOCs, e.g. temperature variations (Weaver and Lobkis 2000) and stress (Michaels et al. 2009), can change the propagating velocity of ultrasonic waves and thus alter the monitoring results if EOCs are not compensated properly. Among all factors, the temperature variations are most common in practical applications of SHM techniques based on ultrasonic waves. To eliminate or reduce the temperature effects, optimal baseline subtraction (OBS) and optimal signal stretch (OSS) (Croxford et al. 2010; Lu and Michaels 2005) methods are widely used in ultrasonic methods.

Singular value decomposition (Liu et al. 2015; Liu et al. 2012) and sparse representation of ultrasonic guided waves (Eybpoosh et al. 2015; Eybpoosh et al. 2015) can also perform well for damage detection or localization under temperature variations.

In the OBS method, large sets of ultrasonic signals are recorded under different temperatures before structural damage, and these ultrasonic measurements are used to establish the baseline database. In order to compensate the temperature variations accurately, the database should be established with the temperature range sufficiently large to contain all possible temperature values to be encountered during monitoring. In the monitoring stage, the new measurement is compared to all the existing measurements in the database and the closest measurement in the database is selected for temperature compensation (Croxford et al. 2007; Lu and Michaels 2005). However, temperature is a continuous variable, so it is impossible to include all the possible temperatures in the database, let alone other EOCs. In practice, the temperature interval in the database should be as small as possible when time, storage, computation and other costs are acceptable.

The OSS method is another commonly used method for temperature compensation in ultrasonic SHM. In the OSS method, temperature changes are assumed to have (approximately) stretching or compressing effects on diffuse ultrasonic waves (Lu and Michaels 2005; Weaver and Lobkis 2000). Therefore, this method estimates an optimal stretching factor and then stretches the new-coming signal to match the baseline signal for temperature compensation. However, the stretching model can be applied only when the temperature variation is small and relatively uniform spatially (Fukuhara and Yamauchi 1993; Salama and Ling 1980).

A combination of OBS and OSS can overcome some of the disadvantages of the OBS and OSS methods to achieve larger temperature compensation range and smaller size of baseline database. The combination of OBS and OSS was successfully used in experiments to detect flaw types of notches and holes in an aluminum plate (Lu and Michaels 2005) and to detect and localize holes in the door of a commercial shipping container with a corrugated steel panel under varying temperature conditions (Clarke et al. 2010).

1.3.2 Damage Quantification

Ultrasonic techniques are widely used for SHM of various engineering structures. The goal of SHM is to characterize the health state of a target structure, and such a characterization can be done by answering the following research questions (Rytter 1993):

(1) Is there any damage in the structure?

(2) Where is the damage in the structure?

(3) What kind of damage has occurred?

(4) How severe is the damage?

(5) How much useful life remains?

Currently, most ultrasonic techniques focus on the first two research questions, i.e. damage detection and localization. The kinds of damage in a specific engineering structure can often be known by expert knowledge, and different monitoring schemes can be designed for specific damage types. However, the last two research questions cannot be easily answered and currently only a few methods are available to perform damage quantification to some extent. Even when the available methods quantify damage, they typically apply only to simple structures with very specific damage types.

For example, ultrasonic Lamb waves with a specific selected mode are used to detect damage in aircraft panels using the pulse-echo method (Yu et al. 2008) and the pitch-catch method (Ihn and Chang 2008). Various damage types, such as delamination, cracks and holes, in composite materials can also be successfully detected using ultrasonic techniques (Ihn and Chang 2008; Keilers and Chang 1995; Kessler et al. 2002; Wang and Chang 1999; Yu et al. 2008). The ultrasonic A-scan technique is used to detect the corrosion or erosion pits on offshore risers, which connect the pipelines on the seabed with the pipe-work on the production platform. The reflected echoes appear clearly on A-scan results demonstrating the existence of corrosion pits, and they can clearly be differentiated from the echoes reflected back by welds (Edwards and Gan 2007).

For damage localization, Michaels et al. (Michaels et al. 2008) applied time-of-arrival and time-difference-of-arrival algorithms to signals collected on aluminum plates using PZT transducer arrays, and showed that these two algorithms could both successfully locate drilled holes on aluminum plates. Harley et al. (Harley and Moura 2014) introduced a data-driven matched field processing technique combining matched field processing with sparse wavenumber analysis to localize damage on aluminum plates. It was demonstrated that this technique could successfully localize two nearby drilled holes with much better accuracy than delay-based methods. Zhao et al. (Zhao et al. 2007) used pitch-catch ultrasonic signals, recorded from PZT discs, for damage localization on an aircraft wing in a laboratory environment. They developed a damage localization algorithm based on correlation analysis called RAPID (reconstruction algorithm for probabilistic inspection of defects) and showed that this algorithm had good performance for simulated cracks and for corrosion damage localization.

However, current ultrasonic methods can only quantify some specific damage types for simple structures. For example, the pulse-echo method is one of the most commonly used ultrasonic technique for wall thickness measurements for metal, plastic or glass (Lynnworth 2013). However, in my work (to be discussed in Chapters 2 and 3) on thick-walled frac iron components (retired from real-work applications due to erosion damage), the pulse echo method did not perform well for detecting localized volume loss; the morphology of volume loss was irregular and reflected ultrasonic pulses away from the transducer, making it difficult to detect an echo.

1.4 Dissertation Outline

One of my research visions is to develop ultrasonic techniques to solve EOCs caused complexities for damage detection and quantification. In this dissertation, Chapter 2 and Chapter 3 fall into this research vision. In Chapter 2, I will propose a modified OSS method and an SVD method for the ultrasonic damage detection under temperature variations. In Chapter 3, I will study the orthogonal relationship between the temperature-induced and damage-induced ultrasonic change signals. The orthogonal relationship is helpful when interpreting the results from SVD and will also be helpful for direct damage detection and quantification under temperature variations.

Another of my research visions is to develop ultrasonic techniques to quantify damages for different specific structural applications. In this dissertation, Chapter 4 and Chapter 5 fall into this research vision. In Chapter 4, I will propose the ultrasonic time-of-flight diffraction technique to quantify thickness loss in thick-walled aluminum tubes. The ultimate goal of this part of my research is to provide reliable techniques to quantify erosion damage in thick-walled frac iron components, where conventional ultrasonic pulse-echo method does not perform well. In Chapter 5, I will study the ultrasonic passband method to quantify ASR-caused cracking damage in concrete.

Chapter 2 Detection of Volume Loss in Thick-Walled Components Using Data-Driven Methods

2.1 Introduction

In the field of oil and natural gas production, frac iron is used to inject, eject, and control the flow of fracture fluid in a natural gas well. Frac iron components include pup joints, plug valves, swivel joints, fittings and so on. These frac iron components carry abrasive fluid at very high pressure rated as much as 15000 psi (Haddad et al. 2011) and are vulnerable to various damages, such as erosion, corrosion and cracking. They are examined after each service to determine whether they can continue to be used in the future. Despite these examinations, components explode with some frequency and cause fatalities, injuries, economic loss, and environmental damage.

The motivation of the research work in this chapter is to develop effective ultrasonic signal processing techniques to monitor the progress of erosion in frac iron components under EOCs. In this chapter, I will develop ultrasonic techniques to detect volume loss of an aluminum alloy tube instead of working directly on frac iron components. Aluminum alloy is chosen for our laboratory study for ease of machining volume loss similar to the erosion damage of our practical interest.

In this chapter, I will focus on data-driven methods to detect volume loss under varying temperature conditions. Data-driven methods are not sensitive to or specific to the structural geometry and material properties (Laory et al. 2011) and thus are more flexible for use on structures with complicated geometry like frac iron components. A method that is model-based, called ultrasonic time-of-flight diffraction, will be studied in Chapter 4 for this same application.

The structure of this chapter is organized as follows. In section 2.2, I will explain details of the experimental work for this chapter. In section 0, signal preprocessing procedures and OSS temperature compensation will be introduced for the damage detection purpose. The volume loss detection under varying temperature conditions will be discussed using the OSS method in section 2.5, using the modified OSS method in section 2.6, and using the SVD method in section 2.7. In sections 2.8 and 2.9, I will conclude and summarize the results in this chapter.

2.2 Experimental Design

This experiment is designed to study volume loss detection in thick-walled aluminum tubes using ultrasonic signal processing techniques. A thick-walled 6061 aluminum alloy tube with dimensions (O.D. x I.D. x length) of 4.00 x 2.00 x 3.15 inch (101.60 x 50.80 x 80.01 mm) is used as the test specimen as shown in Figure 2-1, which has cross-sectional dimensions closely comparable to frac iron elbows. Aluminum alloy is chosen for our laboratory study for ease of machining volume loss similar to the erosion damage of our practical interest. In this experiment, the ultrasonic transducers are Krautkramer probes from GE Inspection Technologies (product code: 113-241-591) with a specified center frequency of 0.98 MHz and a moderate bandwidth (@-6dB: ~70%). The two transducers are glued onto the specimen surface using cyanoacrylate adhesive with an included radial angle of 134.6º as shown in Figure 2-1(b).

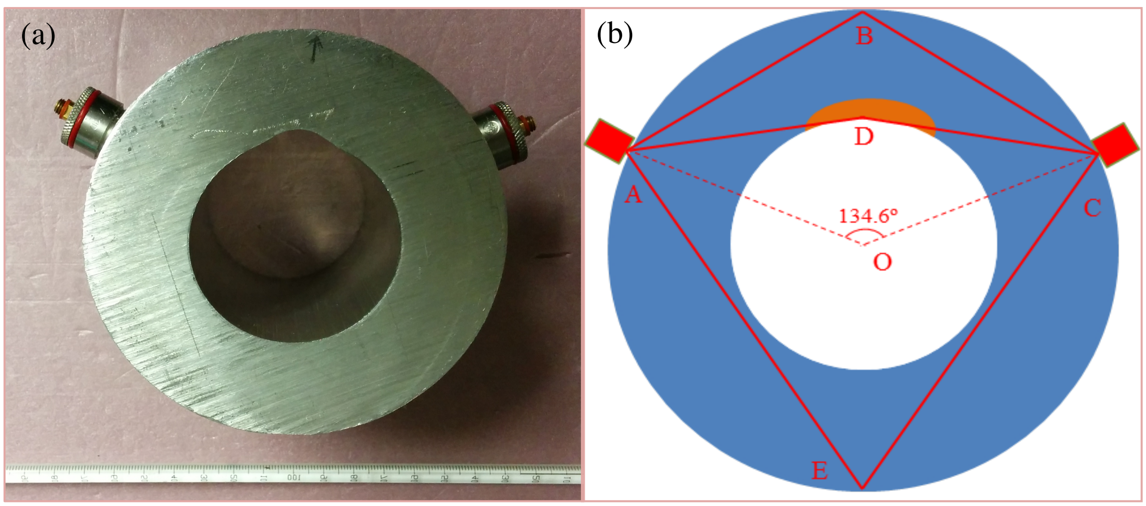

Figure 2-1 (a) The thick-walled aluminum tube and the transducers; (b) an illustration of possible wave paths

An NI PXI-5421 arbitrary waveform generator is used to generate a Gaussian-modulated sinusoidal pulse with peak-to-peak amplitude of 6.0 V at a center frequency of 1.0 MHz as shown in Figure 2-2. An NI PXI-5122 digitizer is used to record ultrasonic signals both in one-transducer mode and in two-transducer mode, with a sampling rate of 20 MHz. The same transducer is used as the emitter and receiver when operating in one-transducer mode, whereas one transducer is used as the emitter and the other is used as the receiver in two-transducer mode. To improve the signal-to-noise ratio, in this experiment each recorded ultrasonic signal is an average of 500 measurements, and each measurement (and therefore each averaged ultrasonic signal) has a duration of 0.2 ms. At each experimental step, ultrasonic signals are repeated 50 times with a 15 s interval between two consecutive signals.

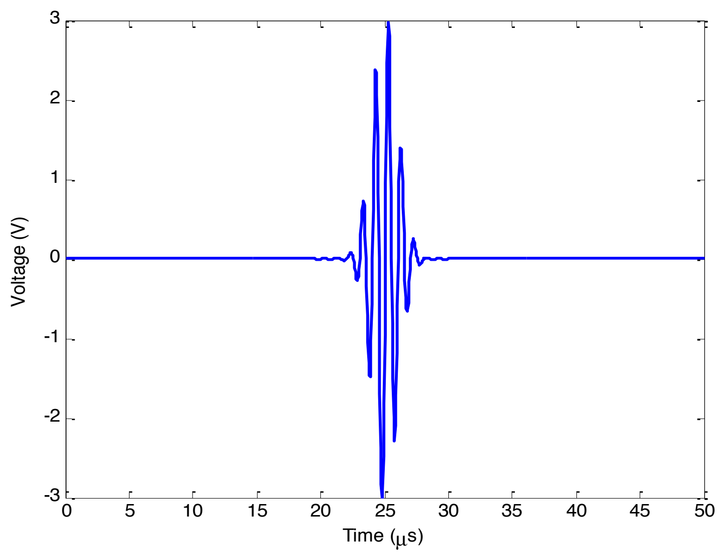

Figure 2-2 A Gaussian-modulated sinusoidal pulse

Volume loss in the thick-wall aluminum tube specimen is introduced in the following procedure. The experiment is designed to have a total of 37 test steps, and a Bernoulli random number generator is used to designate each test step either as an incremental damage condition or a null (no damage) condition. The 37 test steps contain 18 damage steps and 19 null steps produced from that random number generation process. At a damage step, mass loss between 0.3 g and 0.5 g is machined on the inside of the tube using a Dremel sanding drum tool. At a null step, no machining or other work is done to the specimen. The mass loss of the specimen at each step is plotted in Figure 2-3 and is listed in Table 2-1. The duration of each step consists of a fixed 40-minute interval required for processing and measurements, and a variable interval (the wait time in Table 2-1) corresponding to an exponentially distributed random variable with a mean of 40 minutes. The distribution of the variable interval is shown in Figure 2-4 as a histogram. The whole experiment spanned 52.7 hours, and temperature varied throughout that test period.

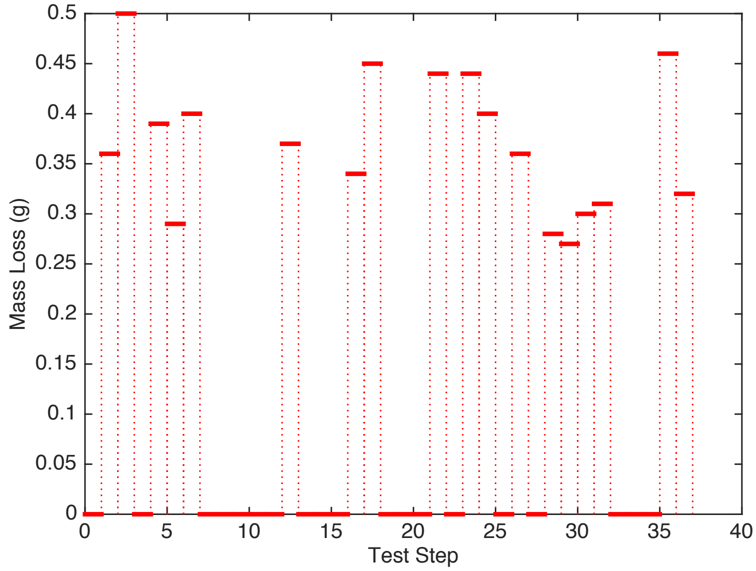

Figure 2-3 The mass loss of the thick-wall aluminum tube specimen at each test step

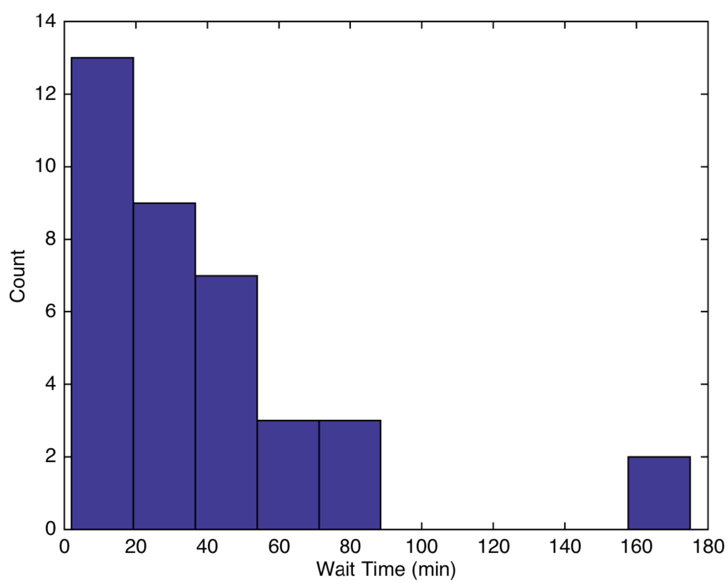

Figure 2-4 The histogram of the wait time. The count is the number of test steps with a specific wait time interval

Table 2-1 The mass loss and wait time at each test step

Test Step	Wait Time (min)	Mass Loss (g)	Test Step	Wait Time (min)	Mass Loss (g)	Test Step	Wait Time (min)	Mass Loss (g)
1	34	0.00	14	175	0.00	27	15	0.36
2	23	0.36	15	56	0.00	28	63	0.00
3	22	0.50	16	27	0.00	29	61	0.28
4	10	0.00	17	44	0.34	30	35	0.27
5	30	0.39	18	19	0.45	31	73	0.30
6	2	0.29	19	35	0.00	32	27	0.31
7	39	0.40	20	10	0.00	33	38	0.00
8	9	0.00	21	16	0.00	34	14	0.00
9	3	0.00	22	43	0.44	35	45	0.00
10	16	0.00	23	82	0.00	36	13	0.46
11	3	0.00	24	171	0.44	37	49	0.32
12	86	0.00	25	50	0.40			
13	18	0.37	26	21	0.00			
						Total:	**1477**	**6.68**

2.3 Signal Preprocessing

Although the ultrasonic signals are recorded in both one-transducer mode and two-transducer mode, only those from the one-transducer mode will be used for the study in this chapter. In this chapter, I will focus on data-driven methods. One of the advantages to using a data-driven method here is that ultrasonic waves can propagate circumferentially and sample the volume loss area repeatedly. Therefore, the circumferentially propagating ultrasonic waves can be very sensitive to damage in the form of volume loss. From this perspective, signals from one-transducer mode and two-transducer mode are similar, but the one-transducer mode is preferred for the practical reason of system simplicity.

2.3.1 Signal Filtering

Figure 2-5 shows two recorded ultrasonic signals from one-transducer mode at test steps 3 and 4 both with the same cumulative mass loss of 0.86 g, because test step 4 is a null step. The first large-amplitude pulse in Figure 2-5(a) is the emitted pulse, and its amplitude in Figure 2-5(a) is clipped in order to image the subsequent pulse arrivals at a useful scale. Several back-wall (reflection) pulse echoes follow immediately after the emitted pulse. From these echoes, the longitudinal wave velocity can be calculated as roughly 6.27 mm/μs. Phase shifts caused by temperature variations can be seen in in Figure 2-5(b) and Figure 2-5(c).

For purposes of damage detection, I do not make use of the emitted pulse and the following back-wall (reflected) echoes, so the segment of signal before 100μs is truncated. To prevent the sharp changes of signals caused by the signal truncation, a tapered cosine window is added to signals after truncation by the Matlab function *"tukeywin"* with the first and last 0.25% of the samples equal to parts of a cosine.

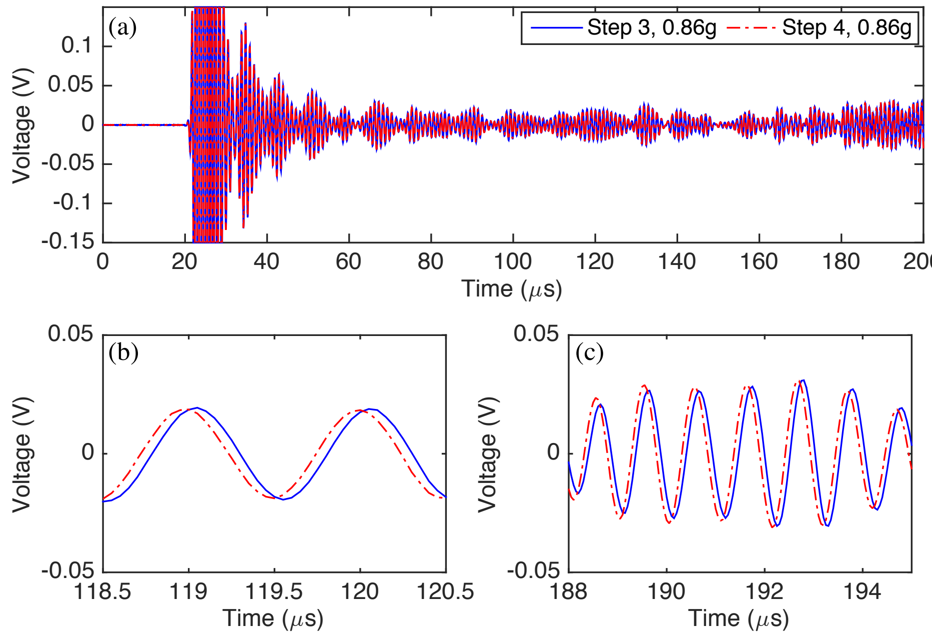

Figure 2-5 Two pulse-echo signals recorded at test steps 3 and 4 both with the same cumulative mass loss of 0.86 g (test step 4 is a null step); (a) the full record; (b) the 118.5-120.5 μs segment; (c) the 188-195 μs segment

2.3.2 Optimal Signal Stretching for Temperature Compensation

In the experiment, the volume loss of the thick-wall aluminum tube was machined by a Dremel sanding drum tool. The heat produced in the machining procedure significantly increased the temperature of the tube, which dropped after the machining procedure. Temperature compensation is important for successful detection of the volume loss of the aluminum tube in this varying temperature condition.

In this section, I will briefly discuss the optimal signal stretch (OSS) method for temperature compensation, and will use the OSS method as the baseline case for comparison in later sections of this chapter. The OSS method can be implemented in multiple ways with different performance in robustness, precision and computational speed (Croxford et al. 2010; Harley and Moura 2012).

In this dissertation, I will implement the OSS method using the scale transform. In this implementation, the optimal stretching factor estimate $\hat{\alpha}$ between the baseline signal $s_0(t)$ and a new signal $s_i(t)$ is defined as (Harley and Moura 2012),

$$\hat{\alpha} = \arg\min_{\alpha} \int_0^{\infty} \left| \frac{s_0(t)}{\sigma_0} - \frac{s_i(\alpha t)}{\sigma_i / \sqrt{\alpha}} \right|^2 dt \tag{2-1}$$

where the normalization factors are defined as,

$$\sigma_0^2 = \int_0^{\infty} |s_0(t)|^2 dt \tag{2-2}$$

$$\sigma_i^2 / \alpha = \int_0^{\infty} |s_i(\alpha t)|^2 dt \tag{2-3}$$

Then, the optimal stretch factor estimate $\hat{\alpha}$ can be simplified as,

$$\begin{aligned} \hat{\alpha} &= \arg\min_{\alpha} \int_0^{\infty} \frac{|s_0(t)|^2}{\sigma_0^2} + \frac{|s_i(\alpha t)|^2}{\sigma_i^2 / \alpha} - 2\frac{s_0(t) s_i(\alpha t)}{\sigma_0 \sigma_i / \sqrt{\alpha}} dt \\ &= \arg\max_{\alpha} \frac{\sqrt{\alpha}}{\sigma_0 \sigma_i} \int_0^{\infty} s_0(t) s_i(\alpha t) dt \end{aligned} \tag{2-4}$$

The stretching is energy-preserving because

$$\int_0^{\infty} \left| \sqrt{\alpha} s_i(\alpha t) \right|^2 dt = \int_0^{\infty} |s_i(t)|^2 dt \tag{2-5}$$

In the later part of this section, I will focus on the application of the OSS method to the ultrasonic signals collected in my experiment; more details about obtaining the optimal stretching factor estimate $\hat{\alpha}$ (using scale transform), and the computational cost and resolution of this implementation, can be found in (Harley and Moura 2012).

After the signal filtering procedure in section 2.3.1, a new arrival (signal) is stretched according to Eq. (2-1) to match the baseline signal. Figure 2-6 shows two signals before the OSS temperature compensation, and Figure 2-7 shows two signals after OSS temperature compensation. From Figure 2-6, the signals have significant phase shifts after a relatively small temperature change of 2.0 °C, whereas Figure 2-7 shows that the phase shifts are negligible after OSS temperature compensation. However, the phase shifts cannot be fully corrected after a relatively large temperature change of 8.0 °C as shown in Figure 2-8 and Figure 2-9.

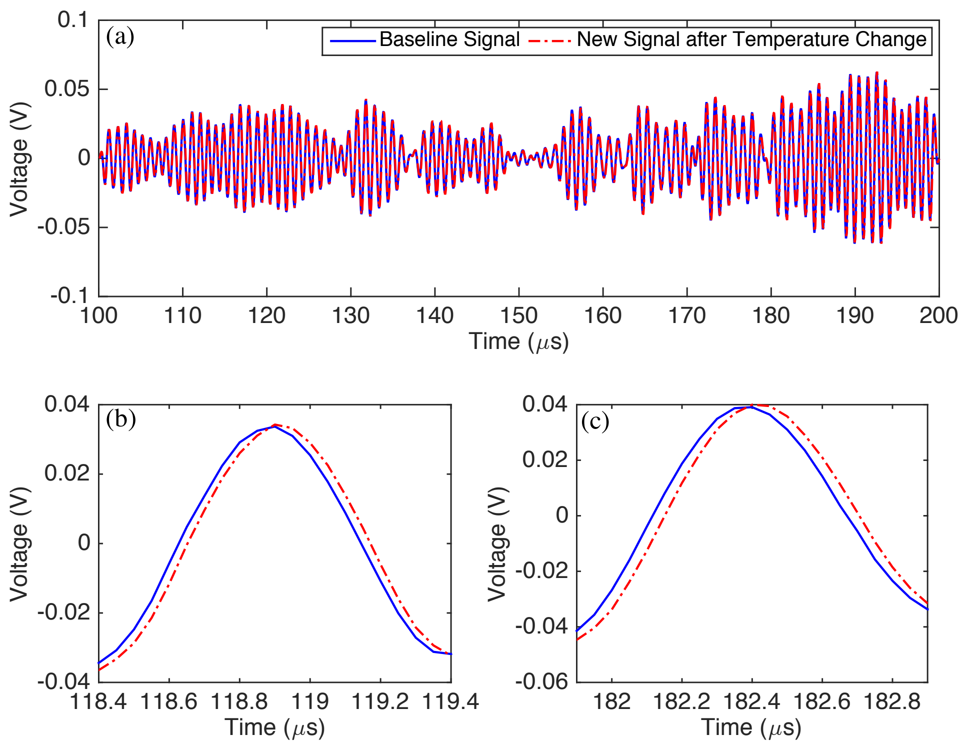

Figure 2-6 Two ultrasonic signals with a relative small temperature change of 2.0 °C but without volume loss before the OSS temperature compensation: (a) the 100.0-200.0 μs segment; (b) the 118.4-119.4 μs segment; (c) the 181.9-182.9 μs segment

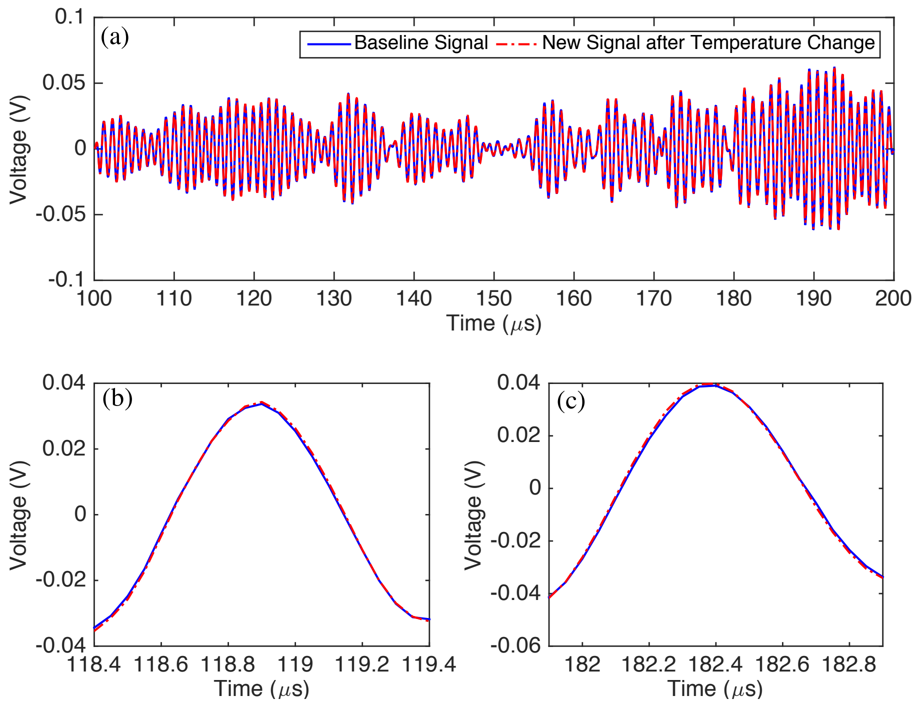

Figure 2-7 Two ultrasonic signals with a relatively small temperature change of 2.0 °C, but without volume loss, after OSS temperature compensation: (a) the 100.0-200.0 μs segment; (b) the 118.4-119.4 μs segment; (c) the 181.9-182.9 μs segment

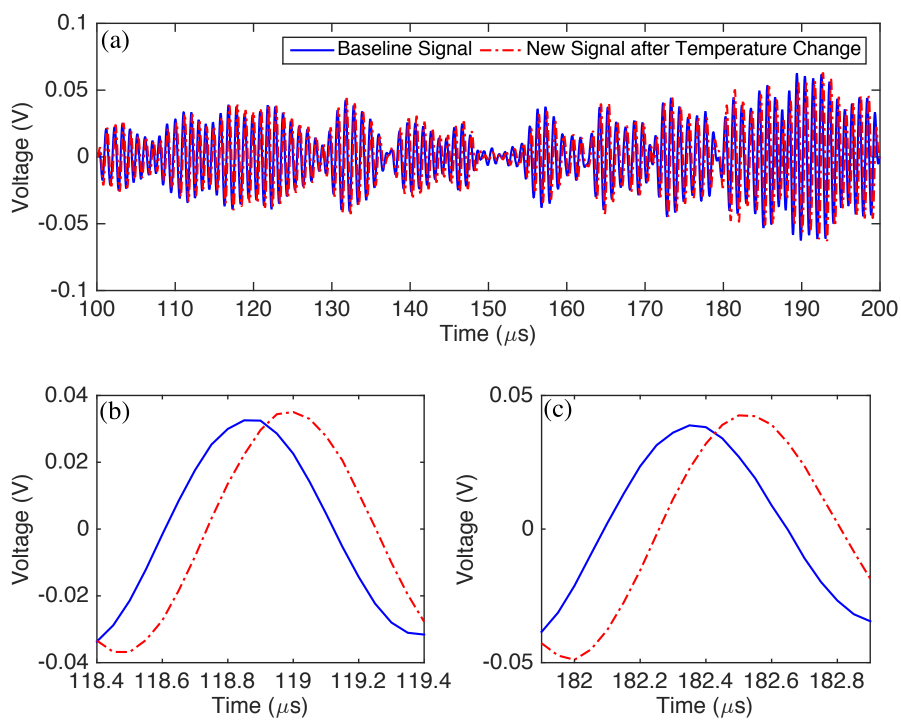

Figure 2-8 Two ultrasonic signals with a relatively large temperature change of 8.0°C, but without volume loss, before OSS temperature compensation: (a) the 100.0-200.0 μs segment; (b) the 118.4-119.4 μs segment; (c) the 181.9-182.9 μs segment

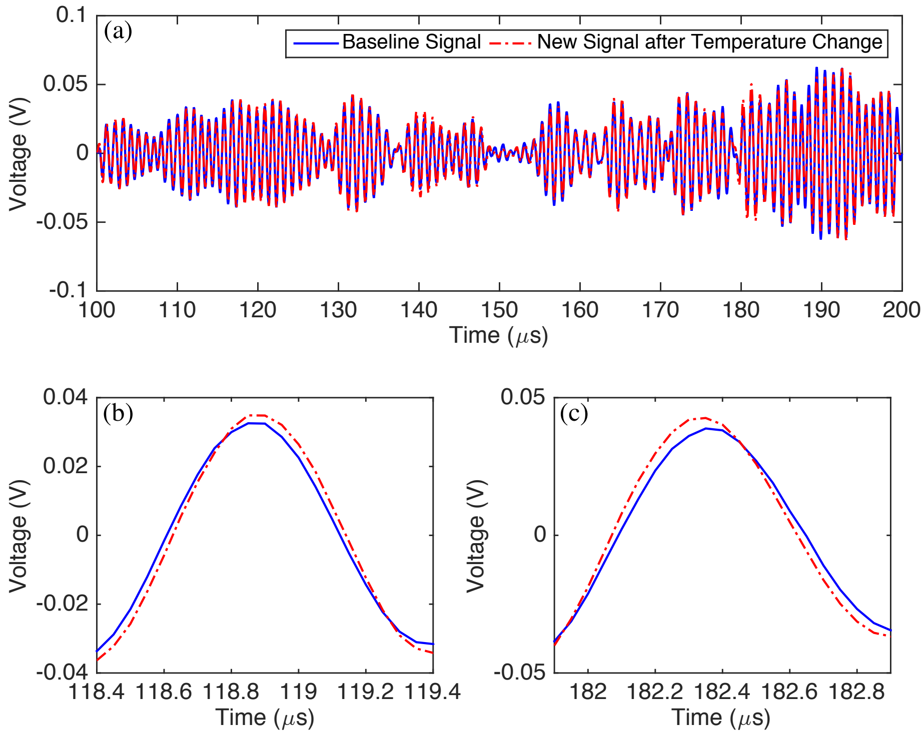

Figure 2-9 Two ultrasonic signals with a relatively large temperature change of 8.0 °C, but without volume loss, after OSS temperature compensation: (a) the 100.0-200.0 μs segment; (b) the 118.4-119.4 μs segment; (c) the 181.9-182.9 μs segment

The temperature changes in this experiment are in the range of about ±8 °C. Temperature changes are inferred from stretching factors, and the details about inference of temperature changes from stretching factors will be given in section 2.4.

2.4 Temperature Change Characterization

In this experiment, the temperature changes of the specimen were not directly measured. However, it is known that temperature changes are directly related to stretching factors (Harley and Moura 2012; Lu and Michaels 2005), so temperature changes are characterized in stretching factors instead of in (temperature) degrees in this chapter.

To demonstrate the direct relation between temperature changes and stretching factors, an additional experiment was carried out on the same specimen with the same transducer and experimental setups used in the experiment described in section 2.2. In this additional experiment, the ambient temperature was adjusted, and ultrasonic signals were recorded at five different ambient temperature levels using a thermometer with a precision of 0.1°C. To make the ambient temperature as close to the internal temperature of the specimen as possible, the ambient temperature was kept at each temperature level for five hours to stabilize the internal temperature of the specimen. The first two echoes from back-wall reflections are used to extract the stretching factors using Eq. (2-1), and subscript indices for both signals can range from 1 to 5 in Eq. (2-1). If the temperature change is positive when the ultrasonic signal pair ($s_i(t)$, $s_j(t)$) is used to calculate the stretching factor, the temperature change would be negative when the ultrasonic signal pair ($s_j(t)$, $s_i(t)$) is used to calculate the stretching factor.

The relation between stretching factors and temperature changes in the additional experiment is shown in Figure 2-10. It is shown that the stretching factor is equal to 1 when there is no temperature change, and that stretching factors have a strong linear relationship with temperature change with R^2 = 0.98. This strong linear relationship is consistent with that found in (Lu and Michaels 2005). The noise in the data is mainly from the temperature measurements and from the difference between the ambient temperature and the internal temperature of the specimen. This is the main reason that I prefer to use stretching factors to characterize the temperature changes.

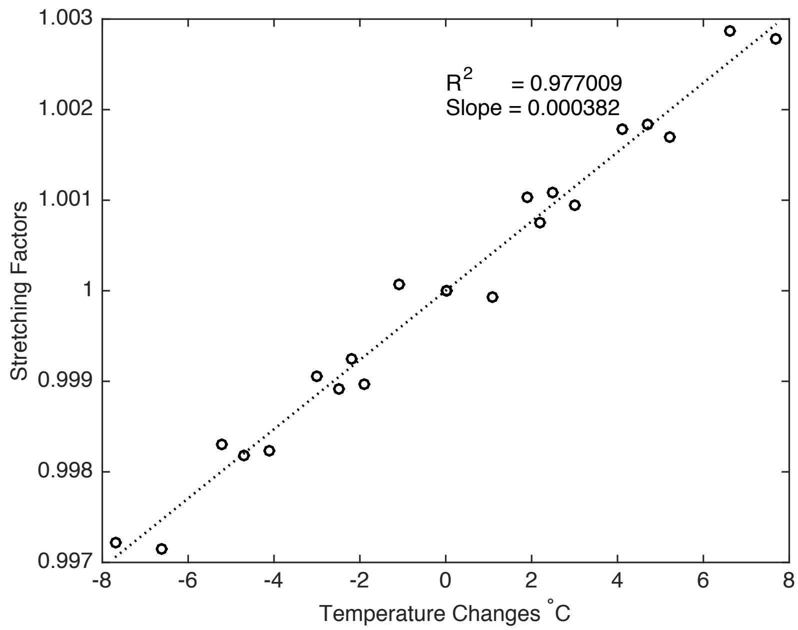

Figure 2-10 Relation between stretching factors and temperature changes

In order to use the data collected in the experiment in section 2.2, I must make an important assumption that the first two pulse echoes from back-wall reflections are not significantly affected by damage. This assumption is reasonable because the potential erosion damage location in frac iron components is foreseeable from the flow geometry, and the transducer location (where the through-thickness back-wall reflections occur) can be situated outside of that potential damage location. In oil and gas production, the flow direction is fixed, and therefore the particulate matter in the fluid will always impact the same general area when flowing through an elbow. Therefore, the erosion damage pattern is largely predictable; I observed the same erosion damage pattern in all four frac iron elbow specimens that I studied. (These four elbow specimens were retired from service because of the erosion damage, and our industrial partner transferred them to us for study in our lab.) The in-service erosion damage pattern is similar to what I created on the aluminum tube specimen as shown in Figure 2-1. If the transducer is located sufficiently distant from the erosion damage location as shown in Figure 2-1, the first two pulse echoes from back-wall reflection are not significantly affected by the erosion damage, because no damage is present on the through-thickness path.

To confirm the above assumption, I analyzed the 1850 ultrasonic signals collected from the experiment in section 2.2. First, a typical ultrasonic signal is shown in Figure 2-11(a). The segment of the signal between 32 and 48 μs corresponds to the first two pulse echoes from back-wall reflections and are shown in Figure 2-11(b). The segment of the signal between 150 and 166 μs corresponds to later arrivals and are shown in Figure 2-11(c). The first signal of the experiment was used as the baseline, and all other signals were stretched against that baseline. The correlation coefficients before stretching, the stretching factors, and the correlation coefficients after stretching are shown in Figure 2-12, using the signal segment between 32 and 48 μs for the stretching analysis, and are shown in Figure 2-13, using the signal segment between 150 and 166 μs for the stretching analysis.

From Figure 2-12(c), the minimum correlation coefficient is 0.9993 after stretching, which is very close to 1. This indicates that the first two pulse echoes are not significantly affected by damage effects, as expected. From Figure 2-13(c), the minimum correlation coefficient is 0.9429, which is much less than that in Figure 2-12(c). This means that this segment of signal may be significantly affected by damage effects.

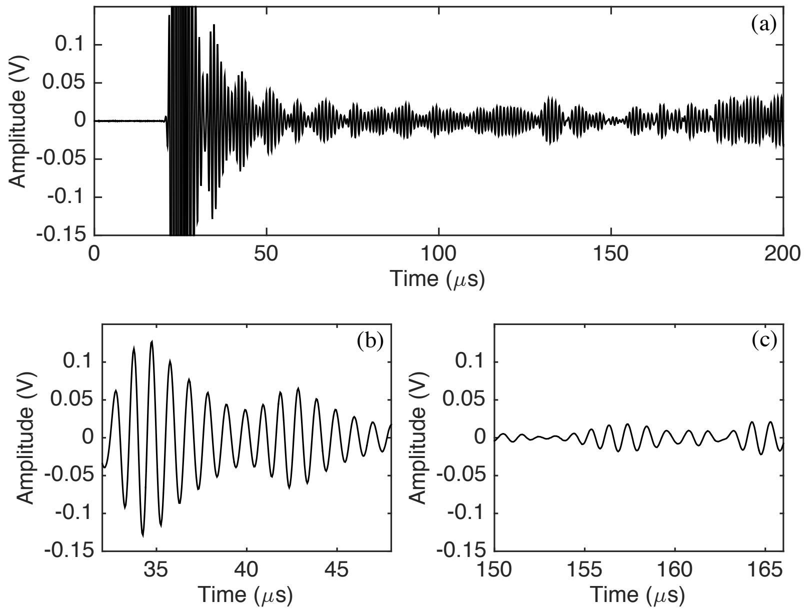

Figure 2-11 (a) A typical ultrasonic signal; (b) the first two pulse echoes from back-wall reflections; (c) some later arrivals of the ultrasonic signal

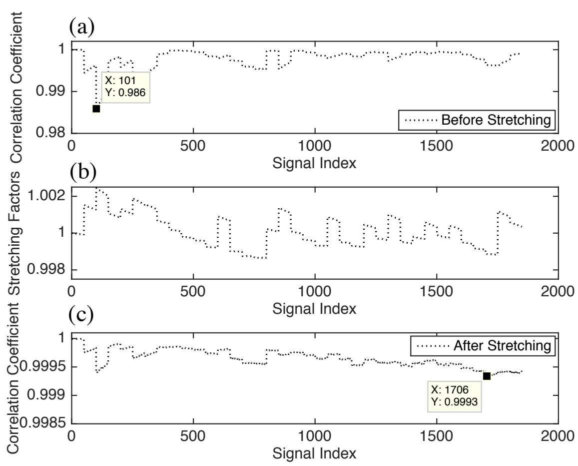

Figure 2-12 Analysis using signals between 32 and 48 μs corresponding to the first two pulse echoes: (a) correlation coefficients before stretching; (b) stretching factors; (c) correlation coefficients after stretching

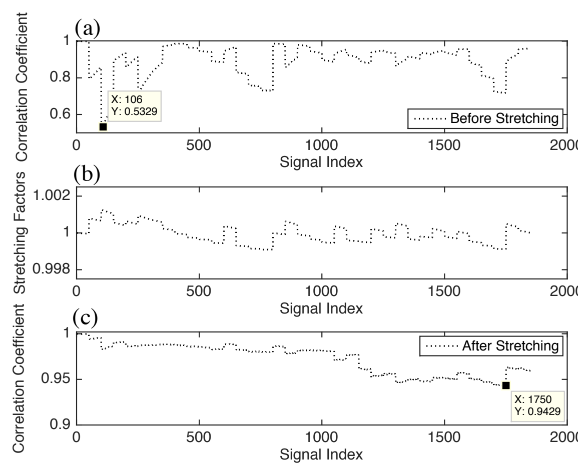

Figure 2-13 Analysis using signals between 150 and 166 μs corresponding to later arrivals: (a) correlation coefficients before stretching; (b) stretching factors; (c) correlation coefficients after stretching

From the discussion in this section, I conclude that there is a strong linear relationship between stretching factors and temperature changes, and that the first two pulse echoes are not significantly affected by damage effects. Therefore, stretching factors extracted from the first two pulse echoes can be used to characterize the temperature changes in the thick-wall aluminum tube.

2.5 Detection of Volume Loss Using the OSS Method

2.5.1 MSE

Defects in materials can cause shape distortion of the ultrasonic waveforms. A simple method for SHM is to record ultrasonic signals before damage (the baseline) and after damage (a new arrival), and then to examine the residuals obtained by subtracting the baseline from the new arrival. Further analysis of the residuals can be used to detect the damage, such as the mean squared errors (MSE) of residuals. If there are temperature variations, MSE should be calculated after performing temperature compensation.

In this chapter, each test step in the experiment in section 2.2 is considered as an individual damage detection task. In the experiment, the 19 test steps with volume loss are labeled as 1, and the 18 test steps without volume loss are labeled as 0. MSE is then used as the predictor variable to predict whether or not volume loss is present. Here, MSE is defined as in Eq. (2-6). It is the mean squared residual signal, and the residual signal is the difference between the new arrival (after OSS temperature compensation) and the baseline signal.

$$MSE_i = \frac{1}{N}\sum_{t=1}^{N}(s_i(t) - s_{i-1}(t))^2 \tag{2-6}$$

where MSE_i is the MSE at experimental step i, $s_i(t)$ is the new arrival (after OSS temperature compensation) at step i, $s_{i-1}(t)$ is the signal from test step i-1 (and the baseline signal for step i) and N is the signal length.

2.5.2 Results and Discussions

In this section, the logistic regression model is used as the classifier and MSE is used as the predictor variable. The measured data and the best fit of the logistic regression model are shown in Figure 2-14. The circles are those steps without volume loss and the crosses are those steps with volume loss. The dotted line is the best fit of the logistic regression model using all the data as training set. From this figure, the raw data are not well separated by the predictor variable MSE.

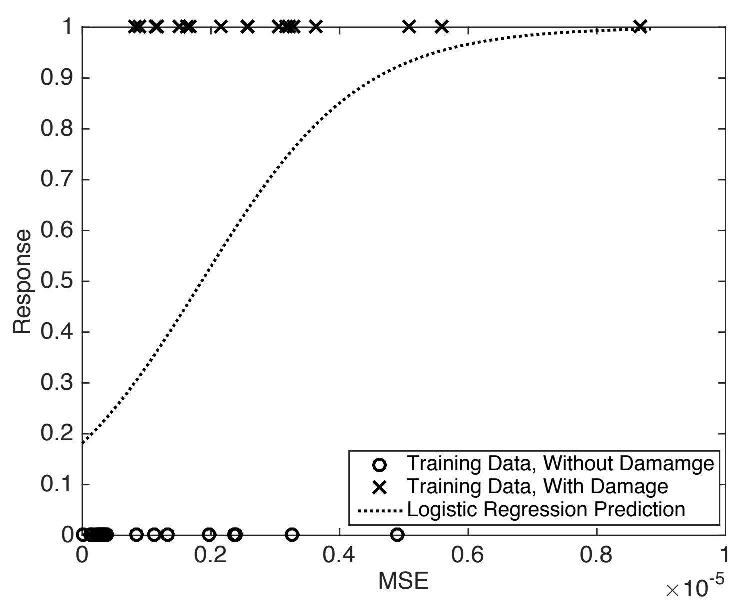

Figure 2-14 Damage detection using the logistic regression model and using MSE as the predictor variable

To know the performance of the prediction from the logistic regression model, a threshold between 0 and 1 must be selected for the logistic regression model to give binary prediction results. Usually, it can be selected as 0.5, and then the outputs greater than 0.5 from logistic regression are labeled as steps with volume loss and the outputs less than 0.5 are labeled as steps without volume loss. However, if the threshold is selected as a value greater than 0.5, there will be fewer Type I errors but more Type II errors. Similarly, if the threshold is selected as a value less than 0.5, there will be fewer Type II errors but more Type I errors. The selection of this threshold should reflect the tolerance level of Type I and Type II errors of users.

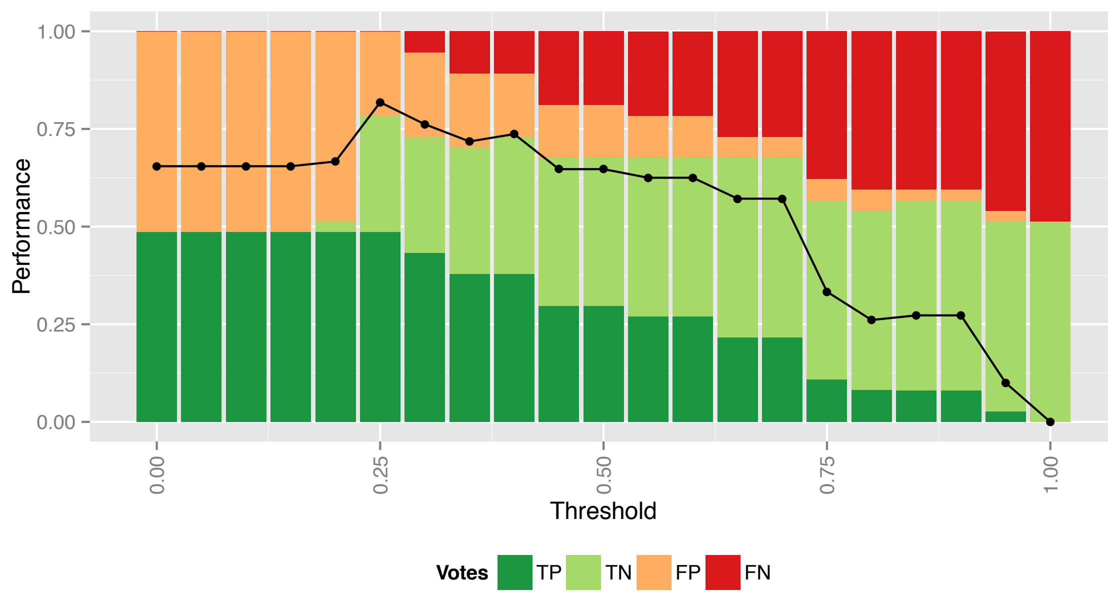

Figure 2-15 Performance of the logistic regression model using MSE as the predictor variable at different threshold values. The black line is the F1 score at each threshold level.

The performance of the logistic regression model using MSE as the predictor variable is shown in Figure 2-15 at different threshold levels, and the calculation of this performance uses leave-one-out cross validation. At each threshold level, the percentage of true positive (TP), true negative (TN), false positive (FP), and false negative (FN) predictions are shown separated in Figure 2-15. [1]The black line is the F_1 score at each threshold level to show the overall performance of the prediction model (Gao et al. 2015). In Figure 2-15, the highest F_1 score and accuracy are 0.78 and 0.82, respectively. These results are better than a random guess but far from satisfactory.

2.6 Detection of Volume Loss Using the Modified OSS Method

In the previous section 2.5, MSE after OSS temperature compensation was used for damage detection of volume loss in the thick-wall aluminum tube, but the performance was not satisfactory. The problem was that the OSS method could not fully correct the phase shifts and shape distortions caused by relatively large temperature changes as shown in Figure 2-8 and Figure 2-9 although it performed better when the temperature changes were relatively small as shown in Figure 2-6 and Figure 2-7. In this section, I will propose a modified OSS method to improve the performance for temperature compensation.

2.6.1 The Modified OSS Temperature Compensation

The idea of my modified OSS method is to calibrate the changes of a damage indicator (like MSE) that are caused by temperature changes, using data obtained when no change occurs in the damage. In my experiment, there were at least four segments in which no incremental volume loss occurred; for example, from test step 7 to 12, from test step 13 to 16, from test step 18 to 21, and from test step 32 to 35, as shown by the arrows in Figure 2-16. In

[1] F_1 score is defined as $F_1 = 2 \cdot \frac{precision \cdot recall}{precision + recall}$, where $precision = \frac{true\ positives}{true\ positives + false\ positives}$ and $recall = \frac{true\ positives}{true\ positives + fase\ negatives}$

this section, the data from these four segments is used to study the changes in the MSE caused by temperature changes.

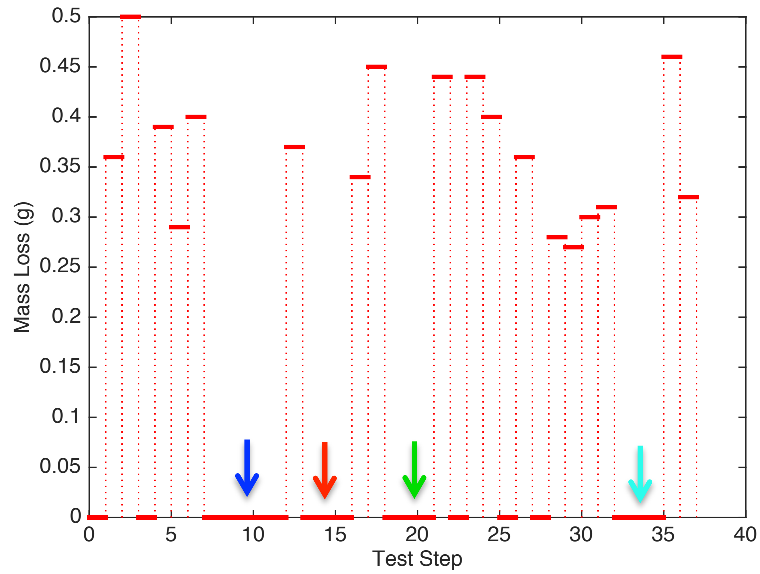

Figure 2-16 The data used for training the modified OSS temperature compensation are from four segments of the experiment as shown by the arrows

Figure 2-17 shows the relationship between MSE and temperature change, characterized by stretching factor, when there is no volume loss. Before OSS temperature compensation, MSE increases with the increase of temperature change, with a polynomial relationship as shown by the equation and R-squared in Figure 2-17(a). After OSS temperature compensation, the magnitude of MSE drops by an order of 10^2. However, the strong polynomial pattern still exists as shown in Figure 2-17(b), indicating that the OSS method cannot fully remove the temperature effects, and this polynomial pattern should be removed (compensated) in order to have better performance in damage detection.

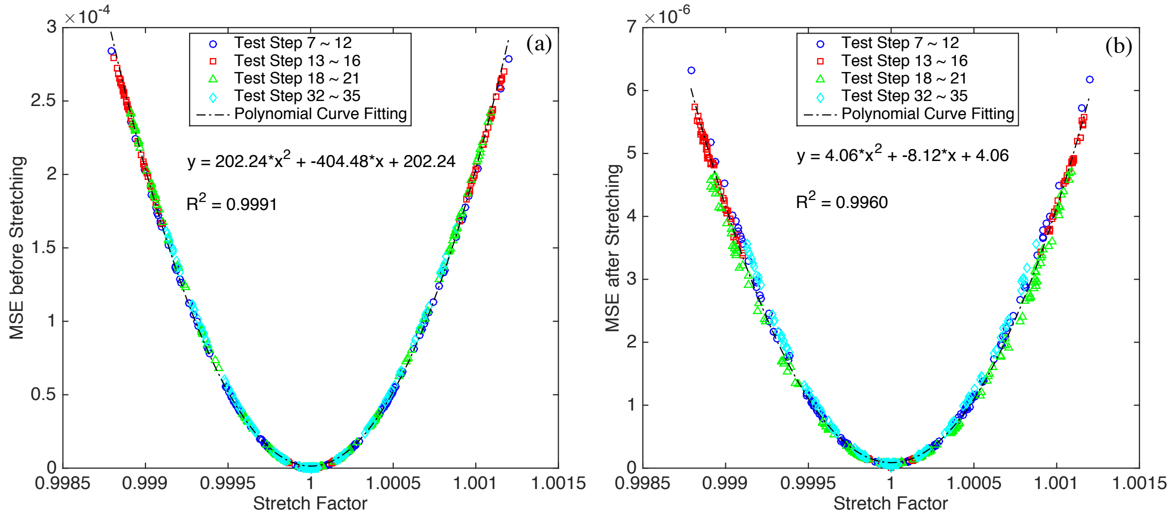

Figure 2-17 MSE when there was no volume loss: (a) before OSS temperature compensation; (b) after OSS temperature compensation

The procedure of the modified OSS temperature compensation is to carry out the temperature compensation in two phases. In the first phase, the OSS method is used on the experimental data for first-order temperature compensation, and the stretching factor is calculated between the baseline signal and the new arrival. In the second phase, the damage indicator (such as MSE) is calibrated based on the stretching factor calculated from the first phase, and then based on the trained model between the stretching factor and the damage indicator when there is no damage (after OSS temperature compensation) like the polynomial model shown in Figure 2-17(b). I call this temperature compensation strategy the modified OSS method because the first phase is the OSS method, and the second phase of this strategy is still based on the stretching factor from the OSS method.

2.6.2 Results and Discussions

As in section 2.5.2, a logistic regression model is used as the classifier. The measured data and the best fit of the logistic regression model are shown in Figure 2-18. The circles are those steps without volume loss and the crosses are those steps with volume loss. The dotted line is the best fit from the logistic regression model using all the data as training set.

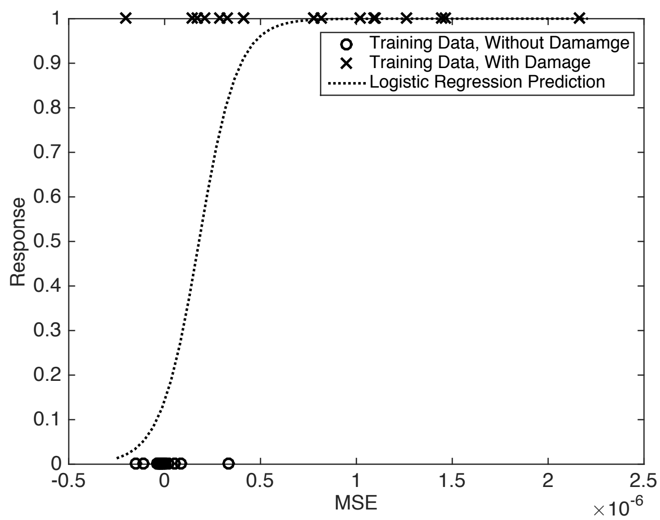

Figure 2-18 Damage detection using the logistic regression model and using the modified MSE as the predictor variable

The performance of the logistic regression model using the modified MSE as the predictor variable is shown in Figure 2-19 at different threshold levels, and the calculation of this performance uses leave-one-out cross validation. At each threshold level, the percentage of true positive (TP), true negative (TN), false positive (FP), and false negative (FN) predictions are shown separated in Figure 2-19. The black line is the F_1 score at each threshold level to shown the overall performance of the prediction model. In Figure 2-19, the highest F1 score and the accuracy are 0.94 and 0.95 respectively.

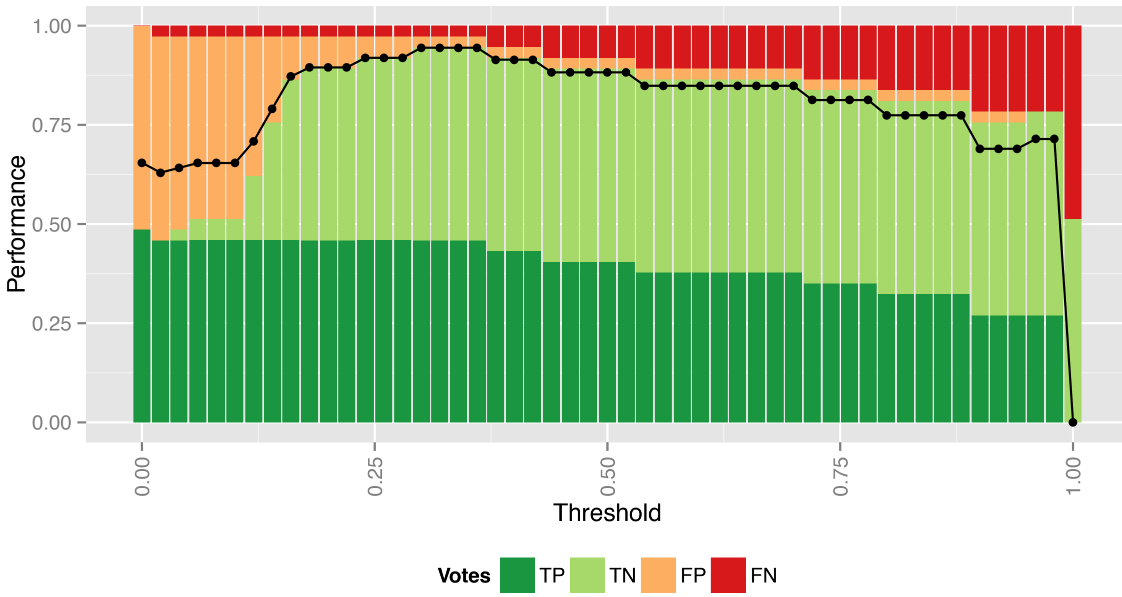

Figure 2-19 Performance of the logistic regression model using the modified MSE as predictor variable at different threshold values. The black line is the F_1 score at each threshold level.

2.7 Detection of Volume Loss Using Singular Value Decomposition

2.7.1 Singular Value Decomposition

Singular value decomposition (SVD) is closely related to principal component analysis (PCA). They are so closely related to each other that they are often used interchangeably. According to Jolliffe (Jolliffe 2002), "*Beltrami (1873) and Jordan (1874) independently derived the singular value decomposition (SVD) in a form that underlies PCA*", and the PCA technique was first given by Pearson (1901) and Hotelling (1933). However, these techniques were not extensively studied and used until the availability of digital computers for large-scale problems.

Now, SVD and PCA techniques are widely used in a variety of engineering fields including face recognition (Zhang et al. 2005; Zhao et al. 1998), image compression (Bryt and Elad 2008; Clausen and Wechsler 2000), signal denoising (Jade et al. 2003; Jha and Yadava 2011; Zhang et al. 2010), etc. In the field of damage detection and structural health monitoring, SVD and PCA are extensively studied to reduce data dimension (Mujica et al. 2008; Zang and Imregun 2001), to remove variations caused by environmental and operational conditions (Laory et al. 2011; Ruotolo and Surace 1999; Vanlanduit et al. 2005; Yan et al. 2005; Yan et al. 2005), and to extract damage sensitive feature for damage detection and clustering (Anton et al. 2009; Gharibnezhad et al. 2011; Mujica et al. 2011).

For example, (Anton et al. 2009) present the promising application of PCA-based methods for the detection and localization of the corrosion damage at several different locations on aluminum plates. In this paper, PZT transducer patterns are very carefully designed and pitch-catch measurements of Lamb waves between selected transducer pairs are recorded for further analysis. The PCA-based methods are then used to detect and select the transducer pairs corresponding to the Lamb wave paths with corrosion damage.

Cross et al. (Cross et al. 2012) proposed a novel method based on PCA, which can successfully detect damage under varying temperature conditions. In their experiment, two PZT transducers are placed on the opposite edges of a rectangular composite panel and Lamb waves are emitted from one transducer and received by the other under varying temperature in the chamber. A circular hole is drilled on a composite panel as the case for damage detection. In their method, signals with temperature variations before damage are used as baseline data, and the principal components are extracted from the baseline data. The largest variation in the data is caused by temperature change, so the first several principal components are removed, and then some minor principal components are used for data detection. This novel application of PCA has the potential to detect damage under varying environmental and operational conditions.

In earlier work at Carnegie Mellon, Liu et al. proposed a novel SVD technique using ultrasonic guided waves to detect a mass scatterer on a pipe, both in the laboratory environment and under operational conditions (Liu et al. 2012; Liu et al. 2015; Liu et al. 2012; Liu et al. 2013). The SVD technique can separate the damage effects and temperature effects into different singular values. By finding a specific pattern in the left singular vectors corresponding to damage effects, this SVD technique can achieve very good performance for mass scatterer detection, both in the laboratory environment and under operational conditions. Furthermore, this SVD technique can also be used for scatterer localization on pipes by using the corresponding right singular vectors (Liu et al. 2014).

In most of these prior applications, the directions with large variations in the data are assumed to be important data structures containing useful information. On the other hand, the data structures along directions with small variations are assumed to be unimportant or caused by noise. Therefore, image compression, dimension reduction, and signal denoising are achieved by discarding singular values smaller than a given threshold.

2.7.1.1 **Principal Component Analysis (PCA)**

Assume a two-dimensional dataset $\boldsymbol{X}$ with dimension of $m \times n$. In $\boldsymbol{X}$, each row represents an observation and each column represents a feature. Also assume that each feature has been mean normalized in $\boldsymbol{X}$. Then, the covariance matrix for the dataset $\boldsymbol{X}$ (an $m \times n$ matrix) is defined as follows,

$$C_X \equiv \frac{1}{n} X^T X \tag{2.7}$$

The covariance matrix C_X is an $n \times n$ matrix. The element $C_X(i,j) = \frac{1}{n} x_i^T x_j$ is the dot product between the measurements of the i^{th} feature and the measurements of j^{th} feature. Since our data are preprocessed to have zero mean, $C_X(i,j)$ is the covariance of the two features and C_X is the covariance matrix. (If the data is not mean normalized, C_X would not be the covariance matrix.)

Large values in diagonal terms of C_X are assumed to correspond to interesting structure in SVD or PCA analysis. On the other hand, large values in off-diagonal terms of C_X correspond to high redundancy because a large off-diagonal term means one feature is well correlated to another.

In PCA analysis, the goal is to find a linear transformation after which the interesting structure in the data is retained and the redundancy is removed. Define an $n \times m$ matrix P, which transforms the matrix X into Y,

$$Y = XP \tag{2.8}$$

Now, the goal is to find a transform matrix P to make the covariance matrix $C_Y = \frac{1}{n} Y^T Y$ to be diagonal. This is because diagonal terms of a covariance matrix correspond to interesting structure, and off-diagonal terms correspond to redundancy in the data as stated earlier.

Note that to assure that $\boldsymbol{C}_Y = \frac{1}{n}\boldsymbol{Y}^T\boldsymbol{Y}$ is indeed the covariance matrix of $\boldsymbol{Y}$, $\boldsymbol{Y}$ must have a zero mean. This can be proved as follows,

$$Y = \begin{bmatrix} y_1 \\ y_2 \\ \vdots \\ y_m \end{bmatrix} = \begin{bmatrix} x_1 \\ x_2 \\ \vdots \\ x_m \end{bmatrix} [\ p_1 \quad p_2 \quad \cdots \quad p_n\ ] = \begin{bmatrix} x_1p_1 & x_1p_2 & \cdots & x_1p_n \\ x_2p_1 & x_2p_2 & \cdots & x_2p_n \\ \vdots & \vdots & \ddots & \vdots \\ x_mp_1 & x_mp_2 & \cdots & x_mp_n \end{bmatrix} \tag{2.9}$$

$$\begin{aligned} \bar{Y} &= \begin{bmatrix} \frac{1}{m}\sum_{i=1}^{m} p_1x_i & \frac{1}{m}\sum_{i=1}^{m} p_2x_i & \cdots & \frac{1}{m}\sum_{i=1}^{m} p_nx_i \end{bmatrix} \\ &= \begin{bmatrix} \frac{1}{m}p_1\cdot 0 & \frac{1}{m}p_2\cdot 0 & \cdots & \frac{1}{m}p_n\cdot 0 \end{bmatrix} \\ &= \begin{bmatrix} 0 & 0 & \cdots & 0 \end{bmatrix} \end{aligned} \tag{2.10}$$

Now $\boldsymbol{C}_Y$ can be rewritten as,

$$\boldsymbol{C}_Y = \frac{1}{n}\boldsymbol{Y}^T\boldsymbol{Y} = \frac{1}{n}(\boldsymbol{XP})^T\boldsymbol{XP} = \frac{1}{n}\boldsymbol{P}^T(\boldsymbol{X}^T\boldsymbol{X})\boldsymbol{P} = \boldsymbol{P}^T(\boldsymbol{C}_X)\boldsymbol{P} \tag{2.11}$$

To make $\boldsymbol{C}_Y$ diagonal, PCA assumes $\boldsymbol{P}$ is an orthonormal matrix. From eigen analysis of linear algebra, $\begin{bmatrix} p_1 & p_2 & \cdots & p_n \end{bmatrix}$ are the eigenvectors of $\boldsymbol{C}_X$ and they are called principal components in PCA. The 1st principal component represents the direction with the greatest variance in the dataset $\boldsymbol{X}$, and similarly the ith principal component represents the direction with the ith greatest variance in the dataset $\boldsymbol{X}$ while satisfying the constraint that the ith principal component must be orthogonal to the first i-1 principal components. The diagonal terms $\begin{bmatrix} \lambda_1 & \lambda_2 & \cdots & \lambda_n \end{bmatrix}$ of $\boldsymbol{C}_Y$ are the eigenvalues of $\boldsymbol{C}_X$, and these eigenvalues indicate the variances along those principal components.

2.7.1.2 **Singular Value Decomposition (SVD)**

Let $\boldsymbol{X}$ the original dataset be an $m \times n$ matrix. In $\boldsymbol{X}$, each row represents an observation and each column represents a feature. Assume each feature has been mean normalized in $\boldsymbol{X}$ when SVD is performed in this dissertation, although the mean normalization is not necessary for general SVD analysis.

The singular value decomposition (SVD) of the dataset $\boldsymbol{X}$ is defined as,

$$\boldsymbol{X} = \boldsymbol{U}\boldsymbol{S}\boldsymbol{V}^{T} \tag{2.13}$$

where $\boldsymbol{U} = [\boldsymbol{u}_1, \boldsymbol{u}_2, ..., \boldsymbol{u}_m]$ is the left singular vector matrix with the dimension of $m \times m$, $\boldsymbol{S}$ is the diagonal singular value matrix with the dimension of $m \times m$ whose diagonal terms $[\sigma_1, \sigma_2, ..., \sigma_m]$ are called singular values, and $\boldsymbol{V} = [\boldsymbol{v}_1, \boldsymbol{v}_2, ..., \boldsymbol{v}_m]$ is the right singular vector matrix with the dimension of $n \times m$. Both the left and the right singular matrices are orthonormal matrices. The singular value matrix is sorted in descending order in the decomposition. Therefore, the 1st right singular vector represents the direction with the greatest variance in the dataset $\boldsymbol{X}$, and similarly the i^{th} right singular vector represents the direction with the i^{th} greatest variance in the dataset $\boldsymbol{X}$, while satisfying the constraint that the i^{th} right singular vector must be orthogonal to the first i-1 right singular vectors.

2.7.1.3 **The Relationship between PCA and SVD**

In practice, singular value decomposition (SVD) and principal component analysis (PCA) are so intimately related to each other that they are often used interchangeably. Their relationship can be described by the following equations,

$$X^T X = (USV^T)^T USV^T = VS^T U^T USV^T = VS^T SV^T \tag{2.14}$$

Then,

$$S^T S = V^T (X^T X) V \tag{2.15}$$

Comparing Eq. (2.15) to Eq. (2.7), the right singular vectors in SVD are exactly the principal components in PCA, and the singular values and the eigenvalues are related to each other according to the relationship $\sigma_i^2 / m = \lambda_i$ when the dataset is mean normalized.

2.7.2 Damage Detection Using SVD

In this dissertation, SVD and PCA can be used interchangeably. However, I prefer to use the term "SVD" because I will use left singular vectors, right singular vectors, and singular values explicitly. In PCA, the principal components, corresponding to the right singular vectors in SVD, and eigenvalues, equivalent to the singular values in SVD, are explicitly shown, but further processing is necessary after PCA to obtain the equivalents of the left singular values in SVD.

2.7.2.1 **Data Organization**

As mentioned earlier, 50 ultrasonic signals (each an average of 500) are recorded at each test step. Each signal with the length of 2000 is organized as a row vector in the data matrix X. For damage detection, data from two consecutive test steps is used, so there are 100 ultrasonic signals corresponding to 100 rows in the data matrix X. In SVD, $X = USV^T$, where data matrix X has the dimension of 100x2000, the left singular vector matrix has the dimension of 100x100, the singular value matrix has the dimension of 100x100, and the right singular matrix has the dimension of 2000x100.

2.7.2.2 **Feature Extraction from SVD**

In this section, I will discuss how the feature used for damage detection is extracted from SVD using statistical hypothesis testing. The results from SVD for a typical test step are shown in Figure 2-20. In Figure 2-20, a left singular vector and a right singular vector are plotted with red colors, and the specific meanings of this left singular vector and this right singular vector will be explained in the next section.

The right singular vectors are the basis vectors of the decomposition of ultrasonic signals using SVD, similar to the sinusoidal basis functions for the Fourier transform. Therefore, the right singular vectors have the same signal length as the recorded ultrasonic signals, and the time scale of the right singular vectors also depends on the sampling rate, which is 20 GHz in our experiment, like the recorded ultrasonic signals. Here, I refer to this time scale as fast time (Liu et al. 2015).

A left singular vector represents the relative weights of the corresponding right singular in the recorded ultrasonic signals. For example, the 1^{st} left singular vector represents the relative weights of the 1^{st} right singular vector in the decompositions of the 100 recorded ultrasonic signals. The 2^{nd} left singular vector represents the relative weights of the 2^{nd} right singular vector in the decompositions of the 100 recorded ultrasonic signals. Therefore, the length of left singular vectors is the same as the number of recorded ultrasonic signals in SVD, and this time scale depends on the time difference between ultrasonic signals, which is 15 seconds in our experiment. Here, I refer to this time scale as slow time (Liu et al. 2015).

The left singular vectors represent the relative weights because both the left singular vectors and the right singular vectors are normalized to have a vector length of 1. The weight magnitude information is stored in the singular values. Therefore, the left singular vectors multiplied by corresponding singular values will be absolute weights.

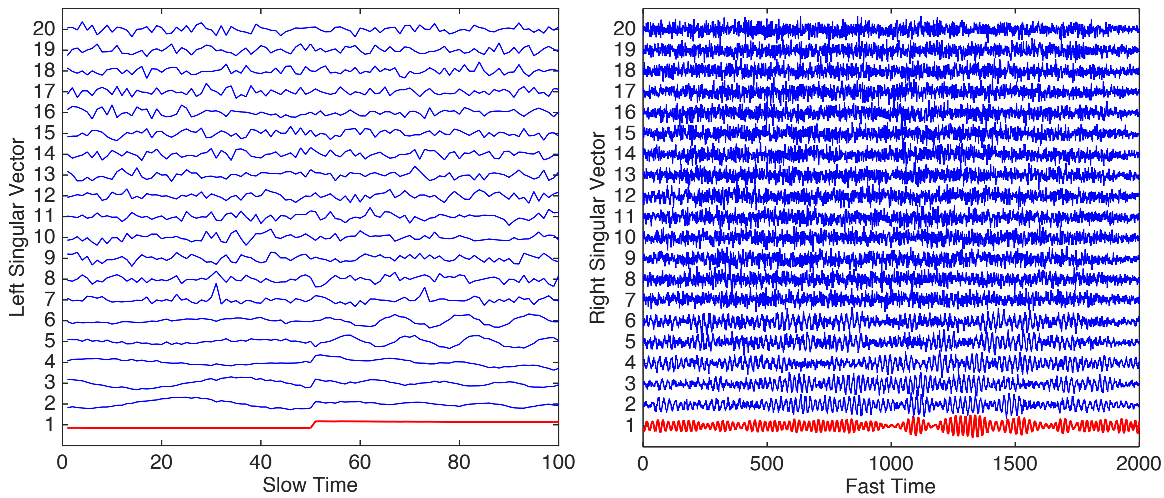

Figure 2-20 The first 20 left singular vectors and right singular vectors from a typical test step

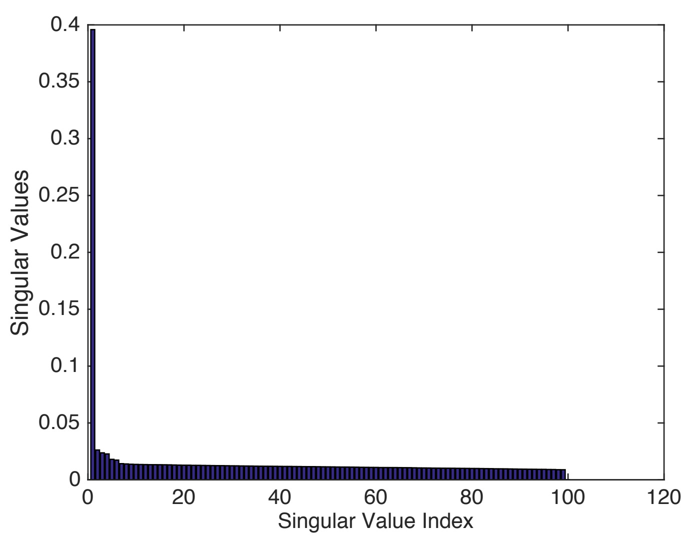

Figure 2-21 Singular values from a typical test step

In this organization of experimental data, if there exists volume loss in a test step, there should be a left singular vector showing the pattern like a step function, as shown by the red colored left singular vector in Figure 2-20(a). The red colored right singular vector in Figure 2-20(b) is the right singular vector corresponding to the left one with red color. The "step" in the left singular vector should be exactly at the middle of the left singular vector in this data organization method. To find the step function corresponding to the volume loss, a statistical hypothesis testing technique is used.

In this statistical hypothesis test, I suppose that a left singular vector $u_i = [u_i^1, \dots, u_i^{\frac{N}{2}}, u_i^{\frac{N}{2}+1}, \dots u_i^N]^T$ consists of two independent random samples $u_i^1, \dots, u_i^{\frac{N}{2}}$ and $u_i^{\frac{N}{2}+1}, \dots, u_i^N$ corresponding to the ultrasonic signals recorded in the baseline step and the damage detection step, respectively. Here I denote μ_X and μ_Y as the means of the first sample and second sample respectively. The null hypothesis and alternative hypothesis are:

$$H_0 : \ \mu_X = \mu_Y$$

$$H_1 : \ \mu_X \neq \mu_Y$$

Then $P_i(\mu_X = \mu_Y)$, the probability that μ_X is equal to μ_Y for the ith singular vector, shows the probability that the first sample and the second sample of a left singular vector are from the same distribution. The hypothesis test is run through the first 20 left singular vectors at each test step to identify the left singular vector most likely caused by the damage effects. (I use the logarithm of the minimum probability log $(min_i P_i(\mu_X = \mu_Y))$ of each test step as the feature to predict if there is volume loss of the thick-wall aluminum tube.) Figure 2-22 shows the hypothesis test result for one of the steps with damage. In this figure,

$P_1(\mu_X = \mu_Y)$ is the minimum value among all $P_i(\mu_X = \mu_Y)$ for this test step, and therefore $\log(P_1(\mu_X = \mu_Y))$ is used as the predictor variable for this test step. If $min_i P_i(\mu_X = \mu_Y)$ is used as the predictor variable, it will have similar performance in damage detection as the predictor variable $\log(min_i P_i(\mu_X = \mu_Y))$. However, the predictor variable $min_i P_i(\mu_X = \mu_Y)$ is heavily skewed towards the right hand side, so it might cause the damage detection algorithm to be less robust. Therefore, logarithm operator $\log(\cdot)$ is used here to correct the heavily skewed predictor variable distribution.

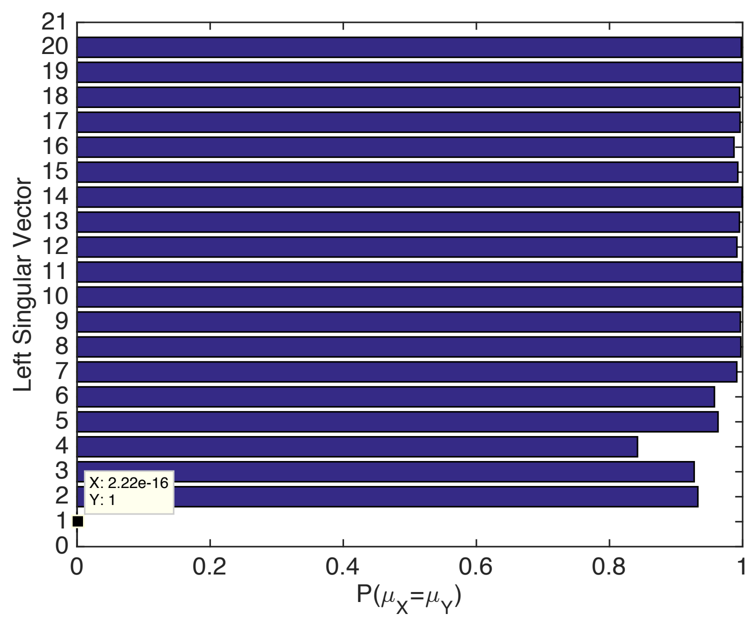

Figure 2-22 The probability that the first half samples (corresponding to the baseline signals) and the second half samples (corresponding to the new signals) in a left singular vector are from the same distribution

2.7.2.3 **Results and Discussions**

In this section, the feature extracted from SVD is used as the predictor variable and a logistic regression model is used as the classifier. The measured data and the best fit of the logistic regression model are shown in Figure 2-23. The circles are those steps without volume loss and the crosses are those steps with volume loss. The dotted line is the best fit from the logistic regression model using all the data as training set. In this figure, the data from different classes can be reasonably separated when using the feature extracted from SVD.

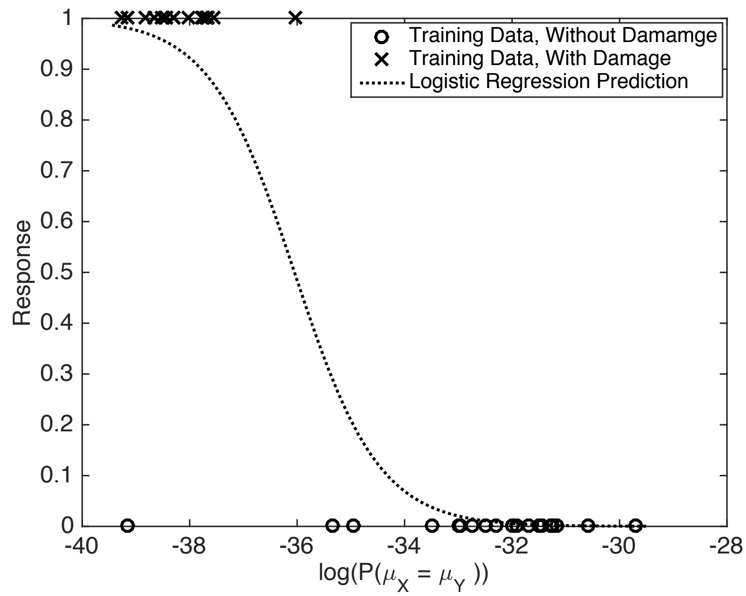

Figure 2-23 Damage detection using the logistic regression model and using the feature from SVD as the predictor variable

The performance of the logistic regression model using the feature from SVD as the predictor variable is shown in Figure 2-24 at different threshold levels, and the calculation of this performance uses leave-one-out cross validation. At each threshold level, the percentage of true positive (TP), true negative (TN), false positive (FP), and false negative (FN) predictions are shown separated in Figure 2-24. The black line is the F_1 score at each threshold level to shown the overall performance of the prediction model. In Figure 2-24, the highest F1 score and the accuracy are 0.94 and 0.95 respectively.

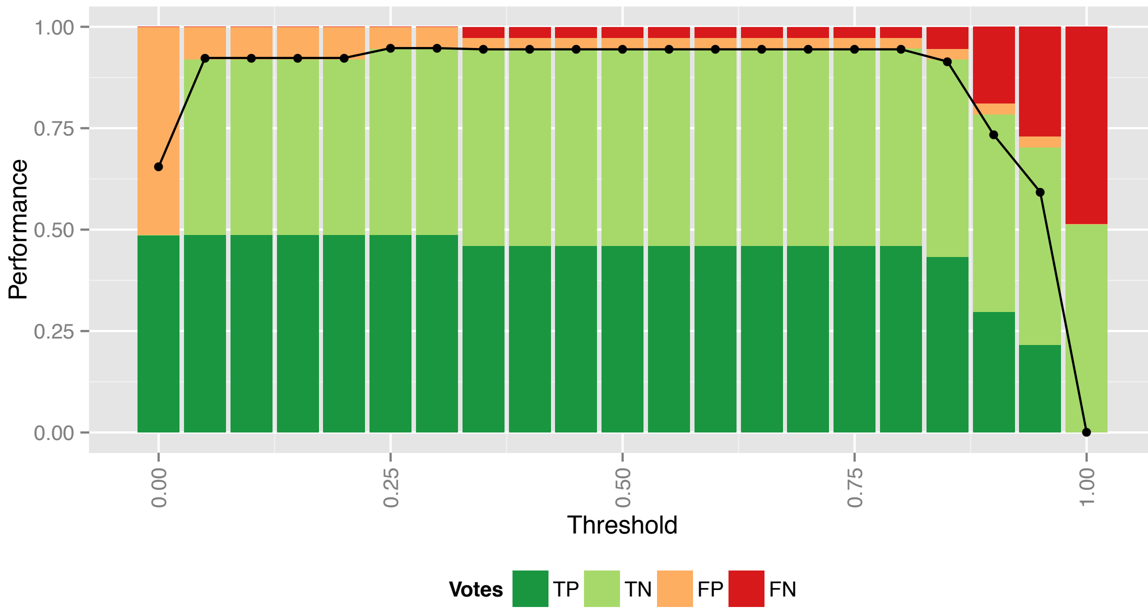

Figure 2-24 Performance of the logistic regression model using the feature from SVD as the predictor variable at different threshold values. The black line is the F_1 score at each threshold level.

2.8 Comparison of the Three Different Methods

To compare the performance of the three different methods for detection of volume loss in the thick-wall aluminum tube, maximum F1 score, maximum accuracy and area under a ROC curve (AUC) are listed in Table 2-2 and the ROC curves are plotted in Figure 2-25. From these three measures, the SVD method and the modified OSS method have comparable performance although the SVD method is slightly better than the modified OSS method in terms of AUC. A higher AUC means the method is more robust in damage detection. Both the SVD method and the modified OSS method have much better performance than the OSS method in this experiment.

Table 2-2 Comparison of the performance of the three different methods

	OSS	Modified OSS	OSS+SVD
F_1 score	0.78	0.94	0.94
Accuracy	0.82	0.95	0.95
AUC	0.79	0.92	0.96

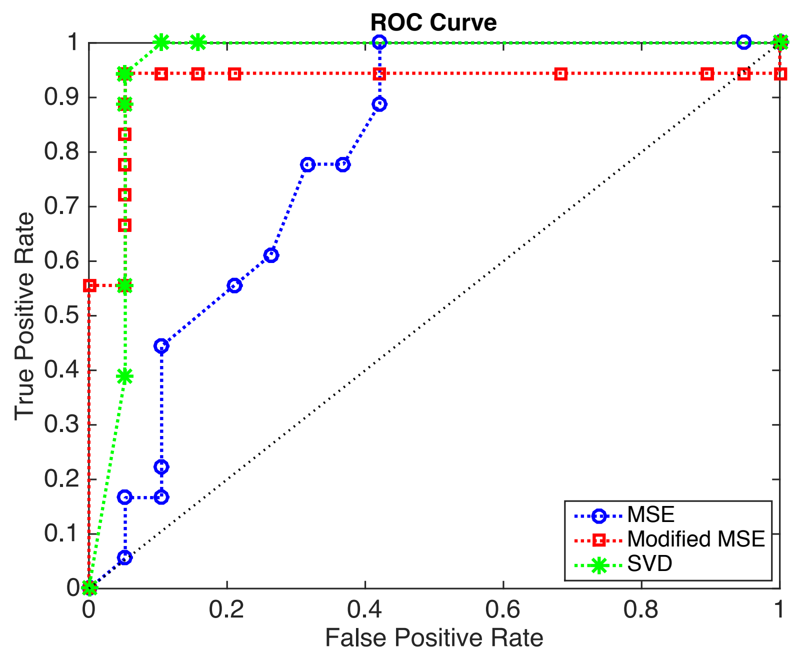

Figure 2-25 The ROC curves

These results indicate that the OSS method alone is not good enough to give reliable temperature compensation when the temperature change is in the range of about ±8 °C, while the modified OSS method and the SVD method can achieve much better results in the same range of temperature change. However, the SVD method can perform well in a larger threshold range than the modified OSS method as shown in Figure 2-19 and Figure 2-24 and in Table 2-2, so the SVD method is more robust in terms of threshold selection.

2.9 Conclusion

In this chapter, the modified OSS method and the SVD method are proposed to detect volume loss in a thick-wall aluminum tube specimen under temperature variations, and the performance of these methods is compared with the regular OSS method. The regular OSS method did not perform well in my experiment because of the relative large temperature variations in the range of about ±8 °C. However, the modified OSS method and the SVD method performed much better than the regular OSS method, as measured by F_1 score, accuracy, and ROC. The SVD method can perform better than the regular OSS method because of its ability to separate the temperature effects from the damage effects. The modified OSS method can further remove the pattern between the stretching factor and the damage indicator, (MSE in this instance) so it can perform much better than the regular OSS method.

Chapter 3 Orthogonal Relationship between Temperature-Induced and Damage-Induced Ultrasonic Change Signals

3.1 Introduction

In the earlier research work in our group, the SVD technique performed well for pipeline damage detection (Liu et al. 2015) and localization (Liu et al. 2015) with temperature variations. In those studies, the SVD technique was demonstrated to be able to somewhat separate the damage-induced ultrasonic change signals from ultrasonic baseline signals and from ultrasonic change signals caused by other factors. Therefore, the temperature effects and other effects could be removed by selecting a left singular vector and a right singular vector corresponding to damage using techniques such as statistical hypothesis testing. In SVD, left singular vectors are unit vectors that are orthogonal to each other as are the right singular vectors. Therefore, damage-induced change signals were inherently assumed to be orthogonal to change signals caused by other factors, e.g. temperature-induced change signals, in the SVD technique studied in (Liu et al. 2015) and (Liu et al. 2015). However, the hypothesis of the orthogonal relationship between the damage-induced change signals and the temperature-induced change signals was not directly studied in their earlier work.

In my earlier work on the thick-walled aluminum tube experiments, I observed an interesting phenomenon that the vector length of the sum of temperature-induced and damage-induced change signals was always greater than the vector length of damage-induced change signals alone. If the orthogonal relationship between temperature-induced and damage-induced ultrasonic change signals exists, this phenomenon can then be explained because temperature-induced change signals will not cancel damage-induced change signals if they are orthogonal to each other.

Therefore, the motivation of the research work in this chapter is to study the hypothesis of the orthogonal relationship and then use it to explain the above phenomena observed in our earlier work. I will also explain how the relationship could be potentially used for damage detection and quantification under temperature variations or other environmental and operational conditions (EOCs).

This chapter is organized as following. The approximate orthogonal relationship between temperature-induced and damage-induced ultrasonic change signals will be studied and demonstrated in section 3.2. The potential underestimation in damage detection or quantification due to an approximate (but not exact) orthogonal relationship will be shown in section 3.3. The potential applications of the orthogonal relationship will be discussed in section 3.4. Finally, I will summarize the work in this chapter in section 3.5.

3.2 Orthogonal Relationship between Temperature-Induced and Damage-Induced Ultrasonic Change signals

In this chapter, I will use the data collected from the one-transducer mode in the experiment described in section 2.2 to study the hypothesis that temperature-induced and damage-induced ultrasonic change signals are orthogonal to each other. In that experiment, the temperature changes of the specimen are not directly measured. Instead, the temperature changes are characterized by stretching factors as discussed in section 2.4.

3.2.1 Data Organization

To study the relationship between ultrasonic baseline signals, temperature-induced change signals, and damage-induced change signals, I need to first extract the two types of change signals from the raw ultrasonic signals collected from the experiment. The raw ultrasonic signals can be treated as a superimposition of ultrasonic baselines, temperature-induced change signals, and damage-induced change signals. The method to extract the two types of change signals is to find triplets, where a triplet is defined as an ultrasonic baseline signal (s_b), an ultrasonic signal affected only by a temperature change (s_t), and an ultrasonic signal affected only by a damage change (s_d) as shown in Figure 3-1. In this figure, all signals are represented as two-dimensional vectors although the real dimension should be the length of signals. Temperature-induced change signals (Δs_t) and damage-induced change signals (Δs_d) can then be extracted by subtracting the baselines.

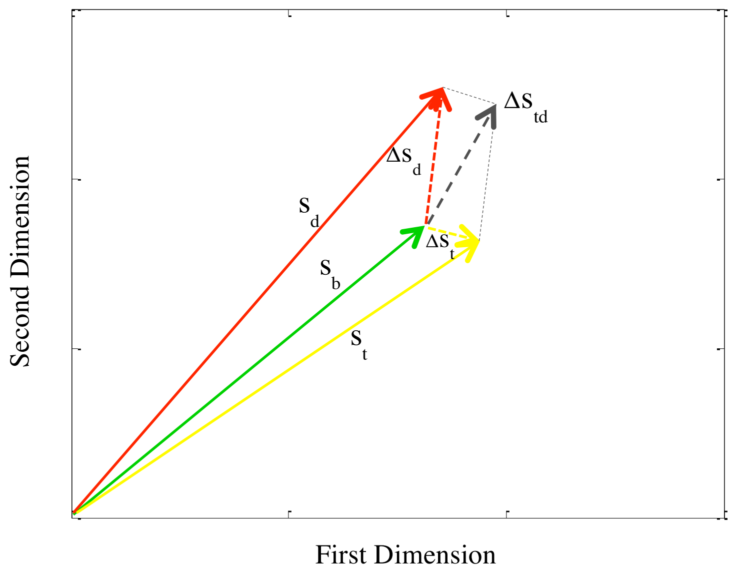

Figure 3-1 A triplet defined as an ultrasonic baseline signal (s_b), an ultrasonic signal affected only by a temperature change (s_t), and an ultrasonic signal affected only by a damage change (s_d)

A random combination of three different signals from the 1850 raw ultrasonic signals may form a triplet but not necessarily; this is because when one signal is used as the baseline there might be both temperature effects and damage effects in the other two signals. The total number of potential triplets from the 1850 ultrasonic signals is on the order of 10^9, and it would take me a few months to examine all the possible triplets. For practical purposes, I use random sampling to find 10,000 qualified triplets for the analysis. In the random sampling, it is impossible to find two different ultrasonic signals with the exact same temperature, so when I claim that two signals share the same temperature or when I claim an ultrasonic signal is affected only by damage in the experiment, it means that the temperature difference between the two measurements is small enough that the stretching factor between the two signals is within the range of $1 \pm 2*10^{-5}$.

3.2.2 Resolution of Stretching Factors

The threshold of $2*10^{-5}$ is the resolution achievable in stretching analysis considering the factors of stretching algorithm, instrument errors, and white noise. The stretching algorithm itself can achieve a resolution on the order of 10^{-6} in a simulation (Harley and Moura 2012). However, there are instrument errors in real signals, such as the errors caused by the function generator and digitizer across different signals, and there exists white noise in signals collected in the experiment. Both instrument errors and while noise will decrease the resolution of stretching factor achievable in analysis.

A simple experiment was designed in order to determine the overall effects of stretching algorithm, instrument errors, and white noise. This experiment was carried out on the same specimen with the same transducer and experimental setups as in the experiment in section 2.2. In this experiment, 1000 ultrasonic signals were recorded with a time interval of 12 seconds between signals, which is the minimum interval attainable with our data acquisition system. Then the $i+1^{th}$ signal was stretched against the i^{th} signal to calculate the stretching factor using only the part of signal between 32 and 48 μs corresponding to the first two pulse echoes. Because no damage was introduced between signals and because I assume there were no significant temperature changes within the 12 seconds, deviations of stretching factor from 1 were considered errors caused by the stretching algorithm, instrument errors, and white noise.

The histogram of stretching factors from this analysis is shown in Figure 3-2. From this figure, the maximum deviation from 1 is $2*10^{-5}$ among the 999 stretching factors, and therefore $2*10^{-5}$ is used as the resolution of our stretching analysis considering stretching algorithm, instrument errors, and white noise. This resolution of stretching factors is conservative when using the maximum deviation as the estimate, especially considering that the temperature can have some minor changes within the 12 seconds and this temperature effects are also included in the maximum deviation.

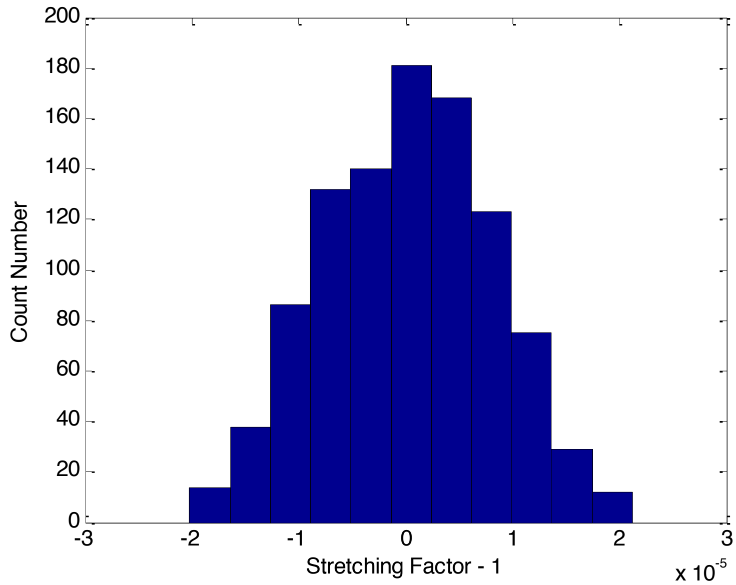

Figure 3-2 The histogram of stretching factors

3.2.3 Results and Analysis

From the 10,000 sampled triplets, temperature-induced change signals (Δs_t) and damage-induced change signals (Δs_d) were extracted as described earlier, and their angles and correlation coefficients with the baseline signals were plotted in Figure 3-3 and Figure 3-4 respectively. Here angles are defined as $\theta = \cos^{-1}\frac{u \cdot v}{\|u\|_2 \|v\|_2}$, where u and v are two vectors and $\|\cdot\|_2$ is the Euclidean norm of a vector.

The angles and correlation coefficients have an approximate bilinear relationship in Figure 3-3. This is because temperature changes cause velocity changes of ultrasonic signals, and signals with temperature changes are proportionally delayed or advanced against the baseline signals. The variations, when there is no temperature change or the change is very small, are relatively large because of the small vector lengths of the temperature-induced change signals in the denominator.

The angles and correlation coefficients have no clear pattern in Figure 3-4. The volume loss in the aluminum tube broadly scatters ultrasonic signals. Furthermore, scattered ultrasonic waves propagate along multiple complicated paths before they arrive at the transducer. Therefore, damage-induced ultrasonic change signals do not have a clear pattern like that caused by temperature changes, and the angles and correlation coefficients then have no clear pattern in Figure 3-4.

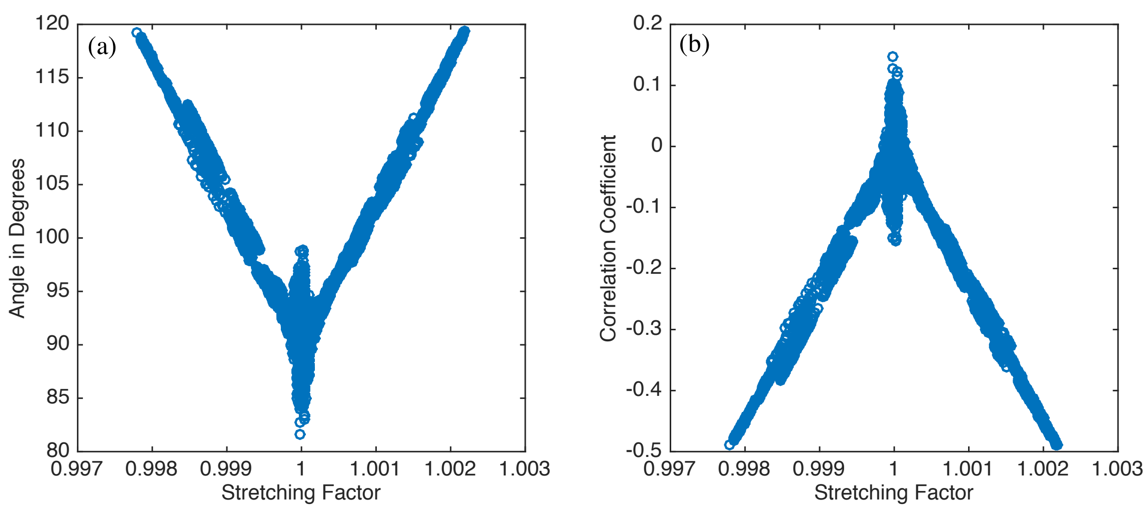

Figure 3-3 Relationship between temperature-induced change signals and baseline signals: (a) correlation coefficients; (b) angles in degrees

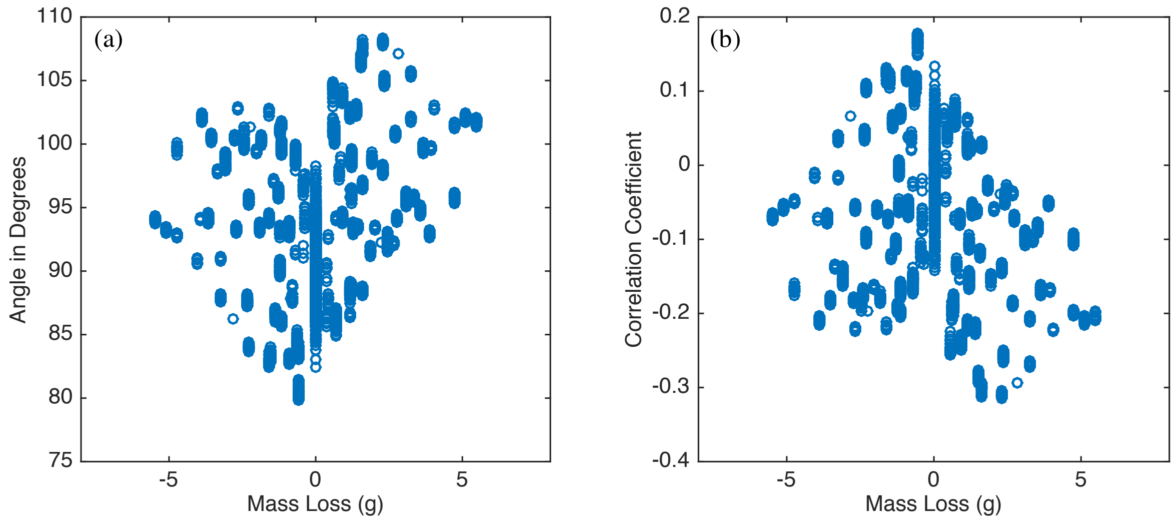

Figure 3-4 Relationship between damage-induced change signals and baseline signals: (a) angles in degrees; (b) correlation coefficients

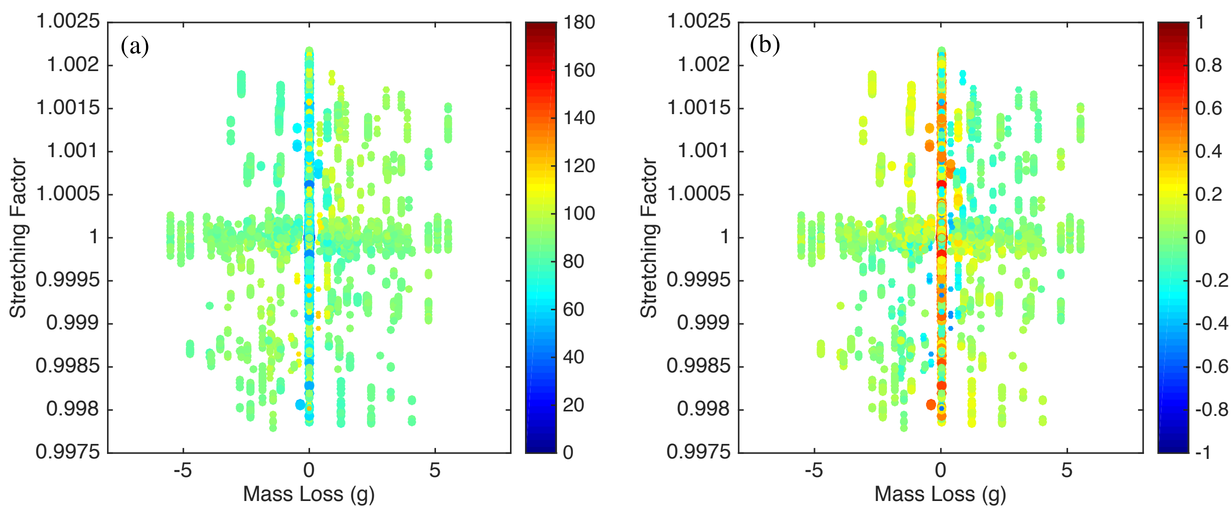

Figure 3-5 Relationship between temperature-induced and damage-induced ultrasonic change signals when the stretching threshold is $2*10^{-5}$: (a) angles in degrees; (b) correlation coefficients

Figure 3-5 is a plot of angles and correlation coefficients between temperature-induced and damage-induced ultrasonic change signals. The color represents the angles in Figure 3-5(a) and correlation coefficients in Figure 3-5(b). Figure 3-6 is a plot of Figure 3-5 with the temperature changes dropped, and Figure 3-7 is a plot of Figure 3-5 with the mass loss dropped. In these three figures, the threshold to define if two signals share the same temperature is $2*10^{-5}$ as discussed in section 3.2.2.

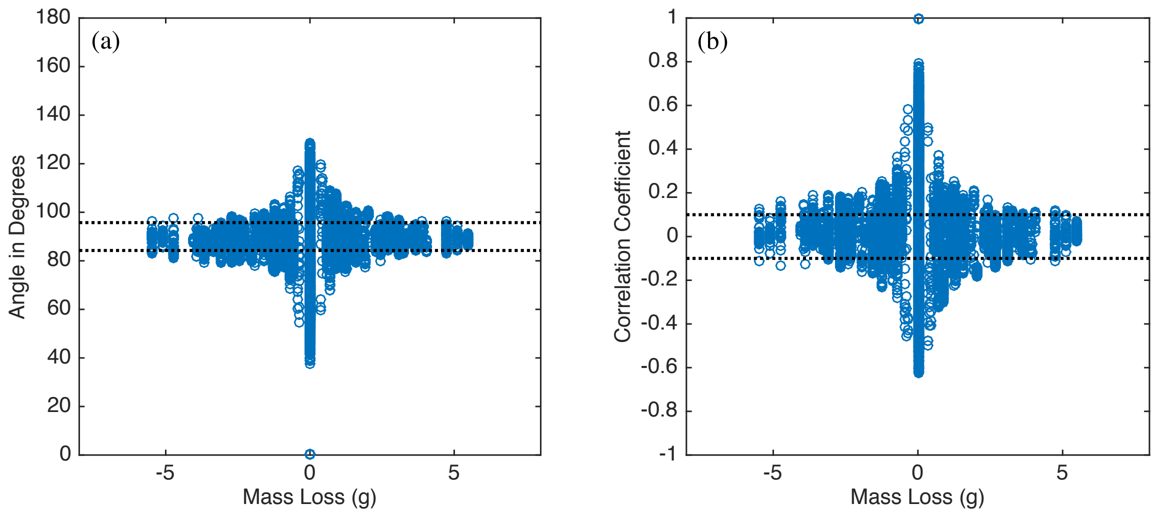

Figure 3-6 Relationship between temperature-induced and damage-induced ultrasonic change signals with the temperature changes dropped when the stretching threshold is $2*10^{-5}$: (a) angles in degrees; (b) correlation coefficients

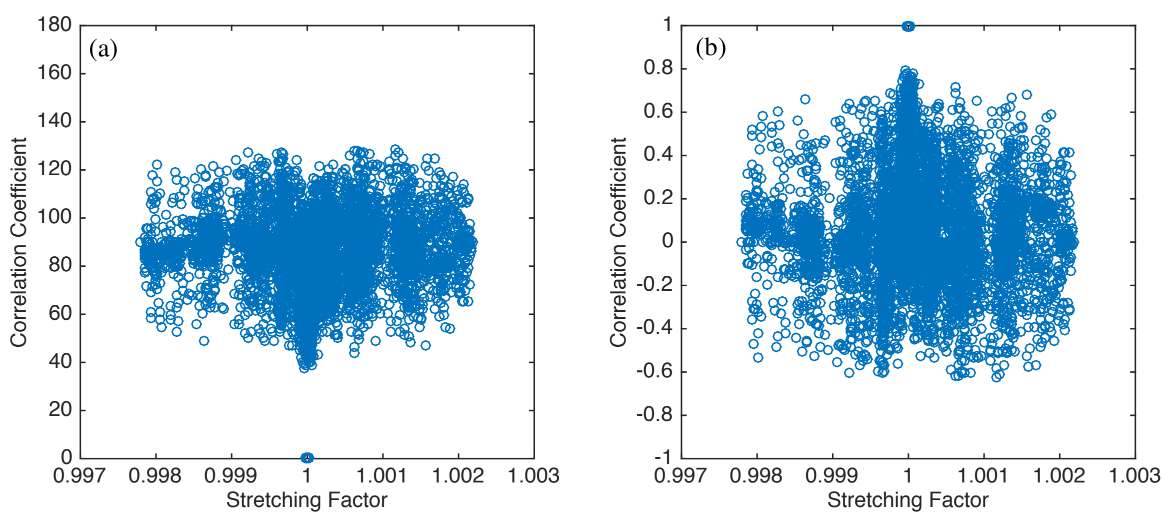

Figure 3-7 Relationship between temperature-induced and damage-induced ultrasonic change signals with the mass loss dropped: (a) angles in degrees; (b) correlation coefficients

In Figure 3-6, the angle varies around 90 degrees and the correlation coefficient varies around 0; both variations decrease with damage level, and tend to stabilize at a certain low level. This is because that the claimed damage-induced change signals contain some temperature-induced changes. When a claimed damage-induced change signal is extracted, the two ultrasonic signals used should share the same temperature but should have different mass loss. In reality, the same temperature is not achievable, and instead two ultrasonic signals recorded at temperatures close enough (the stretching factor between these two signals is less than a stretching threshold like $2*10^{-5}$ mentioned earlier in section 3.2.2) are used to extract the damage-induced change signal.

If mass loss is relatively small, temperature-induced change signals in claimed damage-induced change signals will significantly influence angles or correlation coefficients between temperature-induced and claimed damage-induced ultrasonic change signals. However, if mass loss is large, temperature-induced changes in damage-induced change signals will have negligible influence on angles or correlation coefficients. This can be further verified by relaxing the threshold. If the stretching threshold is relaxed to $8*10^{-5}$, the variations in Figure 3-8 and Figure 3-9 become much larger because the temperature-induced changes become greater in the claimed damage-induced change signals. The dotted horizontal lines represent the noise levels caused by instrument errors and white noise. The noise levels are calculated by replacing the damage-induced ultrasonic change signals with noise signals extracted from the experiment described in section 3.2.2.

The variations of angles and correlation coefficients both stabilize at the noise levels. Therefore, if variations caused by temperature components in damage-induced change signals, instrument errors and white noises are excluded, the angles tend to approximate 90 degrees and the correlation coefficients tend to approximate 0, meaning that temperature-induced and damage-induced ultrasonic change signals are approximately orthogonal to each other. The orthogonal relationship between temperature-induced and damage-induced ultrasonic change signals mainly originates from "randomness" in the damage-induced change signals. The "randomness" here means that scattered ultrasonic pulses do not have a clear pattern and are somewhat randomly scattered in ultrasonic signals.

The angles and the correlation coefficients have no clear pattern in Figure 3-7. This also verifies the conclusion that the orthogonal relationship between temperature-induced and damage-induced change signals mainly originates from "randomness" in the damage-induced ultrasonic change signals, which is not present in the temperature-induced change signals.

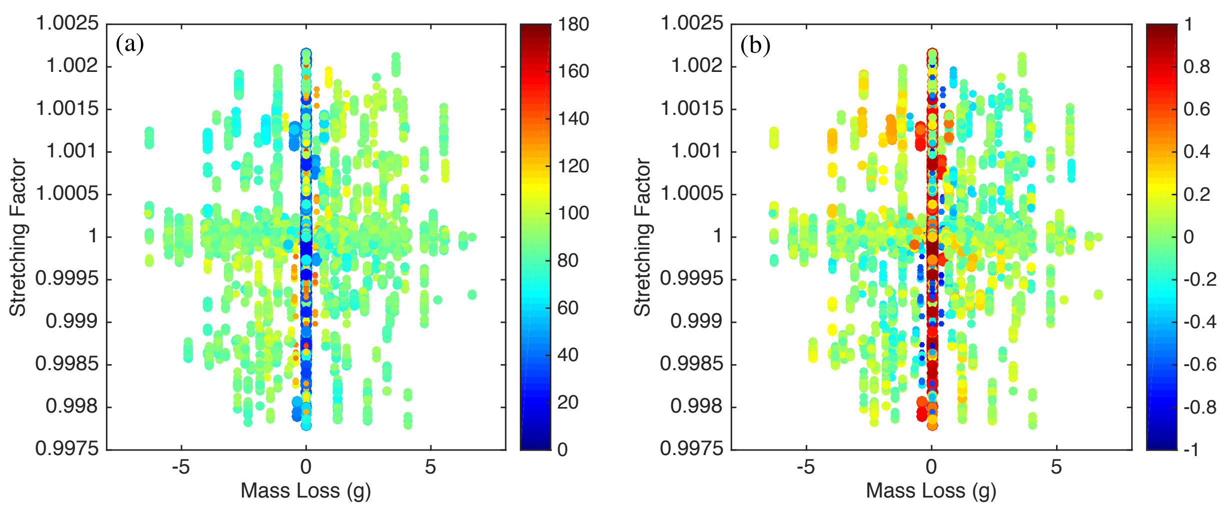

Figure 3-8 Relationship between temperature-induced and damage-induced change signals when the stretching threshold is $8*10^{-5}$: (a) angles in degrees; (b) correlation coefficients

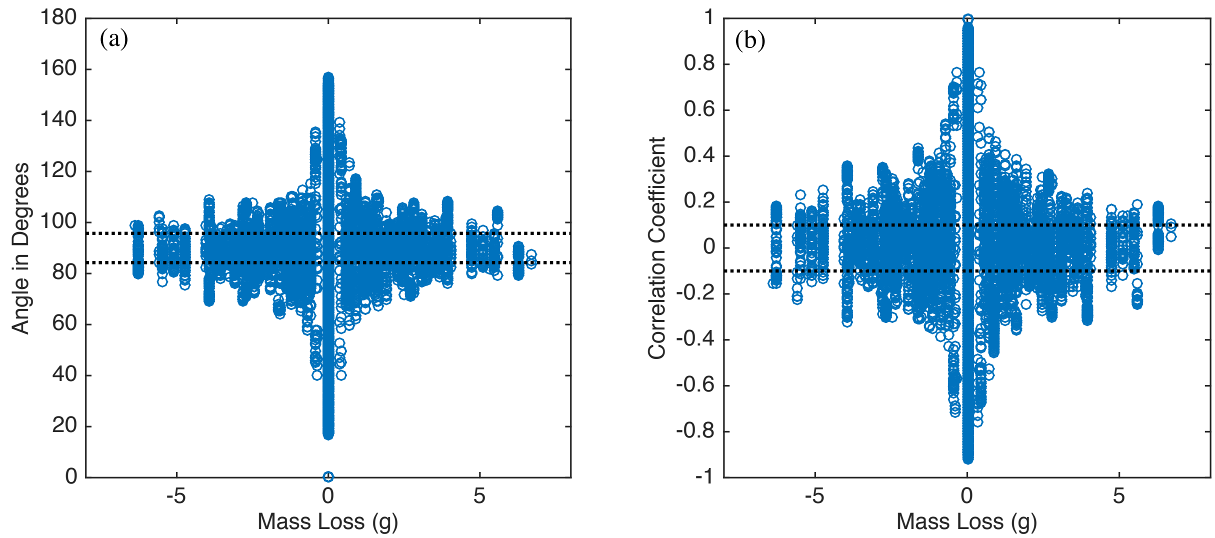

Figure 3-9 Relationship between temperature-induced and damage-induced ultrasonic change signals with the temperature changes dropped when the stretching threshold is $8*10^{-5}$: (a) angles in degrees; (b) correlation coefficients

3.3 Underestimation in Damage Detection or Quantification

If the orthogonal relationship between temperature-induced ultrasonic change signals (Δs_t) and damage-induced ultrasonic change signals (Δs_d) is strictly satisfied, then the vector length $\| \Delta s_t + \Delta s_d \|_2$ will always be greater than or equal to the vector length $\| \Delta s_d \|_2$. In other words, the damage can never be underestimated when using the MSE method without temperature compensation, and $\| \Delta s_t + \Delta s_d \|_2$ will be equal to $\| \Delta s_d \|_2$ if and only if new signals are measured at the baseline temperature level.

However, the orthogonal relationship is not exact, and instrument errors and white noise also exist in the recorded ultrasonic signals. Therefore, it is possible that $\| \Delta s_t + \Delta s_d \|_2$ will be less than $\| \Delta s_d \|_2$ in some circumstances. It is important to know how much $\| \Delta s_t + \Delta s_d \|_2$ can be less than $\| \Delta s_d \|_2$, which can also reveal to what extent the orthogonal relationship is satisfied. Data used for this analysis is the same as that used in section 3.2. The ratios of mixed effects $\| \Delta s_t + \Delta s_d \|_2$ to damage effects $\| \Delta s_d \|_2$ are shown in Figure 3-10(a) for all the data and in Figure 3-10(b) for the data for which $\| \Delta s_t + \Delta s_d \|_2$ are less than the damage effects $\| \Delta s_d \|_2$. From Figure 3-10, most ratios are greater than 1. Only about 13.2% of the ratios are less than 1, and these ratios less than 1 show up only when the stretching factors are very close to 1. Even when the ratios are less than 1 they are not far from 1 because of no significant temperature changes in these cases. After the stretching factors are dropped from Figure 3-10(b), the ratios are plotted against the mass loss as shown in Figure 3-11. From Figure 3-11, the ratios are not significantly smaller than 1 unless there is no mass loss or the mass loss is very small.

Overall, $\| \Delta s_t + \Delta s_d \|_2$ can not be meaningfully less than $\| \Delta s_d \|_2$ as a percentage unless both temperature changes and mass loss are small. When both temperature changes and mass loss are small, absolute values of $\| \Delta s_t + \Delta s_d \|_2$ and $\| \Delta s_d \|_2$ will be quite small. Therefore, the use of $\| \Delta s_t + \Delta s_d \|_2$ for damage detection or quantification would not cause significant underestimation, no matter the temperature ranges and the damage ranges.

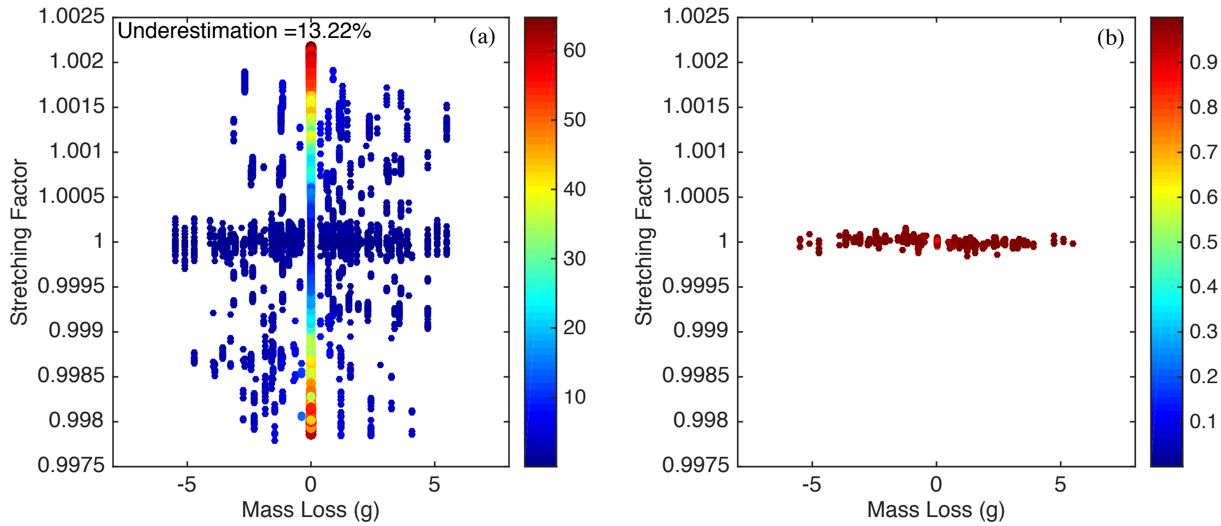

Figure 3-10 The ratios of mixed effects $\| \Delta s_t + \Delta s_d \|_2$ to damage effects $\| \Delta s_d \|_2$ (a) for all the data; (b) for the data for which mixed effects $\| \Delta s_t + \Delta s_d \|_2$ are less than the damage effects $\| \Delta s_d \|_2$

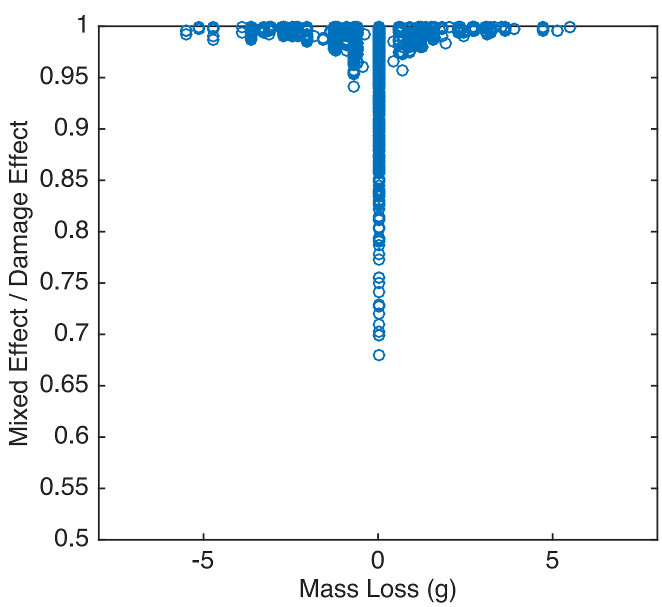

Figure 3-11 The ratios of mixed effects $\| \Delta s_t + \Delta s_d \|_2$ to damage effects $\| \Delta s_d \|_2$ for the data for which mixed effects $\| \Delta s_t + \Delta s_d \|_2$ are less than the damage effects $\| \Delta s_d \|_2$ (stretching factors are not shown in this figure)

3.4 Applications and Discussions

3.4.1 Application in SVD Damage Detection and Localization

As mentioned at the beginning of this chapter, the SVD technique performed well for pipeline damage detection (Liu et al. 2015) and localization (Liu et al. 2015) with temperature variations in earlier research work in our group, but why the SVD technique performed well was not directly investigated. Now, the orthogonal relationship between temperature-induced and damage-induced ultrasonic change signals studied in section 3.2 gives a direct explanation why the SVD technique can separate temperature effects from damage effects and can perform well for damage detection and localization.

3.4.2 Application in MSE Damage Detection or Quantification

In my earlier work on the thick-walled aluminum tube experiments, I observed an interesting phenomenon that the vector length of the sum of temperature-induced and damage-induced change signals was always greater than the vector length of damage-induced change signals alone. To be specific, Figure 3-12 shows the results from the MSE method for volume loss quantification. The data is from the experiment described in section 2.2. In the experiment, 50 signals are recorded at each test step, but only the first signal in each test step is used here. For the OSS temperature compensation, the signal from the first step is used as the baseline and all signals are stretched against the baseline. The stretching factors are shown in Figure 3-12(a), and the stretching factors fluctuate around 1 or the temperature fluctuates around the baseline temperature level. In the MSE method, the signal from the first step is used as the baseline to calculate the residuals for all other signals after the OSS temperature compensation. MSEs are then calculated from the residuals and shown as red color circles in Figure 3-12(b). The results from the MSE method without temperature compensation are shown as blue color circles in Figure 3-12(b).

In Figure 3-12(b), the MSE with OSS temperature compensation is the lower bound of the MSE without temperature compensation. The stretching factor crosses the baseline level multiple times as shown in Figure 3-12(a), but the blue curve is always above the red curve. The orthogonal relationship studied in section 3.2 can explain this phenomenon. The temperature-induced change signals can never cancel the damage-induced change signals if they are orthogonal to each other. Therefore, MSE without temperature compensation must be greater than the one with temperature compensation no matter the temperature is above or below the baseline level.

It can also be concluded from Figure 3-12 that temperature compensation techniques are not necessary for damage detection and quantification in long-term structural health monitoring projects, as long as the temperature fluctuates around the baseline level and must cross the baseline level at least once per specified time period. The specified time period is the time resolution of the monitoring project. Some types of deterioration, like corrosion, erosion, and fatigue cracking, take decades to develop in infrastructure systems. Therefore, the time resolution of the monitoring project for these infrastructure systems are usually not very high, so the above requirement can be satisfied most of time. Even if not satisfied, the requirement can also be relaxed by using multiple baselines. With multiple baselines, the temperature only need to cross one of the baseline levels once per specified time period.

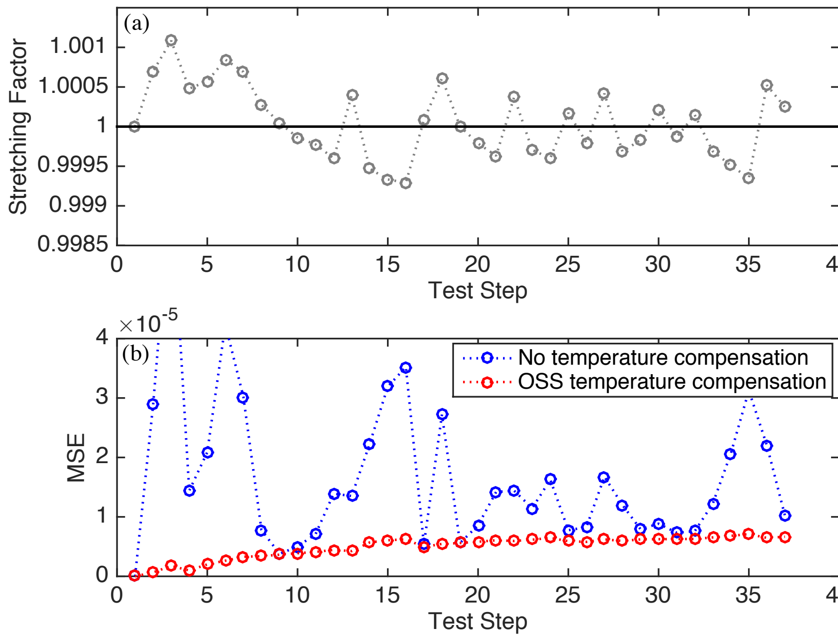

Figure 3-12 Quantification of volume loss in a thick-walled aluminum tube: (a) stretching factors; (b) results using MSE with or without the OSS temperature compensation

3.5 Conclusion

In this chapter, I studied the relationship between temperature-induced and damage-induced ultrasonic change signals and conclude that they are approximately orthogonal to each other. The orthogonal relationship between temperature-induced and damage-induced ultrasonic change signals mainly originates from “randomness” in the damage-induced change signals. The “randomness” here means that scattered ultrasonic pulses do not have a clear pattern and are somewhat broadly scattered in ultrasonic signals.

This orthogonal relationship explains why the SVD technique can separate damage effects from other effects, and function effectively for damage detection and localization in the earlier work in our group. Using this orthogonal relationship, temperature compensation becomes unneccesary in principle for damage detection and quantification in long-term structural health monitoring projects under certain conditions. One advantage of this strategy is that it does not add significant system resources to store baselines (like in the optimal baseline selection method) or to stretch ultrasonic signal (like in the optimal signal stretching method) for structural health monitoring. Another potential advantage of this strategy over the optimal signal stretching method is that it is not strictly limited by the range of temperature changes.

Chapter 4 Ultrasonic Time-of-Flight Diffraction for Thickness Loss Quantification

4.1 Introduction

It is often difficult to develop good physical models for structural health monitoring (SHM) of infrastructure systems. However, if a good physical model is available for a specific structure, in the author's opinion the model-based method is preferable instead of data-driven methods because model-based methods are straightforward and easy to interpret. Furthermore, it might not be necessary to calibrate the model parameters in model-based methods, or at least it is relatively easier to carry out calibration experiments on real infrastructure systems because the calibration usually only involves the determination of some key parameters about the mechanical properties of materials and structural geometrical dimensions.

In this chapter, our goal is to detect and quantify thickness loss of thick-walled aluminum tubes. The pulse-echo method is one of the most commonly used ultrasonic techniques for plate and pipe thickness measurement. However, the pulse-echo method did not perform well to quantify the thickness loss of frac iron components retired from in-service applications due to erosion damage. Figure 4-1 shows a typical frac iron elbow with erosion damage and the two pulse-echo measurement locations. Figure 4-2(a) shows the ultrasonic pulse-echo measurements at the location without erosion damage and Figure 4-2(b) shows another measurement at the location with erosion damage on the frac iron elbow. The thickness loss at the erosion spot is approximately 50% of the 22 mm wall thickness. The pulse-echo method did not perform well because the morphology of thickness loss was irregular and reflected ultrasonic pulses away from the transducer, making it difficult to detect an echo.

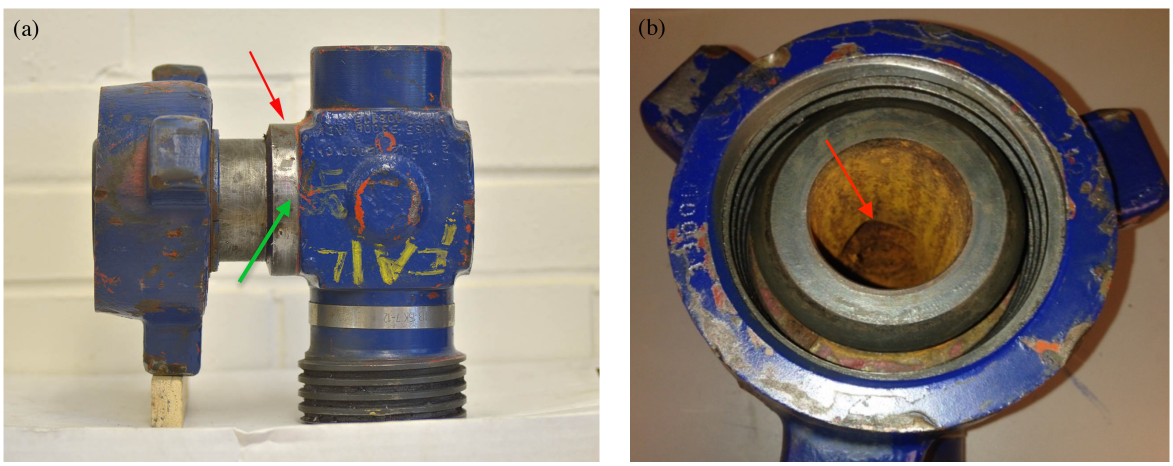

Figure 4-1 (a) A frac iron elbow retired from in-service applications due to erosion damage at location shown by the red arrow. The green arrow shows a location without erosion damage; (b) the same frac iron elbow from a different perspective of view to show the inside erosion damage by the red arrow

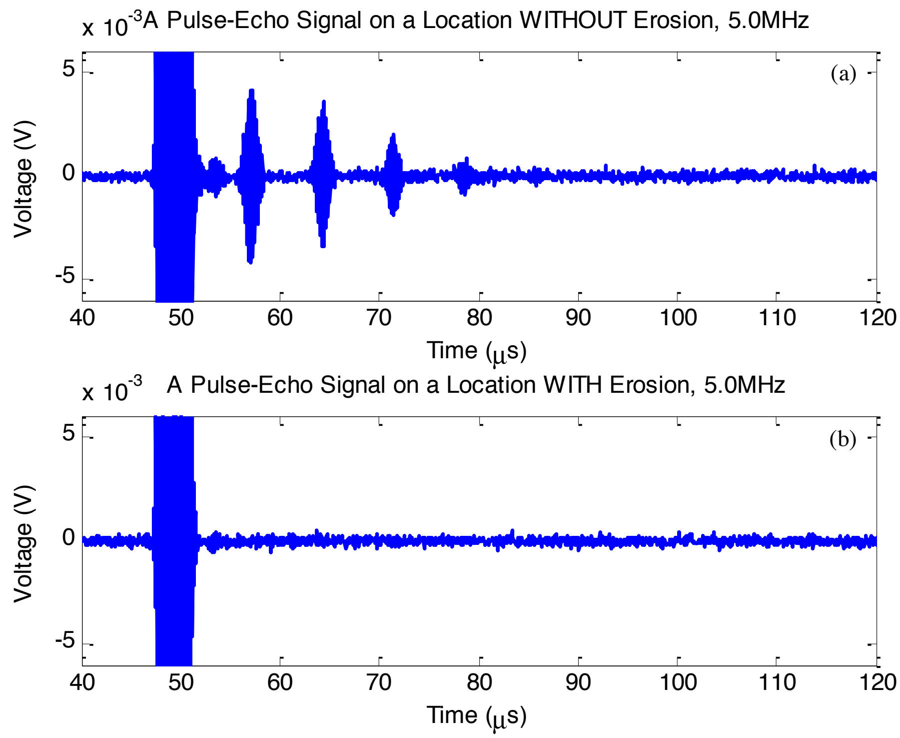

Figure 4-2 Pulse echo measurements on a location (a) without erosion damage as shown by the green arrow in Figure 4-1; (b) with erosion damage as shown by the red arrows in Figure 4-1

The time-of-flight diffraction technique was developed, by Silk and his co-workers at the National NDE center, starting in the early 1970s for detecting and sizing defects in the shell of the pressurized water reactor (PWR) pressure vessel. The origin and development of this technique were detailed in a series of publications by Silk and his co-workers on this topic (Silk 1979; Silk 1979; Silk 1982; Silk 1982; Silk 1984; Silk and Lidington 1975).

The time-of-flight diffraction technique grew out of the difficulties encountered in defect sizing using the conventional pulse-echo method. The pulse-echo method assumes a specular reflection formed by the damage surface. However, a reasonable specular reflection is very rare in field applications. If the specular assumption is not satisfied, the pulse-echo method might not be able to detect the defects or the size of defect might not be estimated accurately. Furthermore, when the pulse-echo method is applied in an application with randomly oriented defects, the scanning probe needs to be placed at different angles to find the specular reflection, and (many times), the sensitivity is still very low in these conditions. Scanning at different angles is not only inconvenient but also not available sometimes due to the constraints of the scanning surface in field applications (Charlesworth and Temple 2001).

After the invention of the time-of-flight diffraction technique, it has become more and more popular in the field of NDE and it has been applied to some very complicated structure types. For example, this technique was applied to detect cracks in T-butt welds and the results showed sizing accuracy on the T-butt welds was comparable to that on simple plate-like structures. In contrast, the accuracy from the pulse-echo method was insufficient for the same test conditions (Jessop and Mudge 1980). The time-of-flight diffraction was also used to study fatigue crack sizing on offshore structures, and in the experiment satisfactory defect sizing measurements were achieved in the underwater condition at laboratory facilities (Hawker et al. 1985; Newton et al. 1986). More examples about the applications of the time-of-flight diffraction technique can be found in (Charlesworth and Temple 2001).

This chapter is organized as follows. In section 4.2, the inductively coupling concept is discussed, and the experiment is then carried out in both wired setup and inductively coupled setup in section 4.3. The results of the ultrasonic time-of-flight diffraction for the thickness loss quantification of thick-walled aluminum tubes are presented in section 4.4. The research work in this chapter is then summarized in section 4.5.

4.2 Inductively Coupled Ultrasonic Transducers

Most ultrasonic techniques for SHM and NDE are implemented using wired ultrasonic transducers. The electrical connection between the ultrasonic transducer and the cable is a weak point in a wired transducer design. Corrosion of connectors might be a serious problem in some long-term monitoring projects, especially where exposed to weather and to contamination (Greve et al. 2007). In recent years, wireless transducer techniques have been introduced to overcome these difficulties. However, this approach typically requires the transducer to have a power supply, usually a battery (Lynch 2007). It also typically requires the transducer to have reliable data processing and transmitting modules. These additional requirements result in significant system complexities (Cho et al. 2008; Lynch 2007).

In earlier work at CMU, an inductively coupled transducer was developed, its electrical behavior was studied (Greve et al. 2007), and it was used to generate Lamb waves and longitudinal waves in plates by edge-mounted transducers for damage detection (Greve et al. 2007; Greve et al. 2008; Zheng et al. 2008). This technique has also been investigated and used to detect delamination damage in carbon fiber composite material by other authors (Zhong et al. 2013). The inductively coupled transducer is inherently a wireless design, but it greatly simplifies the data transmission and power supply mechanisms by using inductive coupling when compared with other wireless designs. Overall, the inductively coupled transducer has advantages of no exposed electrical wiring and longer lifetime compared to wired transducers, and it has advantages of low cost and system simplicity compared to other wireless transducers.

The inductively coupled transducer concept is shown in Figure 4-3. A piezoelectric transducer is wired to the coil #1 winding on a ferrite core, and the coil #2 winding on another ferrite core is connected to a pulser or a digitizer depending on whether the transducer is used as a transmitter or a receiver. When the coil #2 receives a pulse from a pulser, the electric pulse is inductively coupled to the piezoelectric transducer and consequently the piezoelectric transducer will emit ultrasonic waves into the structure. Similarly, when the transducer receives ultrasonic waves and transforms the waves into electric pulses, the electric pulses will be inductively coupled back into coil #2 and received by the digitizer.

I envision that the coil #1 can be encapsulated within the piezoelectric transducer. The transducer itself is then entirely passive and it can be mounted permanently onto the target structure. This transducer design should enable a long lifetime if the encapsulation is properly designed. I also envision that the pulser and receiver can be integrated into a handheld device, connected to a probe corresponding to coil #2, making it convenient to use this device to take pulse-echo measurements. If two probes are designed for the handheld device, with one probe connected to the pulser and the second probe connected to the digitizer, then the device can take pitch-catch measurements between two transducers mounted on the structure.

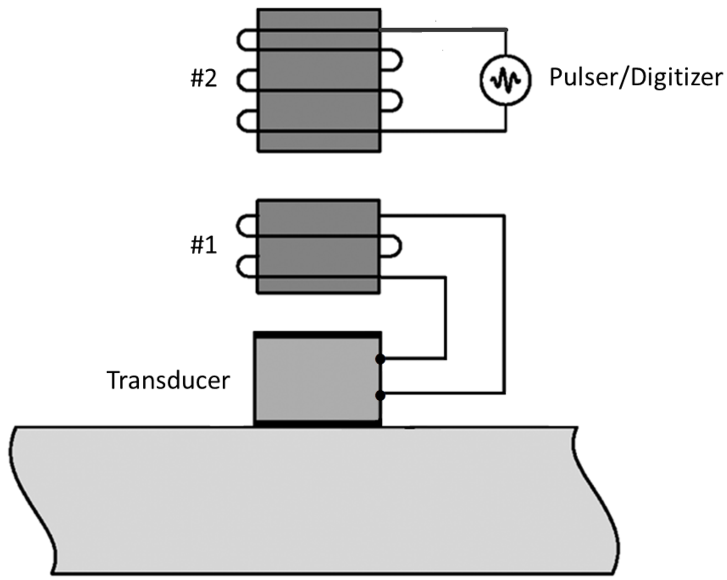

Figure 4-3 The concept of an inductively coupled transducer

4.3 Experimental Work

An experimental system for inductive coupling is built following the prototype shown in Figure 4-3 (Gong et al. 2015). The ferrite cores are PQ-26 type ASTM P7070 power ferrites with a center leg diameter of 12.0 mm, and each coil has 16-turn windings on its ferrite core. Figure 4-4 shows the two ferrite cores at the emitter end when they are facing each other, and the ferrite cores at the receiver end are designed to be the same. The ultrasonic transducers are Krautkramer probes from GE Inspection Technologies (product code: 113-241-591) with a specified center frequency of 0.98 MHz and a moderate bandwidth (@-6dB: ~70%). An NI PXI-5421 arbitrary waveform generator is used to generate a Gaussian-modulated sinusoidal pulse signal with peak-to-peak amplitude of 6.0 V at a center frequency of 1.0 MHz. An NI PXI-5122 digitizer is used to record pitch-catch measurements at a sampling rate of 20 MHz. To improve the signal-to-noise ratio, each recorded ultrasonic signal is an average of 500 measurements. Each ultrasonic signal has duration of 0.25 ms in the experiment. At each experimental step, ultrasonic signals are repeated 50 times with a 15 s interval between two consecutive signals.

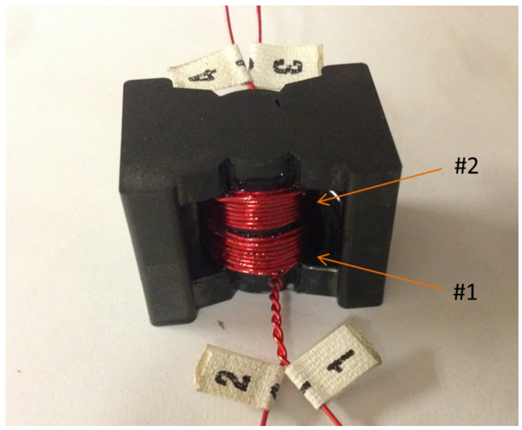

Figure 4-4 A pair of coils used in the experiment for inductive coupling

In this study, the specimen is a thick-walled 6061 aluminum alloy tube with the dimensions (O.D. x I.D. x length) of 4.00 x 2.00 x 3.15 inch (101.60 x 50.80 x 80.01 mm) as shown in Figure 4-5. The outside and inside diameters are typical dimensions of a frac iron component. Aluminum alloy is chosen for our laboratory study for ease of machining a thickness loss similar to the erosion damage of practical interest. The two transducers are glued onto the specimen surface using cyanoacrylate adhesive with an included radial angle of 134.6^{o} to take pitch-catch measurements as shown in Figure 4-5.

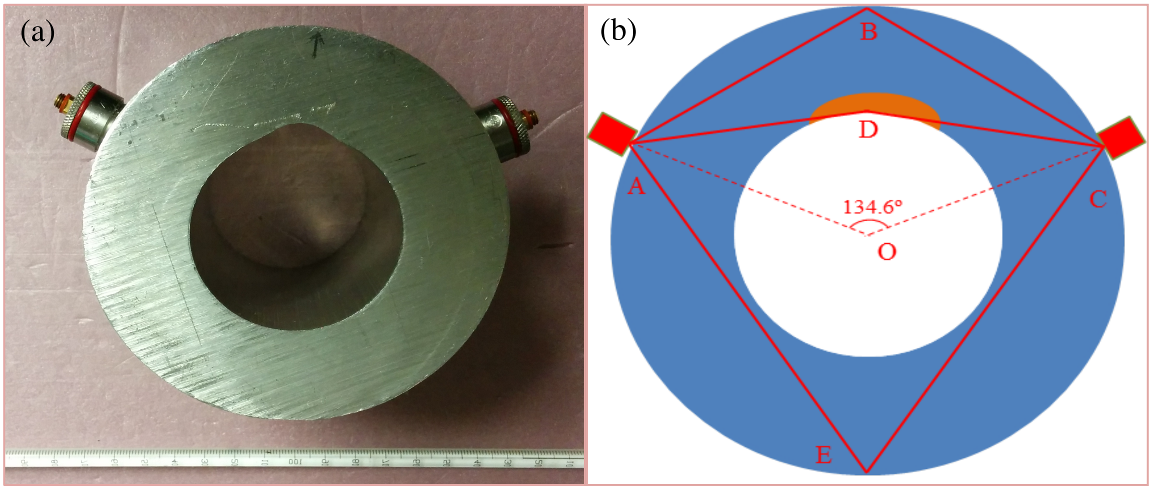

Figure 4-5 (a) The thick-walled aluminum tube and the transducers; (b) an illustration of possible wave paths

In this experiment, six damage levels are introduced by cutting an elliptical damage profile; the damage runs the full-length of the specimen as shown in Figure 4-5. The damage dimensions are listed in Table 4-1. (I will relate ultrasonic measurements to the thickness loss; I will not address possible relationships to the damage width.)

Table 4-1 The damage levels introduced to the aluminum specimen

Damage Level	Thickness Loss (inch)	Thickness Loss (mm)	Approximate Damage Width (inch)	Approximate Damage Width (mm)
0	0.00	0.0	0.0	0
1	0.02	0.5	0.5	13
2	0.04	0.9	0.6	15
3	0.08	1.9	0.6	15
4	0.10	2.6	0.6	15
5	0.11	2.9	0.6	15

4.4 Ultrasonic Time-of-Flight Diffraction for Thickness Loss Quantification

4.4.1 Ultrasonic Time-of-Flight Diffraction

In this section, I will propose a novel method using diffracted ultrasonic longitudinal waves to characterize the thickness loss of the thick-walled aluminum tube (Gong et al. 2015). As shown in Figure 4-5, when longitudinal waves propagate from emitter location A to receiver location C, the shortest path would be A-D-C. The leading pulse will travel along the path A-D-C, and that path will lengthen with damage depth at D. It is evident that longitudinal waves can travel from location A to location D, as indicated in Figure 4-5, but it is not that apparent that ultrasonic waves can change direction at D and continue toward C. This wave path can be explained by ultrasonic diffraction. In the Huygens-Fresnel principle, every point on a wavefront can be treated as a forward-propagating source of a spherical wave and the sum of secondary waves determines the form of the wave at any subsequent time (Fahy 2000). In our case, when the wavefront propagates to D it can be treated as a forward propagating spherical wave source, with a subsequent shortest path to C. This can also explain why the leading pulse, corresponding to Pulse 1 in Figure 4-6, will be sensitive to damage and why I will study this pulse to characterize the thickness loss in our experiment. In this study, the angle of 134.6º is chosen to assure that no direct path exists between the two transducers so that the shortest path length A-D-C will change with damage depth at D. In field application, the location D can be estimated from knowledge of the flow conditions, and transducers can be placed correspondingly at locations A and C.

In our experiment, longitudinal waves are observed to reflect from inner and outer surfaces, and also to propagate around the tube in both circumferential directions and along multiple paths. The experiment also shows that circumferentially propagating longitudinal waves have significant diffraction phenomenon, and the diffracted waves can be used for the quantification of volume loss.

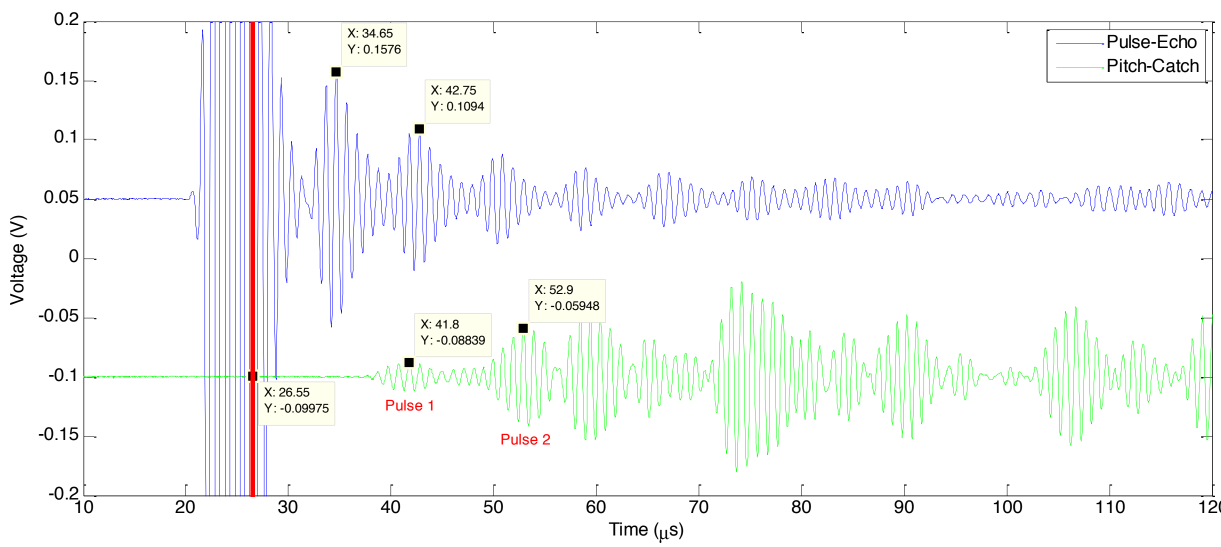

Figure 4-6 The signals received by the emitter and receiver in pulse-echo and in pitch-catch modes from wired transducers

Figure 4-6 shows a pair of signals detected at the emitter (in pulse-echo mode) and the receiver (in pitch-catch mode), respectively, when the specimen is undamaged; the two signals are plotted with DC offset to eliminate overlap. From these two signals, it is determined that pulses 1 and 2 travel from emitter to receiver following paths A-D-C and A-E-C (as denoted in Figure 4-5), respectively. From the pulse-echo signal, echoes from the back-wall reflections can be found clearly. Because no damage occurs at the emitter location, those echoes can be used to calculate the longitudinal wave velocity; in this case the wall thickness is 1.00 inch (25.40 mm) and the time-of-flight between the first two echoes is 8.10

μs, so the longitudinal wave velocity is calculated as 6.27 mm/μs. Here, the time-of-flight between the first two echoes is calculated using the pulse peak locations as labeled in Figure 4-6. Then, the time reference point is calculated as 26.55 μs using the first echo peak location minus the time-of-flight between the first two echoes as indicated by the red line in Figure 4-6. (This time reference point is not the absolute time zero point of the excitation signal, but it is a convenient reference for all time-of-flight calculations.) Using the time reference point, the times-of-flight for pulses 1 and 2 are determined from the pitch-catch signal, from which the travel distance is calculated and listed in Table 4-2. Geometric path lengths for A-D-C and A-E-C, before damage, are measured directly by calipers and are also listed in Table 4-2. The calculated travel distances compare reasonably well with the measured path lengths, supporting our conceptual model of the travel paths.

Table 4-2 Comparison between calculated travel distances and measured path lengths

	Calculated Travel Distance (mm)	Measured Path Length (mm)
Pulse 1	95.64	--
Path A-D-C	--	97.87
Pulse 2	165.25	--
Path A-E-C	--	167.54

4.4.2 Ultrasonic Signals from Wired Transducers and Inductively Coupled Transducers

The experiment was implemented in both the wired setup and the inductively coupled setup, using the same transducers, function generator, and digitizer. Signals obtained from the inductively coupled setup are closely comparable to signals obtained from the wired setup. Figure 4-7(a) shows pitch-catch signals from the two different setups, and Figure 4-7(b) and Figure 4-7(c) zoom in to compare the signals over short (10 μs) intervals. Except for some minor differences, the signals are closely comparable. Crosstalk occurs at roughly 25 μs (when the function generator is operating, but before the ultrasonic pulse reaches the receiver) in the inductively coupled setup but not in the wired setup, as shown in Figure 4-8(a). A constant time offset between the two signals is observed; it is shown early in the signal in Figure 4-8(b), and then 150 μs later, near the end of the signal, in Figure 4-8(c).

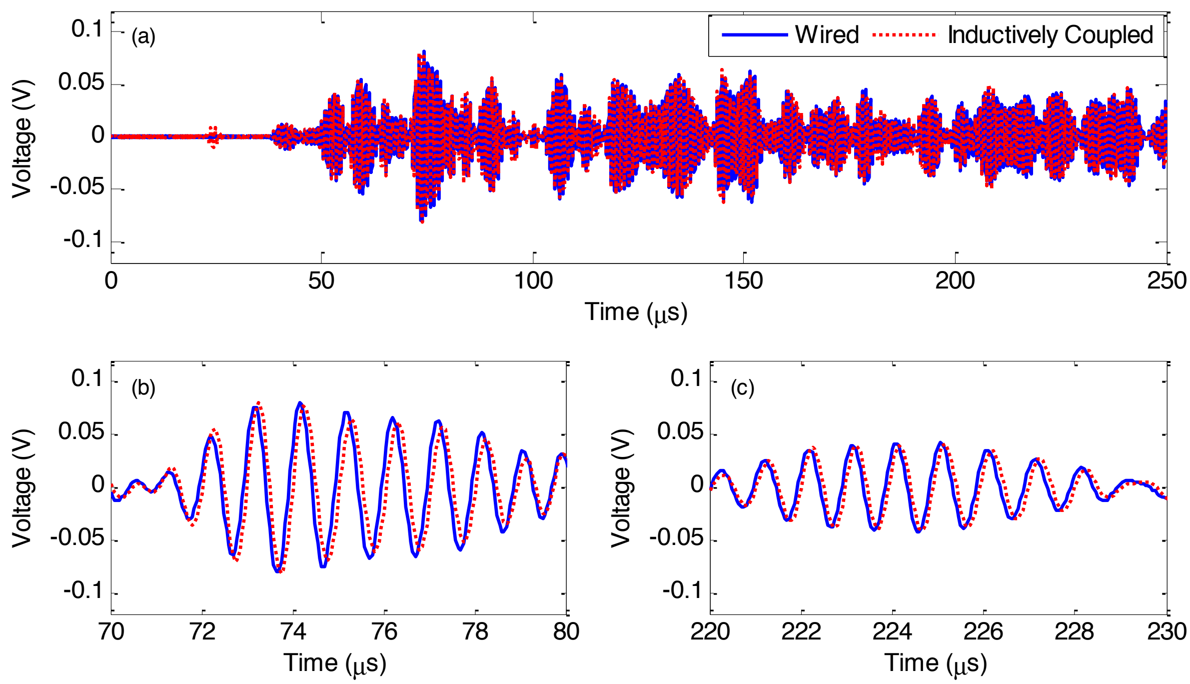

Figure 4-7 (a) Pitch-catch signals from the two different setups; (b) the 70-80 μs segment of the pitch-catch signals; (c) the 220-230 μs segment of the pitch-catch signals

The cross-correlation between the two signals is shown in Figure 4-8(a), indicating that the time offset between the two signals is roughly 0.10 μs, with a maximum correlation coefficient of 0.98. Figure 4-8(b) shows the residuals when the signal from the inductively coupled setup is subtracted from the signal from the wired setup, after adjustment for the constant offset. Although minor differences exist when the signals from the wired setup and the inductively coupled setup are compared to one another, those differences do not affect damage detection performance.

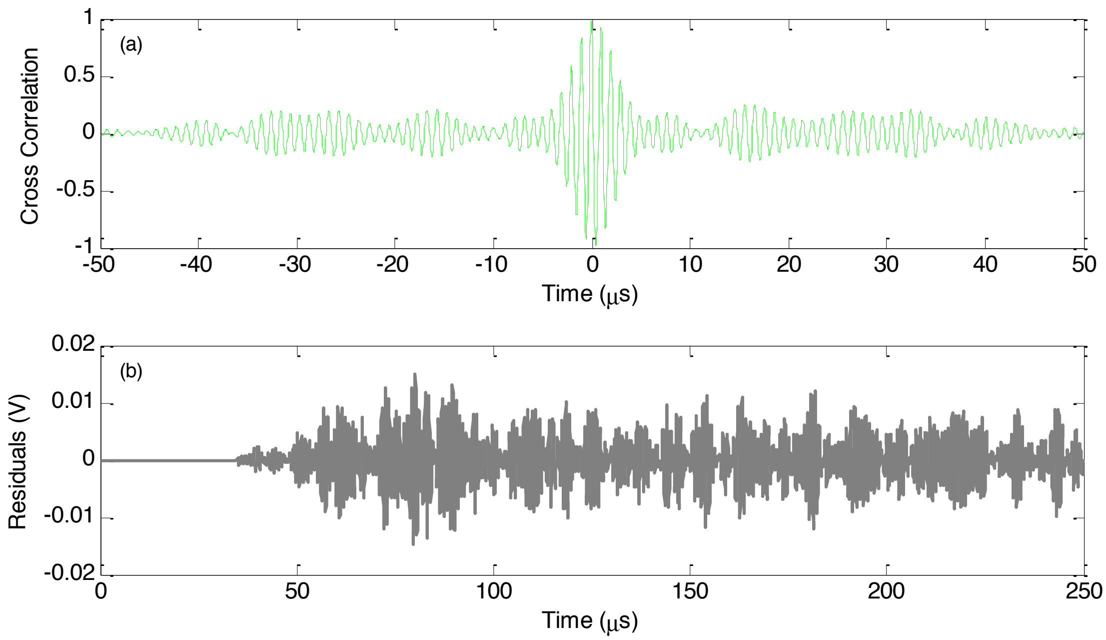

Figure 4-8 (a) Cross-correlation between the two pitch-catch signals in Figure 4-7(a); (b) the difference between the two pitch-catch signals in Figure 4-7(a) (after adjustment for constant offset)

4.4.3 Temperature Compensation

From section 4.4.1, the pulse echoes from back-wall reflections, Pulse 1, and Pulse 2 in Figure 4-6 are all longitudinal waves so that they have the same propagating velocity. In Chapter 2, it has been shown that the pulse echoes in this through-thickness path are not significantly affected by the volume loss because the echoes are geometrically remote from the volume loss. Therefore, the echoes from back-wall reflections can be used for temperature compensation in this time-of-flight diffraction method. To be specific, velocity changes caused by temperature changes can be calculated from the echoes from back-wall reflections, and then velocity changes can be used to calculate the delays or advances of the first arrival at the receiver end caused by temperature changes. Figure 4-9 shows the temperature-caused ultrasonic wave velocity changes in my experiment.

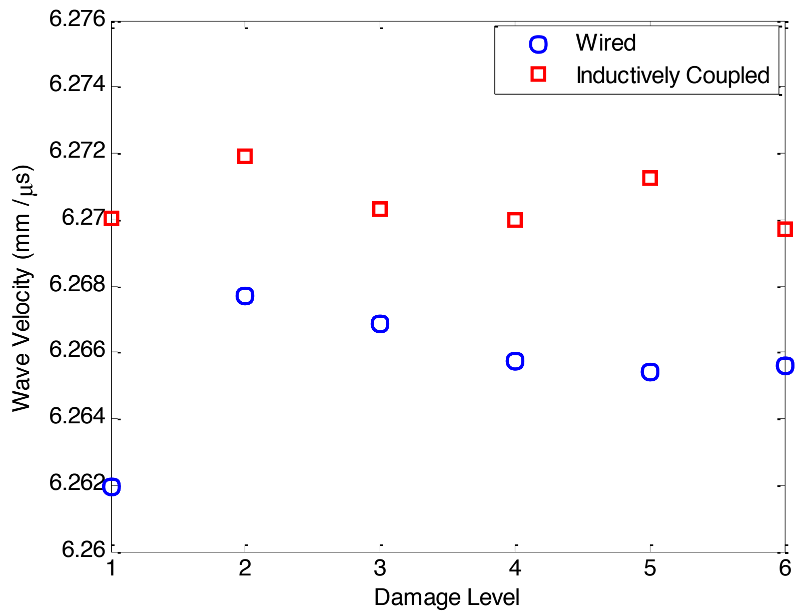

Figure 4-9 The wave velocity changes caused by temperature changes

4.4.4 Influence of Damage Profiles

Even if the damage-caused time delay of the first arrival can be exactly measured, the maximum damage depth can still not be determined exactly because of the influence of the damage profiles. The same maximum damage depth as shown in Figure 4-10 will cause different time delays of the first arrival due to the different damage profiles. The damage profile in Figure 4-10(a) corresponds to the greatest time delay and the damage profile in Figure 4-10(b) corresponds to the smallest time delay when the maximum damage depth is fixed. Time delays from other damage profiles will fall between the greatest and smallest time delays corresponding to the profiles in Figure 4-10. Therefore, the time delay is bounded when the maximum erosion depth is fixed although the exact time delay is not know. Similarly, the maximum damage depth is bounded when the time delay is known, and the lower bound corresponds the damage profile in Figure 4-10(a) and the higher bound corresponds to the damage profile in Figure 4-10(b).

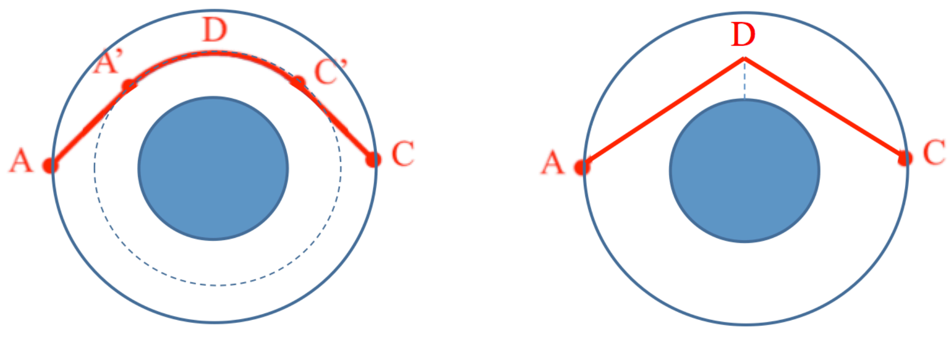

Figure 4-10 Different damage profiles corresponding to: (a) erosion evenly distributed across the section; (b) a vertical crack with the same distance to Point A and Point C. The Point D is at the same location in (a) and (b), so the maximum damage depth is the same for the two different damage profiles.

4.4.5 Results and Discussions

The pitch-catch signal changes with damage level. The time delay of the diffracted ultrasonic leading pulse is used for thickness loss quantification, applying the cross-correlation method to extract that time delay between damage levels, with a Hamming window to prevent sharp changes at the ends of signal. Figure 4-11 shows the leading pulses at the six different damage levels, which are labeled with the measured thickness loss. The original signals have a sampling rate of 20 MHz, so the time resolution will be 0.05 μs if the original signals are directly used in the cross-correlation. However, time delays at different damage levels can be much smaller than 0.05 μs. Therefore, linear interpolation is applied to the original signals to improve the time resolution to 0.0005 μs for the cross-correlation calculation.

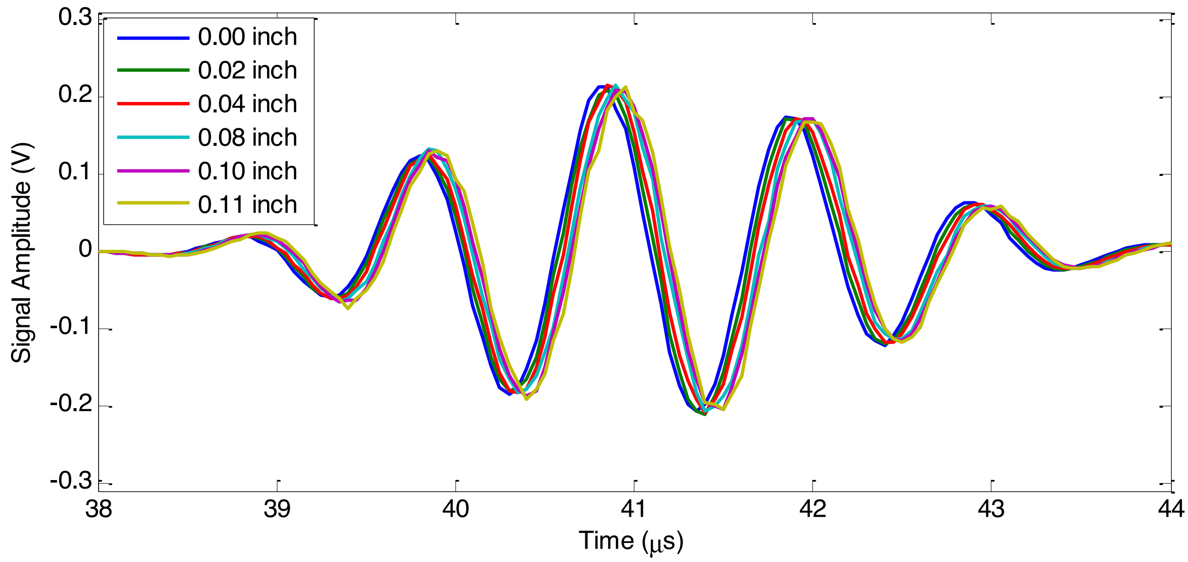

Figure 4-11 The leading pulses with Hamming window at the different damage levels

Figure 4-12 plots the thickness loss against the time delays of the leading pulse referenced to the no-damage signal for the wired transducers. The dotted black lines in this figure are the predicted lower and higher boundaries corresponding to the damage profiles shown in Figure 4-10. In Figure 4-12, the measured data points before temperature compensation are far from the predicted boundaries but those after temperature compensation are very close to the predicted boundaries. This indicates the temperature compensation method introduced in the section 4.4.3 performs well for the damage quantification using the ultrasonic time-of-flight diffraction method. In Figure 4-12, the measured data points are not well bounded by the predicted boundaries even after temperature compensation. This is probably because the predicted values do not consider the influence of instrument errors, environmental noise, or algorithm resolution, and because the temperature compensation method is not perfect. Overall, the time delay from the first arrival shows a monotonic relationship with the thickness loss indicating that the time-of-flight diffraction technique can quantify the thickness loss well for the wired transducers.

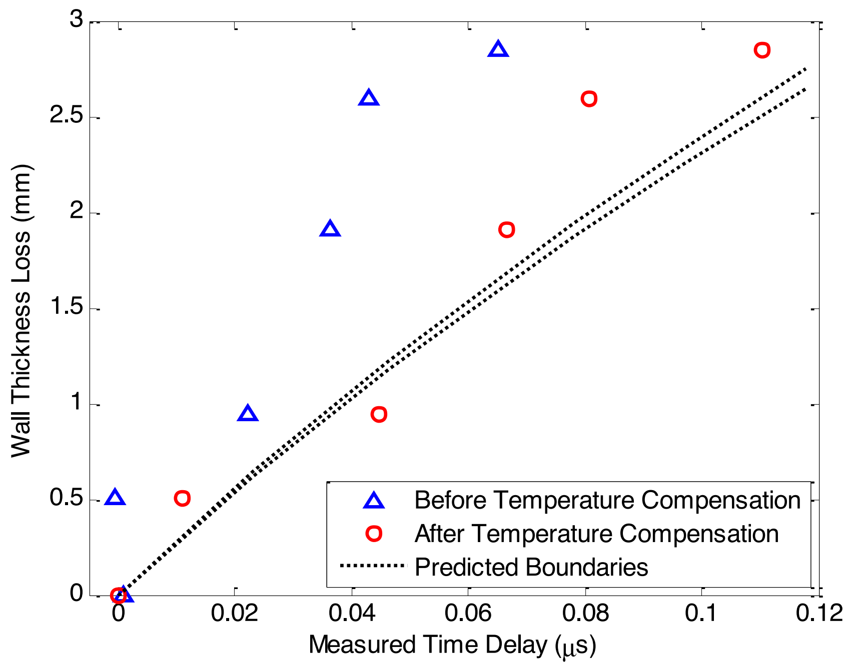

Figure 4-12 The relationship between the time delay of the leading pulse and the erosion depth for wired transducers

Figure 4-13 plots the thickness loss against the time delays of the leading pulse referenced to the no-damage signal for the inductively coupled transducers. Overall, the time delay from the first arrival shows a monotonic relationship with the wall thickness loss indicating that the time-of-flight diffraction technique can quantify the thickness loss well. In Figure 4-13, the measured data points before temperature compensation and after temperature compensation are very close to each other, indicating less temperature variations for the measurements from the inductively coupled transducers. This is due to the experimental procedure. Temperature variations are mainly due to the heat generated by the machining of thickness loss, and the accelerated cooling procedure using ice. The signals from the wired transducers were recorded about three hours after the cooling procedure, and the signals from the inductively coupled transducers were recorded about six hours after the cooling procedure. Therefore, the temperature had not stabilized to room temperature when the signals were recorded from the wired transducers, but had more closely approached to room temperature when the signals were recorded from the inductively coupled transducers. Overall, the inductively coupled transducers and wired transducers have similar performance after temperature compensation, although the results are not exactly the same because of the experimental procedure.

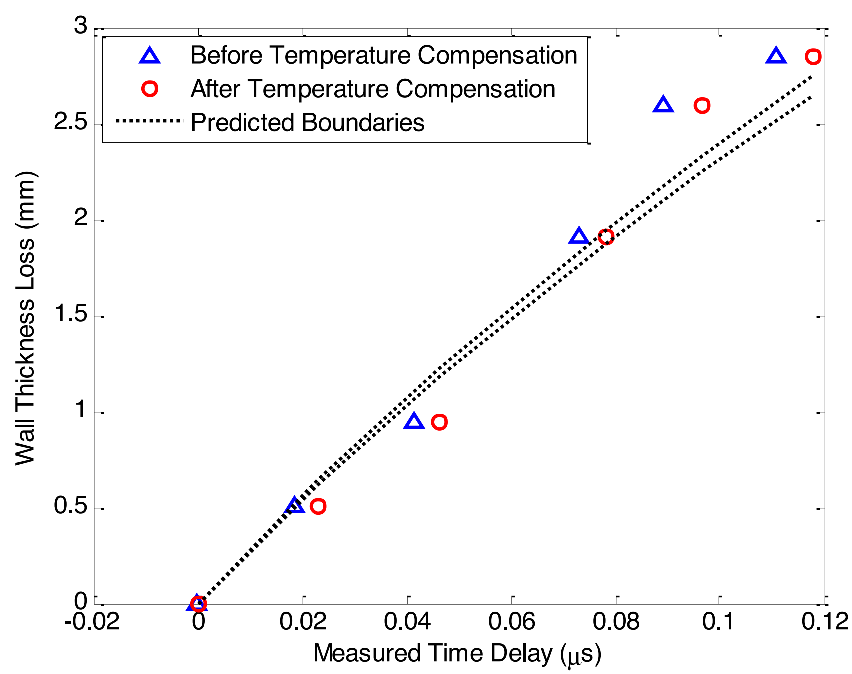

Figure 4-13 The relationship between the time delay of the leading pulse and the erosion depth for inductively coupled transducers

4.5 Conclusion

In this chapter, ultrasonic time-of-flight diffraction is used to quantify the thickness loss in a thick-walled aluminum tube. The diffracted ultrasonic leading pulse in our experiment is shown to be very sensitive to thickness loss, and its time delay monotonically increases with the progress of the thickness loss. A temperature compensation technique based on echoes from back-wall reflections is developed and shows good temperature compensation performance. The effects of damage profiles are also discussed, which provides boundaries for the predictions from the time-of-flight diffraction.

I also demonstrate that the inductively coupled transducers have the similar performance as that of the wired transducers in our experiments. The signals from these two different configurations are closely comparable to one another, and have equivalent performance in producing a monotonic relationship between thickness loss and delay in the arrival time of the leading pulse. In cases where transducers are to be permanently mounted on a structure, including in harsh environments, or in cases where wiring is a major expense, inductively coupled transducers are potentially excellent alternatives.

Chapter 5 Quantification of the Alkali-Silica Reaction Damage in Concrete

5.1 Introduction

[2]U. S. cement consumption (USGS 2003-2012) between 2003 and 2012 averaged 100.0 million metric tons per year, with a standard deviation of 24.4 and with a maximum of 129.8 in 2005. Accordingly, roughly 700 million tons of concrete are constructed each year in the United States in the form of civil infrastructure and buildings. The alkali-silica reaction (ASR) occurs between reactive forms of silica in aggregates and alkalis in cement paste. The reaction product, an amorphous gel, absorbs moisture from the surrounding paste, expands and eventually cracks the aggregate then the paste. The reactivity is potentially harmful when it produces significant expansion.

ASR caused cracking damage was first recognized about 75 years ago (Stanton 1940) and then was the subject of continued concern globally (Swamy 2002; Swamy and Al-Asali 1988). While most aggregate sources are not susceptible to ASR, reactive aggregates are

[2] Portions of this introduction are drawn from a proposal that I drafted and for which I provided all technical content, which was then edited by my research advisor.

nonetheless widespread and history is replete with cases of large-scale damage to major infrastructure and industry investments as reported by the Federal Highway Administration (Folliard et al. 2003). Because of the serious consequences and the widespread risk, research on methods for ASR damage detection has engaged researchers around the world and an excellent treatment can be found in a recent FHWA "Facts Book" (Thomas et al. 2013).

Currently, it is a common practice to use ASTM C1260 (ASTM-C1260 2007) and ASTM C1293 (ASTM-C1293 2008) to screen aggregates before the construction of important concrete structures to avoid potential ASR damage. Researchers (Cruz Carlos et al. 2004; Ideker et al. 2012) have studied and compared the two methods and conclude ASTM C1293 is more realistic and representative of field conditions. However, these methods cannot be used to evaluate the status of existing structures.

Non-destructive evaluation (NDE) techniques based on ultrasonic methods have been widely used by earlier researchers to evaluate the deterioration of concrete material as reflected in its overall material properties. This is first exemplified (ASTM-C597 2009; Yaman et al. 2001) by measuring the ultrasonic pulse velocity (UPV) because it serves as an indicator of elastic modulus; our conventional engineering model of concrete behavior relates the elastic modulus to the compression strength. The UPV has been reported to decrease with the progress of ASR damage (Swamy and Al-Asali 1988). However, The UPV method has also been reported to be not as sensitive as other methods by other researchers (Saint-Pierre et al. 2007; Suaris and Fernando 1987) and our experience is consistent with this latter claim.

The attenuation method is another well studied and widely accepted ultrasonic technique. The ultrasonic attenuation is caused by the scattering and absorbing effects of the concrete. This method has been widely used to evaluate various properties of cement-based materials, such as grain size, air voids, and so forth (Ju et al. 2006; Nair et al. 1989). It has also been shown to have the ability to detect ASR damage in concrete (Saint-Pierre et al. 2007). However, moisture, coupling condition and other factors have very significant influence on attenuation measurements, cause large variations in the measured attenuation, and obscure the attenuation change caused by damage.

In recent years, some nonlinear acoustic techniques have been used to detect damage in concrete and other building materials. When ultrasonic signals propagate through a nonlinear medium, higher order harmonics are generated. The nonlinear parameters based on the harmonics would trace the damage development in the medium since the damage would increase the nonlinearity of the medium. Nonlinear ultrasonic methods based on higher order harmonics have been used to detect damage in building materials (Matlack et al. 2012; Van Den Abeele et al. 2001; Walker 2011), including ASR damage (Chen et al. 2007). Alternately, the nonlinear interaction between a high frequency sinusoidal excitation signal and a low frequency structural vibration would produce a modulated signal. The nonlinear wave modulation spectroscopy (NWMS) measures the cross modulation amplitude to detect the damage in materials (Chen et al. 2009; Van Den Abeele et al. 2001). The nonlinear resonance ultrasound spectroscopy (NRUS) (Payan et al. 2007) and the nonlinear impact resonance acoustic spectroscopy (NIRAS) (Chen et al. 2011) measure a nonlinear parameter by determining the relationship between the resonant frequencies and excitation levels, and then the nonlinear parameter is used to characterize concrete damage. The nonlinear ultrasonic techniques generally have demanding requirements for the testing system, and sometimes the results from nonlinear ultrasonic tests can not be easily interpreted.

In this chapter, I will present three ultrasonic methods to detect the existence of ASR caused cracking damage and to track its progress in concrete. In section 5.2, the experimental work will be detailed. In section 5.3, the three ultrasonic methods used for the detection of ASR caused cracking damage will be presented. The experimental results and discussions are shown in section 5.4. Finally, I will conclude this chapter in section 5.5.

5.2 Specimen Preparation

Three concrete specimens (No.1, No.2 and No.3) are cast with the size of 2.54 × 2.54 × 28.58 cm (1 × 1 × 11.25 inch). For specimens No.1 and No.2, the coarse aggregate is crushed dolomitic limestone with a 1/2-inch nominal maximum size (Aggregate I). It is listed by the Pennsylvania Department of Transportation to have a 0.12% expansion in ASTM C1260. The fine aggregate is crushed sand from the same dolomitic limestone. For specimen No.3, the coarse aggregate is crushed sandstone with a 1/2-inch nominal maximum size (Aggregate II). This aggregate is listed by the Pennsylvania Department of Transportation to have a 0.53% expansion in ASTM C1260. The fine aggregate is non-reactive quartz sand. Type III high-alkali cement from the Essroc Cement Plant in Nazareth, PA is used for all specimens. The equivalent alkali content of the cement is 1.1% by weight. All specimens have the same mixture proportion as Cement: Water: Coarse Aggregate: Fine Aggregate = 500: 235: 1058: 693.

The specimens are cured under moist conditions at room temperature and removed from molds after 24 hours. They are then kept in water for 28 days before test. Then, the lengths of specimens are measured using a length comparator with a precision of 0.000254 cm (0.0001 inch), and ultrasonic measurements are recorded for each specimen. All the above measurements under sound condition are used as baselines. Specimen No.1 is always kept in water at room temperature as a control, and specimens No.2 and No.3 are then immersed in 1N NaOH solution at 80℃ to accelerate ASR damage. The lengths and ultrasonic measurements are further recorded after immersion for 1, 2, 3, and 4 weeks for specimens No.1 and No.2. For specimen No.3, the tests last only for 2 weeks.

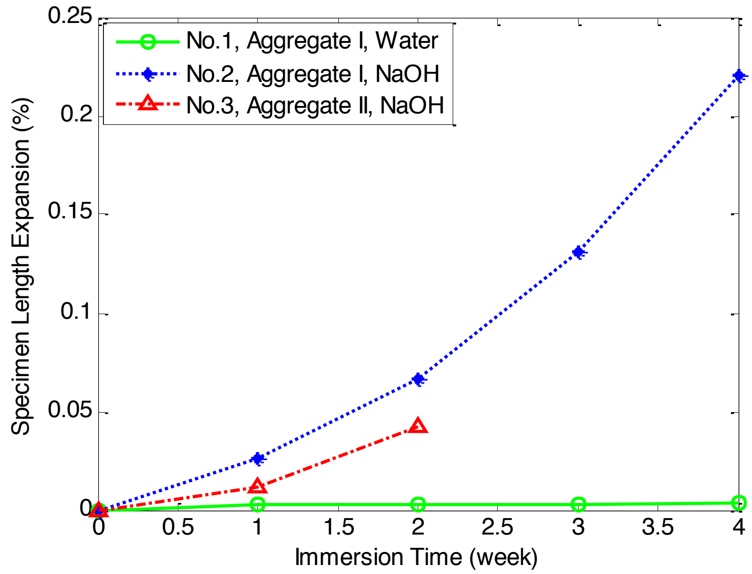

Figure 5-1 Specimen expansions during the tests

Figure 5-1 shows the specimen expansions. Specimen No.1 in water does not have detectable expansion, but specimens No.2 and No.3 immersed in NaOH solution show large expansions, indicating the existence of ASR damage. In specimen No.2, the crushed fine aggregate exposes reactive components to the alkalis more than in the case of the coarse aggregate, so the expansion and damage in specimen No.2 are mainly caused by the fine aggregate. On the other hand, the fine aggregate in specimen No.3 is not reactive, so the expansion and damage in specimen No.3 are dominated by coarse aggregate. This explains why specimen No.2 can have a larger expansion than specimen No.3 with more reactive coarse aggregate.

5.3 The Ultrasonic Test

In this section, I introduce the ultrasonic test and my three signal processing methods for ASR damage detection: attenuation spectrum method, ultrasonic passband method, and stretching factor method.

In my ultrasonic test, two Krautkramer transducers from GE Inspection Technologies (product code: 113-241-591) are used with a specified center frequency of 0.98 MHz and a moderate bandwidth (bandwidth@-6dB: ~70%). A Ritec RPR-4000 high power pulser is used to generate a one-cycle sinusoidal signal with amplitude of roughly 150 V while sweeping the frequency from 200 kHz to 2.0 MHz in 50 kHz steps. An NI PXI-5122 digitizer is used to record the pitch-catch measurements through the 1 inch thickness of the specimens at a sampling rate of 20 MHz. Each signal has duration of 0.25 ms. Measurements are repeated five times at each of the three locations on each specimen.

5.3.1 The Attenuation Spectrum Method

The Ritec pulser in my tests can only generate single-frequency signals. Fortunately, the concrete-transducer is approximately a linear time invariant (LTI) system in a specific test cycle. Therefore, I use the summation of excitations at single frequencies to approximate a wideband excitation, and the summation of corresponding responses to approximate a wideband response. The attenuation spectrum in test cycle i is then defined as the magnitude of the transfer function (Saint-Pierre et al. 2007),

$$A_i(f) = \frac{|FFT(y_i(t))|}{|FFT(x_i(t))|} \tag{5-1}$$

where f is the frequency, $x_i(t)$ and $y_i\ (t)$ are the wideband excitation and response respectively at test cycle i (i = 0, 1, 2, 3, or 4 in this dissertation).

5.3.2 The Ultrasonic Passband Method

In my tests, I anticipate that damage in concrete will cause more attenuation in the high frequency range than in the low frequency range. Then, I model the concrete-transducer system as a physical bandpass filter (Gong et al. 2014; Gong et al. 2014). To quantitatively describe the ultrasonic passband, a cumulative distribution function (CDF) at test cycle i is defined as,

$$CDF_i(f) = \frac{\int_{f_0}^{f} A_i^{0.5}(\rho)d\rho}{\int_{f_0}^{f_1} A_i^{0.5}(\rho)d\rho} \quad (f_0 < f < f_1) \tag{5-2}$$

where f_0 and f_1 are starting and ending frequencies in our tests, $A_i\ (f)$ is the attenuation spectrum as defined in Eq. (5-1).

In the ultrasonic passband method, the concrete damage is detected from changes in the ultrasonic passband in the frequency domain. In contrast, in attenuation spectrum or attenuation methods (Saint-Pierre et al. 2007) the concrete damage is detected from changes in the signal amplitude. That is, the ultrasonic passband method utilizes relative attenuation information, while the attenuation spectrum or attenuation methods utilize absolute attenuation information. Consequently the ultrasonic passband method is unaffected by uniformly distributed attenuation that can be caused by changes in the coupling or other testing conditions.

Although the CDF has been defined to describe the ultrasonic passband, it is not convenient to use the CDF to quantitatively show ultrasonic passband changes caused by damage especially when comparing ultrasonic passband changes for different materials. Therefore, I further define a quantity $\Delta_{CDF}(i)$ to characterize ultrasonic passband changes with time.

$$\Delta_{CDF}(i) = \int_{f_0}^{f_1} CDF_0(f) - CDF_i(f) df \tag{5-3}$$

where $CDF_0(f)$ is the CDF at test cycle 0, and $CDF_i(f)$ is the CDF at test cycle *i*. The quantity $\Delta_{CDF}(i)$ calculates the area between the two CDF curves to show the changes.

5.3.3 The Stretching Factor Method

In my tests, it is found that the response signal is stretched by the ASR damage in concrete (Gong et al. 2014). The stretching effect is approximately modeled as

$$y_{i+1}(t-t_0)=b\cdot y_i(a(t-t_0)),\ a>1 \tag{5-4}$$

where $y_i(t)$ is the response signal at test cycle i, a is the stretching factor, b is a factor used to model the amplitude change, and t_0 is the time zero point of the signal.

The stretching model is not time invariant so that the time zero point is important for the analysis. Theoretically, the time zero point is at the beginning of the excitation. However, I cannot place it exactly because of noise and because of imprecision in the transition zone of the excitation signal.

Here, I propose a method using signal processing to find stretching factors without knowing the time zero point of original signals. As mentioned earlier, the concrete-transducer can be modelled as a LTI system in a given test cycle

$$Y_i(j\omega)=H_i(j\omega)X_i(j\omega) \tag{5-5}$$

where $X_i(j\omega)$ and $Y_i(j\omega)$ are Fourier transforms of $x_i(t)$ and $y_i(t)$ respectively, and $H_i(j\omega)$ is the transfer function. Then, both sides of the Eq. (5-5) are convolved with $X^*(j\omega)$.

$$\begin{aligned}Z_i(j\omega)&=Y_i(j\omega)X_i^*(j\omega)=H_i(j\omega)X_i(j\omega)X_i^*(j\omega)\\&=\left|X_i(j\omega)\right|^2H_i(j\omega)=W_i(j\omega)H_i(j\omega)\end{aligned} \tag{5-6}$$

The signal $z_i(t)$ is the response corresponding to the input $w_i(t)$, which is clearly a real input beginning of a time zero point. If damage has a stretching effect on $y_i(t)$, it should also have the same effect on $z_i(t)$. Therefore, I use $z_i(t)$ instead of $y_i(t)$ for stretching analysis.

5.4 Results and Discussions

Typical attenuation spectra and CDF curves for specimen No.3 are shown in Figure 5-2 and Figure 5-3, respectively. For each attenuation spectrum and each CDF curve, five independent measurements at the specific location are averaged and the error bars represent the standard deviations.

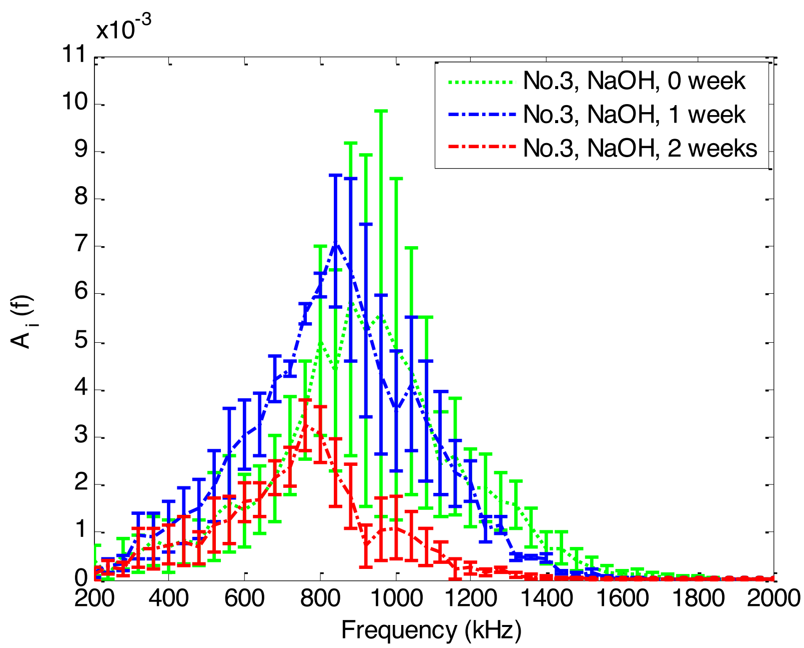

Figure 5-2 The attenuation spectra for specimen No.3

I expect greater attenuation with the progression of ASR damage. However, from Figure 5-2, the attenuation spectra are more complicated. First, the attenuation spectra do not show consistent smaller magnitude after ASR damage. Second, there are large variations covering the magnitude decreases even if they exist. Therefore, the results from the attenuation spectra can be ambiguous and may not be able to detect existing ASR damage.

On the other hand, it is clear from Figure 5-3 that CDF curves calculated from the relative attenuation show a consistent shift to lower frequency range with increasing ASR damage. Also, the error bars indicate that CDF curves have much smaller variations than the attenuation spectra.

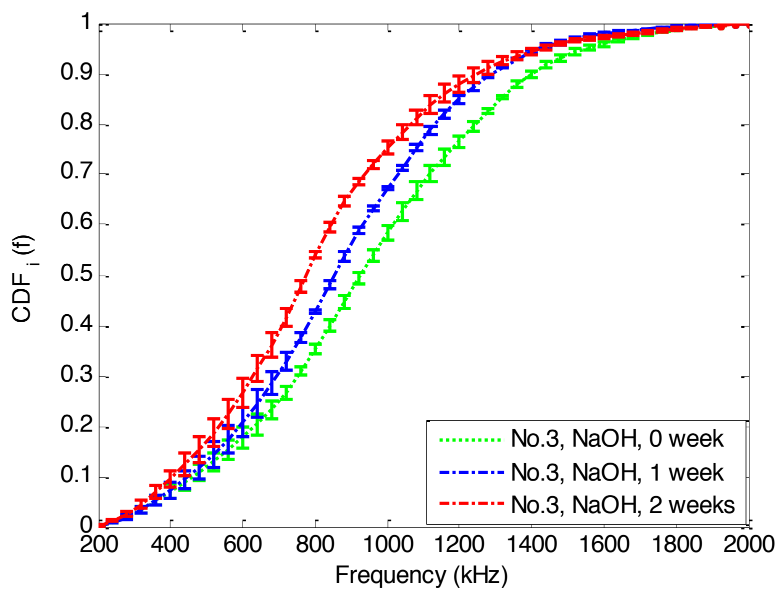

Figure 5-3 The CDF curves for specimen No.3

Figure 5-4 shows ultrasonic passband changes $\Delta_{CDF}(i)$ at three locations on each of the three specimens. For specimen No.1, $\Delta_{CDF}(i)$ decreases with time. In other words, the ultrasonic passband moves towards the high frequency range with time. This can be explained by that the hydration reaction continues in sound concrete and transforms cement compounds into cement paste. The concrete will gain strength in this process, and the higher quality of concrete at later time reduces the attenuation of high frequencies. For specimens No.2 and No.3, $\Delta_{CDF}(i)$ increase with time. In other words, the ultrasonic passbands move towards the low frequency range with time. This can be interpreted as ASR damage causing high frequency components to diminish much than low frequency components. Therefore, the ultrasonic passband method can detect the ASR damage and track its progress well, whether ASR is dominated by fine aggregate or by coarse aggregate.

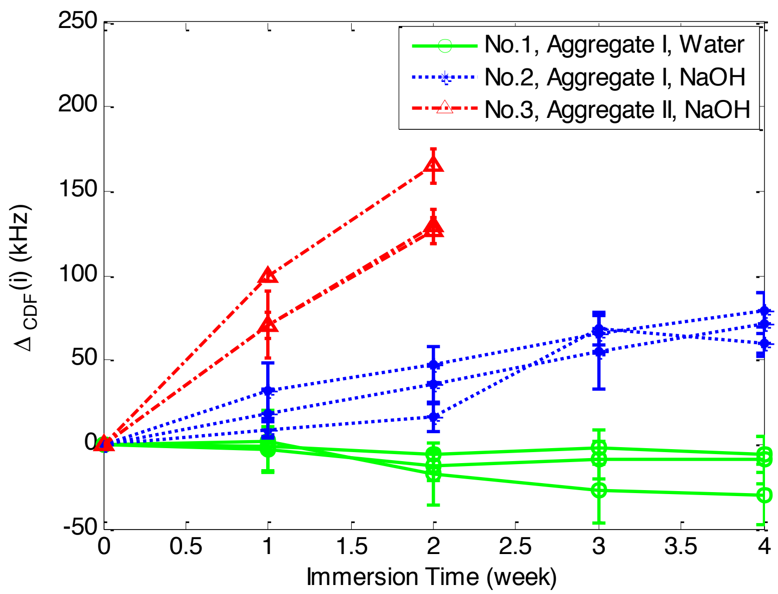

Figure 5-4 The ultrasonic passband changes over time

For the stretching factor method to improve consistently, I select the three signals with largest amplitudes from the five recorded in each test cycle; only 400 kHz signals are used for stretching analysis. In order to reduce errors caused by waveform distortions, the cumulative stretching factors are calculated based on the incremental stretching factors at each subsequent step.

In this chapter, I use the scale transform (Harley and Moura 2011) to extract stretching factors. In Figure 5-5, a typical pair of signals from specimen No.3 is shown to demonstrate the stretching effect. It is obvious that the two signals match each other much better after stretching. The maximum cross-correlation coefficient between the two signals is very close to 1.0 after the stretching is applied, so the stretching model in Eq. (5-4) can characterize the signal changes well.

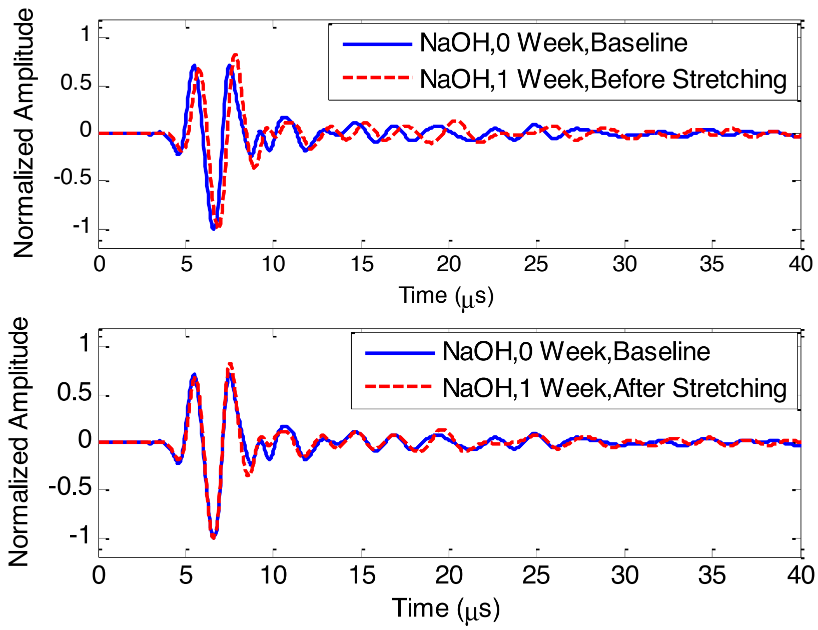

Figure 5-5 A typical pair of signals from specimen No.3 (a) before stretching; (b) after stretching

Figure 5-6 shows cumulative stretching factors at three locations on each of the three specimens. For specimen No.1, the signals are continuously compressed with time. For specimen No.2 and No.3, the signals are continuously stretched with time. These results from stretching factor method are consistent with those from ultrasonic passband method. However, I notice that the results from stretching factor method might have larger variations among multiple locations especially for specimen No.3 in Figure 5-6.

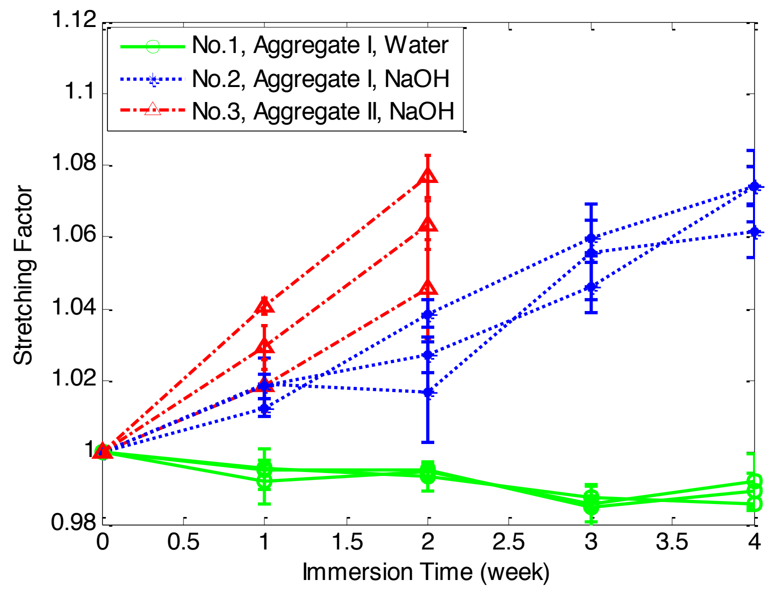

Figure 5-6 The stretching factors

5.5 Conclusion

In this chapter, three ultrasonic methods are studied to detect ASR damage in concrete. The results from the attenuation spectrum (or attenuation methods) exhibit large variations caused by changes in the coupling and testing conditions, and hence these methods cannot detect the ASR damage in concrete without further analysis.

In contrast, my test results with the ultrasonic passband method suggested that it can effectively detect the existence and track the progress of ASR caused cracking damage well when ASR caused cracking damage is present in either fine aggregate or in coarse aggregate. I hypothesize that the ultrasonic passband method is based on the ultrasonic wave filtering effects of cracks in concrete. With the develop of ASR damage in concrete, more high frequency components of ultrasonic waves are filtered out than low frequency components.

My results and analysis support that hypothesis. My test results further show that the stretching factor method can also detect the existence and track the progress of ASR damage, whether the ASR is dominated by the fine aggregate or the coarse aggregate.

Chapter 6 Major Contributions and Future Work

6.1 Major Contributions

This dissertation has been focusing on novel ultrasonic signal processing techniques for damage detection, quantification and temperature compensation. The major contributions achieved in this dissertation are summarized as following:

- **Novel ultrasonic signal processing techniques for temperature compensation in damage detection.** In Chapter 2, in an application based upon erosion loss in frac iron elbows physically simulated in laboratory studies of volume (mass) loss in a thick-walled tube specimens, it is shown that the optimal signal stretching (OOS) method cannot work alone for damage detection when the temperature change is relatively large (±8 °C) and the mass loss is relatively small (0.3 - 0.5 g). The modified OSS method and the SVD method are proposed to compensate the temperature effects for volume loss detection, and they both perform well on the experimental data used in this dissertation.

- **Orthogonal relationship between temperature-induced and damage-induced ultrasonic change signals.** In Chapter 3, the approximate orthogonal relationship between temperature-induced and damage-induced ultrasonic change signals is studied and verified using the same dataset in Chapter 2. The orthogonal relationship can be used to explain why SVD works well under varying temperature conditions; the orthogonal relationship also has the potential to be directly used for damage detection and quantification under some conditions as discussed in section 3.4.2.

- **The ultrasonic time-of-flight diffraction for the quantification of wall thickness loss in thick-walled aluminum tubes.** In Chapter 4, the ultrasonic time-of-flight diffraction technique is proposed to quantify the wall thickness loss of thick-walled aluminum tube specimens, and a temperature compensation technique for this application is also developed. In the experiment, the ultrasonic time-of-flight diffraction worked well, and the experimental results can well fit the theoretical results.

- **The ultrasonic passband technique for the quantification of alkali-silica reaction (ASR) caused cracking damage in concrete.** In Chapter 5, a novel ultrasonic passband technique is proposed to quantify the alkali-silica reaction (ASR) caused cracking damage in concrete structures. This technique is based on the ultrasonic wave filtering effects of cracks in concrete. With the development of ASR damage in concrete, it is hypothesized that high frequency components of ultrasonic waves are filtered out more than low frequency components. In comparison to other methods, this technique overcomes the large variation problem of attenuation-based methods and the poor sensitivity problem of velocity change methods.

6.2 Future Work

In this dissertation, some practical SHM problems have been studied, e.g. the frac iron erosion problem in oil and gas production and the alkali-silica reaction problem in concrete infrastructure systems. These studies have been focusing on novel ultrasonic signal processing techniques for damage detection, quantification and closely related temperature compensation topics. However, I have not assumed (and I do not suggest) that structural health monitoring problems can be fully solved using the techniques developed in this dissertation. The expectation of this dissertation is to push forward the state-of-the-art SHM techniques, and to provide some background for future research work by others.

In Chapter 2, the damage detection problem on thick-walled aluminum tube specimens has been studied to provide some insights into the frac iron erosion problem in oil and gas production. However, extensive studies are still necessary to extend our techniques, developed on thick-walled aluminum tubes, to frac iron component monitoring in field applications. In practice, the frac iron components are much more complicated in terms of geometric shapes and damage morphology than the aluminum tubes used in our study, although our aluminum tubes have cross-sectional dimensions closely comparable to those of exemplar frac iron components. Moreover, frac iron components operate in hash conditions, where the working pressure can be as high as 15000 psi and fracking fluid flows through the components containing abrasive particles (Haddad et al. 2011).

In Chapter 2, it is shown that the optimal signal stretching (OSS) method cannot work alone for damage detection when the temperature change is relatively large (±8 °C) and the mass loss is relatively small (0.3-0.5 g). Then the modified OSS method and the SVD method are proposed to detect volume loss under temperature variations, and they both perform well on the data used in this thesis. However, extensive studies are still needed to know whether these techniques could apply to data collected on other structures under various conditions.

In Chapter 3, the orthogonal relationship between temperature-induced and damage-induced ultrasonic change signals is studied using the same dataset in Chapter 2 and potential applications are discussed. The orthogonal relationship is believed to originate from "randomness" in the damage-induced change signals. The "randomness" here means that scattered ultrasonic pulses do not have a clear pattern and are somewhat randomly distributed in ultrasonic signals. Then a hypothesis that the "randomness" depends on the geometric complexity of structures might be true. It is possible that the greater complexity ("randomness") in ultrasonic signals occurs because the complicated geometric shapes create more possible wave paths. Therefore, the orthogonal relationship might be more obvious on complicated structures but less obvious on simple structures. Future work is needed to verify or deny this hypothesis.

In Chapter 4, the case is similar to that Chapter 2 that the study has only been carried out on thick-walled aluminum tube specimens instead of frac iron steel components. Therefore, further studies are needed to extend the time-of-flight diffraction quantification technique developed on aluminum tubes to frac iron component monitoring in field applications.

In Chapter 5, the novel ultrasonic passband technique is proposed to quantify the alkali-silica reaction (ASR) caused cracking damage in concrete structures. As a comparison, this technique overcomes the large variation problem of attenuation-based methods and the poor sensitivity problem of velocity change methods. This ultrasonic passband technique might not be limited to ASR-caused cracking, and (in principle) it can probably apply to any SHM problems with distributed material damage. The ultrasonic passband technique can be a full model-based method if the filtering effects of cracking damage can be modeled, but such modeling of filtering effects (of cracking damage) will need rigorous research study in the future.

References

Anton, S. R., Inman, D. J., and Park, G. (2009). "Reference-free damage detection using instantaneous baseline measurements." *AIAA journal*, 47(8), 1952-1964.

ASTM-C597 (2009). "Standard test method for pulse velocity through concrete." *American Society for Testing and Materials*.

ASTM-C1260 (2007). "Standard test method for potential alkali reactivity of aggregates (mortar-bar method)." *American Society for Testing and Materials*.

ASTM-C1293 (2008). "Standard test method for determination of length change of concrete due to alkali-silica reaction." *American Society for Testing and Materials*.

Bryt, O., and Elad, M. (2008). "Compression of facial images using the K-SVD algorithm." *Journal of Visual Communication and Image Representation*, 19(4), 270-282.

Catbas, F. N., Susoy, M., and Frangopol, D. M. (2008). "Structural health monitoring and reliability estimation: Long span truss bridge application with environmental monitoring data." *Engineering Structures*, 30(9), 2347-2359.

Charlesworth, J. P., and Temple, J. A. G. (2001). *Engineering Applications of Ultrasonic Time-of-Flight Diffraction*, Research Studies Press, Hertfordshire, England.

Chen, J., Jayapalan, A. R., Kim, J.-Y., Kurtis, K. E., and Jacobs, L. J. (2009). "Nonlinear wave modulation spectroscopy method for ultra-accelerated alkali-silica reaction assessment." *ACI Materials Journal*, 106(4), 340-348.

Chen, J., Jayapalan, A. R., Kurtis, K. E., Kim, J. Y., and Jacobs, L. J. (2007). "Assessment of alkali-silica reaction damage in mortars with nonlinear ultrasonic techniques." *Proc., 34th Annual Review of Progress in Quantitative Nondestructive Evaluation*, Golden, CO, 1345-1352.

Chen, J., Kim, J.-Y., Kurtis, K. E., and Jacobs, L. J. (2011). "Theoretical and experimental study of the nonlinear resonance vibration of cementitious materials with an application to damage characterization." *The Journal of the Acoustical Society of America*, 130(5), 2728-2737.

Cho, S., Yun, C.-B., Lynch, J. P., Zimmerman, A. T., Spencer Jr, B. F., and Nagayama, T. (2008). "Smart wireless sensor technology for structural health monitoring of civil structures." *Steel Structures*, 8(4), 267-275.

Clarke, T., Simonetti, F., and Cawley, P. (2010). "Guided wave health monitoring of complex structures by sparse array systems: influence of temperature changes on performance." *Journal of Sound and Vibration*, 329(12), 2306-2322.

Clausen, C., and Wechsler, H. (2000). "Color image compression using PCA and backpropagation learning." *Pattern Recognition*, 33(9), 1555-1560.

Cross, E., Manson, G., Worden, K., and Pierce, S. (2012). "Features for damage detection with insensitivity to environmental and operational variations." *Proceedings of the Royal Society A: Mathematical, Physical and Engineering Science*, 468(2148), 4098-4122.

Croxford, A., Wilcox, P., Drinkwater, B., and Konstantinidis, G. (2007). "Strategies for guided-wave structural health monitoring." *Proceedings of the Royal Society A: Mathematical, Physical and Engineering Science*, 463(2087), 2961-2981.

Croxford, A. J., Moll, J., Wilcox, P. D., and Michaels, J. E. (2010). "Efficient temperature compensation strategies for guided wave structural health monitoring." *Ultrasonics*, 50(4), 517-528.

Cruz Carlos, J., Mancio, M., Shomglin, K., Harvey, J., Monteiro, P., and Ali, A. (2004). "Accelerated laboratory testing for alkali-silica reaction using ASTM 1293 and comparison with ASTM 1260." California Department of Transportation.

Edwards, G. R., and Gan, T.-H. (2007). "Detection of corrosion in offshore risers using guided ultrasonic waves." *Proc., 26th International Conference on Offshore Mechanics and Arctic Engineering*, San Diego, California, 377-384.

Eybpoosh, M., Berges, M., and Noh, H. Y. (2015). "Sparse representation of ultrasonic guided‐waves for robust damage detection in pipelines under varying environmental and operational conditions." *Structural Control and Health Monitoring*.

Eybpoosh, M., Berges, M., and Noh, H. Y. (2015). "Temperature variation effects on sparse representation of guided-waves for damage diagnosis in pipelines." *Proc., SPIE Smart Structures and Materials+ Nondestructive Evaluation and Health Monitoring*, San Diego, California, 94371N.

Fahy, F. J. (2000). *Foundations of Engineering Acoustics*, Academic Press, Oxford, UK.

Farrar, C. R., and Worden, K. (2007). "An introduction to structural health monitoring." *Philosophical Transactions of the Royal Society A: Mathematical, Physical and Engineering Sciences*, 365(1851), 303-315.

Folliard, K. J., Thomas, M. D. A., and Kurtis, K. E. (2003). "Guidelines for the use of lithium to mitigate or prevent ASR." Federal Highway Administration, FHWA-RD-03-047.

Fukuhara, M., and Yamauchi, I. (1993). "Temperature dependence of the elastic moduli, dilational and shear internal frictions and acoustic wave velocity for alumina,(Y) TZP and β' -sialon ceramics." *Journal of Materials Science*, 28(17), 4681-4688.

Gao, J., Ploennigs, J., and Berges, M. (2015). "A data-driven meta-data inference framework for building automation systems." *Proc., The 2nd ACM International Conference on Embedded Systems for Energy-Efficient Built Environments*, New York, NY, 23-32.

Gautschi, G. (2002). *Piezoelectric sensorics: force, strain, pressure, acceleration and acoustic emission sensors, materials and amplifiers*, Springer, Berlin, Germany.

Gharibnezhad, F., Mujica, L. E., and Rodellar, J. (2011). "Comparison of two robust PCA methods for damage detection in presence of outliers." *Proc., The 9th International Conference on Damage Assessment of Structures*, Oxford, United Kingdom, 012009.

Giurgiutiu, V. (2007). *Structural Health Monitoring: With Piezoelectric Wafer Active Sensors*, Academic Press, Oxford, UK.

Gong, P., Hay, T. R., Greve, D. W., and Oppenheim, I. J. (2015). "Volumetric loss quantification using ultrasonic inductively coupled transducers." *Proc., SPIE Smart Structures and Materials+ Nondestructive Evaluation and Health Monitoring*, San Diego, CA, 943514.

Gong, P., Patton, M. E., Greve, D. W., Harley, J. B., Junker, W. R., Liu, C., and Oppenheim, I. J. (2014). "ASR damage detection in concrete from ultrasonic methods." *Proc., SPIE Smart Structures and Materials+ Nondestructive Evaluation and Health Monitoring*, San Diego, CA, 90610E.

Gong, P., Patton, M. E., Greve, D. W., Harley, J. B., Liu, C., and Oppenheim, I. J. (2014). "Alkali-silica reaction (ASR) detection in concrete from frequency dependent ultrasonic attenuation." *Proc., The 40th Annual Review of Progress in Qauntitative Nondestructive Evaluation*, Baltimore, MD, 909-916.

Greve, D., Zheng, P., and Oppenheim, I. (2007). "Excitation of longitudinal and Lamb waves in plates by edge-mounted transducers." *Proc., IEEE Ultrasonics Symposium*, New York, NY, 1120-1123.

Greve, D. W., Oppenheim, I. J., and Zheng, P. (2008). "Lamb waves and nearly-longitudinal waves in thick plates." *Proc., The 15th International Symposium on: Smart Structures and Materials & Nondestructive Evaluation and Health Monitoring*, San Diego, CA, 69321I.

Greve, D. W., Sohn, H., Yue, C. P., and Oppenheim, I. J. (2007). "An inductively coupled lamb wave transducer." *Sensors Journal, IEEE*, 7(2), 295-301.

Haddad, Z. A., Smith, M. B., de Moraes, F. D., and Moreira, O. M. M. (2011). "The design and execution of frac jobs in the ultra deepwater lower tertiary wilcox formation."

Proc., SPE Annual Technical Conference and Exhibition, Denver, Colorado, 147237-MS.

Harley, J. B., and Moura, J. M. (2011). "Guided wave temperature compensation with the scale-invariant correlation coefficient." *Proc., IEEE Ultrasonics Symposium*, Orlando, FL.

Harley, J. B., and Moura, J. M. (2012). "Scale transform signal processing for optimal ultrasonic temperature compensation." *Ultrasonics, Ferroelectrics, and Frequency Control, IEEE Transactions on*, 59(10).

Harley, J. B., and Moura, J. M. (2014). "Data-driven matched field processing for Lamb wave structural health monitoring." *The Journal of the Acoustical Society of America*, 135(3), 1231-1244.

Hawker, B., Newton, K., and Wein, A. (1985). "Sizing defects in complex geometries underwater by ultrasonic TOFD." *Proc., The 20th Annual British Conference on NDT*, Erskine, Strathclyde, Scotland, 171 - 185.

Ideker, J. H., Bentivegna, A. F., Folliard, K. J., and Juenger, M. C. G. (2012). "Do current laboratory test methods accurately predict alkali-silica reactivity?" *ACI Materials Journal*, 109(4), 395-402.

Ihn, J.-B., and Chang, F.-K. (2008). "Pitch-catch active sensing methods in structural health monitoring for aircraft structures." *Structural Health Monitoring*, 7(1), 5-19.

Jade, A., Srikanth, B., Jayaraman, V., Kulkarni, B., Jog, J., and Priya, L. (2003). "Feature extraction and denoising using kernel PCA." *Chemical Engineering Science*, 58(19), 4441-4448.

Jessop, T., and Mudge, P. (1980). "Size measurement and characterisation of weld defects by ultrasonic testing, Part 1: Non-planar defects in ferritic steels." *Non-destructive examination in relation to structural integrity*, The Welding Institute, 3527-4-77.

Jha, S. K., and Yadava, R. (2011). "Denoising by singular value decomposition and its application to electronic nose data processing." *Sensors Journal, IEEE*, 11(1), 35-44.

Jolliffe, I. (2002). *Principal Component Analysis*, Springer-Verlag, New York, NY.

Ju, J. W., Weng, L.-S., and Liu, Y. (2006). "Ultrasonic frequency-dependent amplitude attenuation characteristics technique for nondestructive evaluation of concrete." *ACI Materials Journal*, 103(3), 177-185.

Keilers, C. H., and Chang, F.-K. (1995). "Identifying delamination in composite beams using built-in piezoelectrics: part I—experiments and analysis." *Journal of Intelligent Material Systems and Structures*, 6(5), 649-663.

Kessler, S. S., Spearing, S. M., and Soutis, C. (2002). "Damage detection in composite materials using Lamb wave methods." *Smart Materials and Structures*, 11(2), 269.

Kołakowski, P. (2007). "Structural health monitoring–a review with the emphasis on low-frequency methods." *Engineering Transactions*, 55(3), 239–275.

Koo, K., Brownjohn, J., List, D., and Cole, R. (2013). "Structural health monitoring of the Tamar suspension bridge." *Structural Control and Health Monitoring*, 20(4), 609-625.

Laory, I., Trinh, T. N., and Smith, I. F. (2011). "Evaluating two model-free data interpretation methods for measurements that are influenced by temperature." *Advanced Engineering Informatics*, 25(3), 495-506.

Liu, C., Harley, J., O'Donoughue, N., Ying, Y., Altschul, M. H., Garrett Jr, J. H., Moura, J. M., Oppenheim, I. J., and Soibelman, L. (2012). "Ultrasonic monitoring of a pipe under operating conditions." *Proc., SPIE Smart Structures and Materials+ Nondestructive Evaluation and Health Monitoring*, San Diego, CA, 83450B.

Liu, C., Harley, J. B., Bergés, M., Greve, D. W., Junker, W. R., and Oppenheim, I. J. (2014). "A robust baseline removal method for guided wave damage localization." *Proc., SPIE Smart Structures and Materials+ Nondestructive Evaluation and Health Monitoring*, San Diego, CA, 90611K.

Liu, C., Harley, J. B., Bergés, M., Greve, D. W., and Oppenheim, I. J. (2015). "Robust ultrasonic damage detection under complex environmental conditions using singular value decomposition." *Ultrasonics*, 58, 75-86.

Liu, C., Harley, J. B., O'Donoughue, N., Ying, Y., Bergés, M., Altschul, M. H., Garrett Jr, J. H., Greve, D., Moura, J. M., and Oppenheim, I. J. (2012). "Ultrasonic scatterer detection in a pipe under operating conditions using singular value decomposition." *Proc., Review of Progress in Quantitative Nondestructive Evaluation*, Denver, Colorado, 1454-1461.

Liu, C., Harley, J. B., Ying, Y., Oppenheim, I. J., Bergés, M., Greve, D. W., and Garrett, J. H. (2013). "Singular value decomposition for novelty detection in ultrasonic pipe monitoring." *Proc., SPIE Smart Structures and Materials+ Nondestructive Evaluation and Health Monitoring*, San Diego, CA, 86921R.

Lu, Y., and Michaels, J. E. (2005). "A methodology for structural health monitoring with diffuse ultrasonic waves in the presence of temperature variations." *Ultrasonics*, 43(9), 717-731.

Lynch, J. P. (2007). "An overview of wireless structural health monitoring for civil structures." *Philosophical Transactions of the Royal Society A: Mathematical, Physical and Engineering Sciences*, 365(1851), 345-372.

Lynnworth, L. C. (2013). *Ultrasonic Measurements for Process Control: Theory, Techniques, Applications*, Academic Press, San Diego, CA.

Matlack, K. H., Wall, J. J., Kim, J.-Y., Qu, J., Jacobs, L. J., and Viehrig, H.-W. (2012). "Evaluation of radiation damage using nonlinear ultrasound." *Journal of Applied Physics*, 111(5), 054911.

Michaels, J. E., Croxford, A. J., and Wilcox, P. D. (2008). "Imaging algorithms for locating damage via in situ ultrasonic sensors." *Proc., IEEE Sensors Applications Symposium*, Atlanta, GA, 63-67.

Michaels, T. E., Michaels, J. E., and Cobb, A. C. (2009). "Simultaneous ultrasonic monitoring of crack growth and dynamic loads during full scale fatigue tests of aircraft wings." *Proc., The 35th Annual Review of Progress in Quantitative Nondestructive Evaluation*, Chicago (Illinois), 1458-1465.

Mujica, L., Rodellar, J., Fernandez, A., and Guemes, A. (2011). "Q-statistic and T2-statistic PCA-based measures for damage assessment in structures." *Structural Health Monitoring*, 10(5), 539-553.

Mujica, L. E., Vehi, J., Ruiz, M., Verleysen, M., Staszewski, W., and Worden, K. (2008). "Multivariate statistics process control for dimensionality reduction in structural assessment." *Mechanical Systems and Signal Processing*, 22(1), 155-171.

Nair, S. M., Hsu, D. K., and Rose, J. H. (1989). "Porosity estimation using the frequency dependence of the ultrasonic attenuation." *Journal of Nondestructive Evaluation*, 8(1), 13-26.

Newton, K., Wein, A., and Hawker, B. (1986). "Research into new techniques for the detection and sizing of defects in subsea steel constructions." *Proc., Underwater Technology Conference*, Bergen, Norw, 89-112.

Payan, C., Garnier, V., Moysan, J., and Johnson, P. A. (2007). "Applying nonlinear resonant ultrasound spectroscopy to improving thermal damage assessment in concrete." *The Journal of the Acoustical Society of America*, 121(4), EL125-EL130.

PHMSA (2011). "Reporting Criteria Changes – 1990-Current." *The United States Department of Transportation Pipeline and Hazardous Materials Safety Administration Office of Pipeline Safety*, <http://primis.phmsa.dot.gov/comm/reports/safety/docs/IncidentReportingCriteriaHistory1990-2011.pdf%3E>. (Feb 21, 2015).

PHMSA (2015). "Pipeline incident 20 year trend." *The United States Department of Transportation Pipeline and Hazardous Materials Safety Administration Office of Pipeline Safety*, <https://hip.phmsa.dot.gov/analyticsSOAP/saw.dll?Portalpages&NQUser=PDM_WEB_USER&NQPassword=Public_Web_User1&PortalPath=%2Fshared%2FPDM Public Website%2F_portal%2FSC Incident Trend&Page=All Reported%3E>. (Feb 21, 2015).

Rose, J. L. (2004). *Ultrasonic Waves in Solid Media*, Cambridge University Press, Cambridge, UK.

Ruotolo, R., and Surace, C. (1999). "Using SVD to detect damage in structures with different operational conditions." *Journal of sound and vibration*, 226(3), 425-439.

Rytter, A. (1993). "Vibrational based inspection of civil engineering structures." Ph.D. Thesis, University of Aalborg, Aalborg, Denmark.

Saint-Pierre, F., Rivard, P., and Ballivy, G. (2007). "Measurement of alkali–silica reaction progression by ultrasonic waves attenuation." *Cement and Concrete Research*, 37(6), 948-956.

Salama, K., and Ling, C. (1980). "The effect of stress on the temperature dependence of ultrasonic velocity." *Journal of Applied Physics*, 51(3), 1505-1509.

Silk, M. (1979). "Accurate techniques for defect sizing in pressurized components." *Proc., Conference on Periodic Inspection of Pressurized Components*, London, UK, 155-162.

Silk, M. (1979). "A separable probe technique for accurate crack sizing using ultrasonic diffraction." *Proc., Ultrasonics International*, Graz, Austria, 415-426.

Silk, M. (1982). "Defect detection and sizing in metals using ultrasound." *International Materials Reviews*, 27(1), 28-50.

Silk, M. (1982). "The fundamental accuracy of ultrasonic time of flight testing techniques." *Proc., Periodic Inspection of Pressurized Components*, London, UK, 125-133.

Silk, M. (1984). "The use of diffraction-based time-of-flight measurements to locate and size defects." *British Journal of Non-destructive Testing*, 26(4), 208-213.

Silk, M., and Lidington, B. (1975). "Defect sizing using an ultrasonic time-delay approach." *Brit. J. Non-Destructive Testing*, 17(2), 33-36.

Stanton, T. E. (1940). "Expansion of concrete through reaction between cement and aggregate." *Proceedings of the ASCE*, 1781-1811.

Suaris, W., and Fernando, V. (1987). "Detection of crack growth in concrete from ultrasonic intensity measurements." *Materials and Structures*, 20(3), 214-220.

Swamy, R., and Al-Asali, M. (1988). "Engineering properties of concrete affected by alkali-silica reaction." *ACI Materials Journal*, 85(5), 367-374.

Swamy, R. N. (2002). *The Alkali-Silica Reaction In Concrete*, Blackie and Son Ltd, Glasgow, UK.

Swamy, R. N., and Al-Asali, M. M. (1988). "Engineering properties of concrete affected by alkali-silica reaction." *ACI Materials Journal*, 85(5), 367-374.

Thomas, M. D. A., Fournier, B., and Folliard, K. J. (2013). "Alkali-aggregate reactivity (AAR) facts book." Federal Highway Administration, FHWA-HIF-13-019.

USGS (2003-2012). "Cement." *Minerals Yearbook*, <http://minerals.usgs.gov/minerals/pubs/commodity/cement/%3E>. (Nov. 20, 2015).

Van Den Abeele, K. E., Sutin, A., Carmeliet, J., and Johnson, P. A. (2001). "Micro-damage diagnostics using nonlinear elastic wave spectroscopy (NEWS)." *NDT & E International*, 34(4), 239-248.

Vanlanduit, S., Parloo, E., Cauberghe, B., Guillaume, P., and Verboven, P. (2005). "A robust singular value decomposition for damage detection under changing operating conditions and structural uncertainties." *Journal of Sound and Vibration*, 284(3), 1033-1050.

Walker, S. V. (2011). "Characterization of fatigue damage in A36 steel specimens using nonlinear rayleigh surface waves." M.S. Thesis, Georgia Institute of Technology.

Wang, C., and Chang, F. (1999). "Built-in diagnostics for impact damage identification of composite structures." *Proc., The 2nd International Workshop on Structural Health Monitoring*, Stanford, California, 8-10.

Weaver, R. L., and Lobkis, O. I. (2000). "Temperature dependence of diffuse field phase." *Ultrasonics*, 38(1), 491-494.

Yaman, I. O., Inci, G., Yesiller, N., and Aktan, H. M. (2001). "Ultrasonic pulse velocity in concrete using direct and indirect transmission." *ACI Materials Journal*, 98(6), 450.

Yan, A.-M., Kerschen, G., De Boe, P., and Golinval, J.-C. (2005). "Structural damage diagnosis under varying environmental conditions—part I: a linear analysis." *Mechanical Systems and Signal Processing*, 19(4), 847-864.

Yan, A.-M., Kerschen, G., De Boe, P., and Golinval, J.-C. (2005). "Structural damage diagnosis under varying environmental conditions—part II: local PCA for non-linear cases." *Mechanical Systems and Signal Processing*, 19(4), 865-880.

Yu, L., Santoni-Bottai, G., Xu, B., Liu, W., and Giurgiutiu, V. (2008). "Piezoelectric wafer active sensors for in situ ultrasonic-guided wave SHM." *Fatigue & Fracture of Engineering Materials & Structures*, 31(8), 611-628.

Zang, C., and Imregun, M. (2001). "Structural damage detection using artificial neural networks and measured FRF data reduced via principal component projection." *Journal of Sound and Vibration*, 242(5), 813-827.

Zhang, D., Chen, S., and Zhou, Z.-H. (2005). "A new face recognition method based on SVD perturbation for single example image per person." *Applied Mathematics and computation*, 163(2), 895-907.

Zhang, L., Dong, W., Zhang, D., and Shi, G. (2010). "Two-stage image denoising by principal component analysis with local pixel grouping." *Pattern Recognition*, 43(4), 1531-1549.

Zhao, W., Krishnaswamy, A., Chellappa, R., Swets, D. L., and Weng, J. (1998). "Discriminant analysis of principal components for face recognition." *Face Recognition*, Springer, 73-85.

Zhao, X., Gao, H., Zhang, G., Ayhan, B., Yan, F., Kwan, C., and Rose, J. L. (2007). "Active health monitoring of an aircraft wing with embedded piezoelectric sensor/actuator network: I. Defect detection, localization and growth monitoring." *Smart Materials and Structures*, 16(4), 1208.

Zheng, P., Greve, D. W., and Oppenheim, I. J. (2008). "Crack detection with wireless inductively-coupled transducers." *Proc., The 15th International Symposium on: Smart Structures and Materials & Nondestructive Evaluation and Health Monitoring*, San Diego, CA, 69321H.

Zhong, C. H., Croxford, A. J., and Wilcox, P. D. (2013). "Investigation of inductively coupled ultrasonic transducer system for NDE." *Ultrasonics, Ferroelectrics and Frequency Control, IEEE Transactions on*, 60(6).